



DEPARTMENT OF COMPUTER SCIENCE

## Diffusion Models for Time-Evolving Precipitation Fields

George Herbert

---

A dissertation submitted to the University of Bristol in accordance with the requirements of  
the degree of Master of Science in the Faculty of Engineering.

---

Tuesday 2<sup>nd</sup> May, 2023

---

# Abstract

---

# **Declaration**

I declare that the work in this dissertation was carried out in accordance with the requirements of the University's Regulations and Code of Practice for Taught Programmes and that it has not been submitted for any other academic award. Except where indicated by specific reference in the text, this work is my own work. Work done in collaboration with, or with the assistance of others, is indicated as such. I have identified all material in this dissertation which is not my own work through appropriate referencing and acknowledgement. Where I have quoted or otherwise incorporated material which is the work of others, I have included the source in the references. Any views expressed in the dissertation, other than referenced material, are those of the author.

George Herbert, Tuesday 2<sup>nd</sup> May, 2023

---

# Contents

<b>1</b>	<b>Introduction</b>	<b>1</b>
1.1	Problem Overview . . . . .	1
1.2	Aims and Objectives . . . . .	1
<b>2</b>	<b>Technical Background</b>	<b>3</b>
2.1	Generative Models . . . . .	3
2.2	Conditional Generation . . . . .	3
2.3	Latent Variables . . . . .	4
2.4	Likelihood-Based Generative Models . . . . .	4
2.5	Variational Autoencoders . . . . .	5
2.6	Score-Based Generative Models . . . . .	8
2.7	Diffusion Models . . . . .	8
<b>3</b>	<b>Related Work</b>	<b>19</b>
3.1	Statistical Downscaling . . . . .	19
3.2	Nowcasting . . . . .	20
<b>4</b>	<b>Experiments and Results</b>	<b>21</b>
4.1	Dataset . . . . .	21
4.2	Importance of the Transformation . . . . .	22
4.3	Learning a Transformation . . . . .	30
4.4	Temporal Interpolation . . . . .	37
4.5	Nowcasting . . . . .	41
<b>5</b>	<b>Conclusion</b>	<b>47</b>
5.1	Main Contributions . . . . .	47
5.2	Future Work . . . . .	47

---

# List of Figures

2.1	Graphical depiction of basic VAE with one observed variable $\mathbf{x}$ and one latent variable $\mathbf{z}$ . Solid lines depict the Bayesian network of the generative model; dashed lines depict the Bayesian network of the approximate inference model. . . . .	6
2.2	Graphical depiction of Markovian hierarchical VAE with one observed variable $\mathbf{x}$ and three latent variables $\mathbf{z}_1$ , $\mathbf{z}_2$ and $\mathbf{z}_3$ . Solid lines depict the Bayesian network of the generative model; dashed lines depict the Bayesian network of the approximate inference model. . . . .	7
2.3	Relationship between time $t$ and the log signal-to-noise ratio $\lambda_t$ for the truncated continuous-time $\alpha$ -cosine noise schedule $f_\Lambda(t)$ as defined in Equation 2.60 with $\lambda_{\min} = -30$ and $\lambda_{\max} = 30$ . The horizontal axis is time $t \in [0, 1]$ ; the vertical axis is $\lambda_t = f_\Lambda(t) \in [\lambda_{\min}, \lambda_{\max}] = [-30, 30]$ . . . . .	11
2.4	Relationship between time $t$ and $\alpha_t$ (left) and $\sigma_t$ (right) for the same truncated continuous-time $\alpha$ -cosine noise schedule as that in Figure 2.3. The horizontal axis is time $t \in [0, 1]$ ; the vertical axis is the value of $\alpha_t$ (left) and $\sigma_t$ (right). . . . .	11
2.5	Probability density function $p_\Lambda(\lambda)$ for the same truncated continuous-time $\alpha$ -cosine schedule as that in Figure 2.3. The horizontal axis is the log signal-to-noise ratio $\lambda \in [\lambda_{\min}, \lambda_{\max}]$ ; the vertical axis is the corresponding probability density $p_\Lambda$ . . . . .	12
2.6	Relationship between the log signal-to-noise ratio $\lambda$ and the functions $w(\lambda)$ and $-w'(\lambda)$ for the $\mathbf{v}$ -parameterisation with the same truncated continuous-time $\alpha$ -cosine schedule as that in Figure 2.3. The horizontal axis is the log signal-to-noise level $\lambda$ ; the vertical axis is the value of $w(\lambda)$ and $-w'(\lambda)$ ; the vertical axis is logarithmic. . . . .	15
4.1	Mean precipitation rate for each $8.8 \text{ km} \times 8.8 \text{ km}$ subarea in our dataset. . . . .	22
4.2	Two samples generated via our no-transformation model. The sample depicts hourly precipitation for the same $563.2 \text{ km} \times 563.2 \text{ km}$ region centred on Birmingham, UK, over ten hours. Each grid cell illustrates the mean precipitation rate, measured in millimetres per hour, for an $8.8 \text{ km} \times 8.8 \text{ km}$ subarea. The top sample exhibits significant noise at the lower end of the precipitation scale, while the bottom sample exhibits a baseline shift in precipitation rate. . . . .	23
4.3	Distribution of individual precipitation intensities in samples generated via our no-transformation model and the test set. The horizontal axis is the precipitation rate, measured in millimetres per hour; the vertical axis is frequency density. The vertical axis is scaled logarithmically. The left graph depicts the distribution of precipitation rates below 0.3 millimetres per hour, while the right graph depicts the full distribution. . . . .	24
4.4	QQ plot comparing the distribution of individual precipitation intensities in samples generated via our no-transformation model with the test set. Quantiles plotted are $\{1 - 10^{-n_1} + n_2 \cdot 10^{-n_1-1} \mid n_1, n_2 \in \mathbb{N}, 1 \leq n_1 \leq 6, 1 \leq n_2 \leq 9\}$ . The black line is the reference line, indicating where the quantiles of the generated samples would lie if they were equal to the quantiles of the test set. . . . .	25

---

4.5	Mean-normalised bias at each cell representing the same $8.8 \text{ km} \times 8.8 \text{ km}$ geographical area in the samples generated via our no-transformation model. . . . .	26
4.6	Power spectral density (PSD) graphs for samples generated via our no-transformation model and the test set. The horizontal axis is the number of waves, denoted $k$ ; the vertical axis is the mean power across all samples for a given $k$ , denoted $P(k)$ . Both axes are logarithmic. The left graph is for the two spatial dimensions, and the right graph is for the temporal dimension. . . . .	27
4.7	Distribution of individual precipitation intensities in samples generated via our square-root-transformation model, samples generated via our no-transformation model and the test set. The format of each graph is the same as Figure 4.3 . . . . .	28
4.8	QQ plot comparing the distribution of individual cells' values in samples generated by our square-root transformed model to samples generated by our untransformed model and the UKCP18 test set. The format is the same as Figure 4.4. . . . .	29
4.9	Mean-normalised bias at each cell representing the same $8.8 \text{ km} \times 8.8 \text{ km}$ geographical area in the samples generated by our square-root-transformation model. . . . .	29
4.10	PSD graphs for samples generated via our square-root transformed model, samples generated via our untransformed model, and the test set from UKCP18. The format is the same as Figure 4.6. . . . .	30
4.11	Randomly selected sample generated via our model trained with the loss function given in Equation 4.13. The format is the same as Figure 4.2a. . . . .	33
4.12	The transformation learnt by our model trained with the loss function given in Equation 4.15. The horizontal axis is the value of some element $x_i \in [-1, 1]$ input to the transformation network; the vertical axis is the corresponding output $h_\omega(x_i) \in [-1, 1]$ . . . . .	34
4.13	Distribution of precipitation rates in samples generated via our learnt-transformation model compared to samples generated via our square-root-transformation model and the test set from UKCP18. The format is the same as Figure 4.3. . . . .	35
4.14	QQ plots for individual cells within the test set from UKCP18 against both samples generated via our square-root-transformation model and samples generated via our learnt-transformation model. The format is the same as Figure 4.4. $\mathcal{Q} = \{1 - 10^{-n_1} + n_2 \cdot 10^{-n_1-1} \mid n_1, n_2 \in \mathbb{N}, 1 \leq n_2 \leq 9\}$ . . . . .	35
4.15	Mean-normalised bias at each cell representing the same $8.8 \text{ km} \times 8.8 \text{ km}$ geographical area in the samples generated via our learnt-transformation model. . . . .	36
4.16	Relationship between the mean-normalised bias at each cell representing the same $8.8 \text{ km} \times 8.8 \text{ km}$ geographical area in the samples generated via our square-root-transformation model and our learnt-transformation model. The horizontal axis is the mean-normalised bias for the square-root transformation; the vertical axis is the mean-normalised bias for the learnt transformation. The black line shows linear regression with a coefficient of determination of $R^2 = 0.59$ . . . . .	36
4.17	PSD graphs for samples generated via our learnt-transformation model, our square-root-transformation model and the test set from UKCP18. The format is the same as Figure 4.6. . . . .	37
4.18	Three samples generated via our learnt-transformation model. The format is the same as Figure 4.2a. . . . .	38
4.19	Distribution of individual precipitation rates in the conditionally generated interpolated samples produced by our learnt-transformation model with varying reconstruction-guidance weights, and the observed distribution of the corresponding withheld samples from 12 seasons in our test set. The format is the same as Figure 4.3. . . . .	40

---

---

4.20	QQ plot comparing the distribution of individual precipitation rates in the conditionally generated interpolated samples produced by our learnt-transformation model with varying reconstruction-guidance weights against the corresponding observed withheld samples from 12 seasons in our test set. The format is the same as Figure 4.4.	40
4.21	PSD graphs for samples generated via our learnt-transformation model with different reconstruction-guidance weights and the test set from UKCP18. The format is the same as Figure 4.6.	41
4.22	Temporally interpolated samples generated via our learnt-transformation model. Figure 4.22a depicts the observed sample in UKCP18, with the hourly snapshots conditioned on highlighted in red. The three subsequent figures depict interpolated samples generated with different reconstruction-guidance weights; captions below each figure indicate the reconstruction-guidance weight $w_r$ . Ideally, each hourly snapshot should be identical, or very similar, to the corresponding true snapshot in Figure 4.22a. The format of each hourly snapshot is the same as Figure 4.2a.	42
4.23	Distribution of individual precipitation rates in the conditionally generated nowcasts produced by our learnt-transformation model, and the observed distribution of the corresponding withheld samples from 12 seasons in our test set. The format is the same as Figure 4.3.	43
4.24	QQ plot comparing the distribution of individual precipitation rates in the conditionally generated nowcasts produced by our learnt-transformation model against the corresponding observed withheld samples from 12 seasons in our test set. The format is the same as Figure 4.4.	44
4.25	PSD graphs for conditionally generated nowcasts produced via our learnt-transformation model against the corresponding observed withheld samples from 12 seasons in our test set. The format is the same as Figure 4.6.	44
4.26	Nowcast sample generated via our learnt-transformation model. Figure 4.26a depicts an observed sample in UKCP18, with the hourly samples conditioned on in the subsequent nowcast highlighted in red. Figure 4.26b depicts the corresponding nowcast. Ideally, each hourly snapshot in the nowcast should resemble the corresponding observed snapshot. The format of each hourly snapshot is the same as Figure 4.2a.	45

---

# Ethics Statement

This project did not require ethical review, as determined by my supervisor Dr Laurence Aitchison.

---

# Notation and Acronyms

i.i.d.	: Independent and identically distributed
KL	: Kullback–Leibler
VAE	: Variational Autoencoder
ELBO	: Evidence Lower Bound
QQ	: Quantile-Quantile
PSD	: Power Spectral Density
:	:
$\mathbf{X}^{\circ n}$	: Element-wise exponentiation of matrix $\mathbf{X}$ with power $n$
$\text{diag}(\mathbf{x})$	: Diagonal matrix with the values of vector $\mathbf{x}$ on the diagonal
$\log(x)$	: Natural logarithm function (i.e. logarithm with base $e$ ) applied to $x$
$f \simeq g$	: $g$ is an unbiased estimator of $f$
$D_{\text{KL}}(P \  Q)$	: KL divergence of $P$ from $Q$

---

# Chapter 1

## Introduction

### 1.1 Problem Overview

Climatological data is of paramount importance in the modern world. Driven by the increasingly evident manifestations of climate change, the need for reliable simulations based on emissions scenarios has become increasingly pressing to guide those striving to mitigate the consequences and formulate policies to shape our planet’s future. The impact of climatological data extends beyond future projections: nowcasting currently supports real-world socioeconomic needs in various sectors reliant on weather-dependent decision-making [45].

Despite the importance of climatological data, challenges persist in both domains. High-resolution climate simulations—essential for representing critical features such as hourly rainfall characteristics and assessing the risk of life-threatening events like localised-flash flooding—are too computationally expensive. The computational burden poses a significant barrier to their widespread deployment [17]. Meanwhile, in the nowcasting domain, state-of-the-art operational techniques typically utilise radar-based wind estimates to advect precipitation fields, which struggle to capture non-linear events such as convective initiation and heavy precipitation [29].

Recent advancements in generative artificial intelligence provide a promising route to alleviate these challenges. Within the computer-vision domain, diffusion models [37, 12, 40] have outperformed previous state-of-the-art models—typically generative adversarial networks (GANs) [8]—in various tasks, including text-to-image synthesis [28, 31, 33], image inpainting [40, 23] and image superresolution [34, 14]. In the climate simulations domain, diffusion models have successfully downscaled high-resolution precipitation samples with realistic spatial structures based on low-resolution inputs [1], thereby presenting a promising method to reduce computational costs. However, diffusion models capable of downscaling currently operate on daily mean snapshots, potentially neglecting critical information in time-evolving data at a higher temporal resolution, such as the strong autocorrelation inherent in precipitation and capturing hourly peaks [24].

Researchers have recently adapted diffusion models to the video domain [15, 11], making significant strides towards generating temporally-coherent high-fidelity video. In this work, we build upon these advancements by adopting techniques from video diffusion models to generate time-evolving precipitation fields.

### 1.2 Aims and Objectives

We summarise the aims and objectives of this work as follows:

- To leverage techniques employed in video diffusion models to develop a diffusion model capable of unconditionally generating time-evolving precipitation fields; and to provide a comprehensive assessment of the model’s capabilities and limitations.

## *1.2. AIMS AND OBJECTIVES*

---

- To devise methods to address any identified limitations and evaluate the efficacy of these approaches.
- To extend the diffusion model for conditional generation in order to enhance the temporal resolution of existing time-evolving precipitation simulations, thus demonstrating initial proof-of-principle of the capacity for diffusion models to decrease the computational cost of time-evolving high-resolution climate simulations.
- To provide preliminary results for nowcasting, aiming to encourage future research in this area. As the current state-of-the-art generative model for nowcasting is a GAN [29], we hypothesise that a well-optimised diffusion model will present a more optimal solution, reflecting accomplishments observed in the computer-vision domain.

---

# Chapter 2

## Technical Background

### 2.1 Generative Models

Let us consider some dataset  $\mathcal{D}$  consisting of  $N_{\mathcal{D}} \geq 1$  datapoints which we assume are independent and identically distributed (i.i.d.):

$$\mathcal{D} = \{\mathbf{x}^{(i)} \mid 1 \leq i \leq N_{\mathcal{D}}, i \in \mathbb{N}\} \quad (2.1)$$

We assume each observed datapoint  $\mathbf{x}^{(i)} \in \mathcal{D}$  is a realisation of the observed random variable  $\mathbf{x}$  from an underlying process, whose true distribution  $p^*(\mathbf{x})$  is unknown. We will omit the index  $(i)$  whenever it is clear we are referring to a single datapoint. The goal of *generative modelling* is to approximate this true distribution with a chosen model  $p_{\theta}(\mathbf{x})$  with parameters  $\theta$ . We learn parameters  $\theta$  such that the probability distribution function given by the model  $p_{\theta}(\mathbf{x})$  approximates the true distribution of the data, such that for any observed  $\mathbf{x}$ :

$$p_{\theta}(\mathbf{x}) \approx p^*(\mathbf{x}) \quad (2.2)$$

Once learnt, we can generate new samples *unconditionally* from our approximate model at will. We thus refer to the model  $p_{\theta}(\mathbf{x})$  as an unconditional generative model.

### 2.2 Conditional Generation

We can extend generative modelling to the conditional setting. We consider each observed  $\mathbf{x}$  to have some corresponding conditioning information  $\mathbf{c}$ . In this context, we wish to approximate the conditional distribution  $p^*(\mathbf{x}|\mathbf{c})$ . Similar to the unconditional setting, we learn parameters  $\theta$  for our model  $p_{\theta}(\mathbf{x}|\mathbf{c})$  such that for any observed  $\mathbf{x}$  and conditioning information  $\mathbf{c}$ :

$$p_{\theta}(\mathbf{x}|\mathbf{c}) \approx p^*(\mathbf{x}|\mathbf{c}) \quad (2.3)$$

Once learnt, we can generate new samples *conditionally* from our approximate model at will.

One of the most basic cases is a class-conditional generative model, where the conditioning variable  $\mathbf{c}$  is simply a class label. In such cases, our conditional model  $p_{\theta}(\mathbf{x}|\mathbf{c})$  has an interpretation as the reverse of a discriminative classification model—a more traditional form of machine learning. As opposed to inputting an observed  $\mathbf{x}$  and the model outputting the predicted corresponding class label  $\mathbf{c}$ , we input a class label  $\mathbf{c}$  and use the model to generate a new sample  $\mathbf{x} \sim p_{\theta}(\mathbf{x}|\mathbf{c})$ .

Significantly, the conditioning variable  $\mathbf{c}$  is not limited to class labels; it can be flexible and take the form of any additional information we wish to condition on to generate samples. A powerful tool in the case of image generation,  $\mathbf{c}$  may be a text encoding to facilitate text-to-image synthesis (see e.g. [33, 16]). Alternatively,  $\mathbf{c}$  may be a lower-resolution image from which

we wish to upscale to add higher-resolution details, known as image super-resolution (see e.g. [14]).

In this work, we do not explicitly use a conditional model. However, we do derive one approximately from an unconditional model. We discuss this further in Section 2.7.8.

## 2.3 Latent Variables

We can think of each observed datapoint  $\mathbf{x} \in \mathcal{D}$  as being represented or generated via  $N_{\mathbf{z}} \geq 1$  associated *latent variables*:

$$\{\mathbf{z}_1, \dots, \mathbf{z}_{N_{\mathbf{z}}}\} = \{\mathbf{z}_i \mid i \leq 1 \leq N_{\mathbf{z}}, i \in \mathbb{N}\} \quad (2.4)$$

The latent variables are part of the model, but we do not observe them directly, and they are not within the dataset. We model the joint distribution of the observed variable and the latent variables by  $p_{\theta}(\mathbf{x}, \mathbf{z}_1, \dots, \mathbf{z}_{N_{\mathbf{z}}})$ ; the marginal distribution over the observed variable  $p_{\theta}(\mathbf{x})$  is given by:

$$p_{\theta}(\mathbf{x}) = \int p_{\theta}(\mathbf{x}, \mathbf{z}_1, \dots, \mathbf{z}_{N_{\mathbf{z}}}) d\mathbf{z} \quad (2.5)$$

In the context of a latent-variable model, *generation* refers to the process of sampling the latent variables from the joint distribution  $p_{\theta}(\mathbf{z}_1, \dots, \mathbf{z}_{N_{\mathbf{z}}})$ , and then sampling the observed variable from the conditional distribution  $p_{\theta}(\mathbf{x}|\mathbf{z}_1, \dots, \mathbf{z}_{N_{\mathbf{z}}})$ . In the simplest case, we may only have a single latent variable; we omit the index 1 in such cases for notational simplicity.

## 2.4 Likelihood-Based Generative Models

As mentioned in Section 2.1, the goal of a generative model is to learn parameters  $\theta$  such that  $p_{\theta}(\mathbf{x}) \approx p^*(\mathbf{x})$ . One way to interpret this is as a minimisation problem. Namely, we wish to learn parameters  $\theta$  that minimise the Kullback–Leibler (KL) divergence of the true distribution  $p^*(\mathbf{x})$  from our model distribution  $p_{\theta}(\mathbf{x})$ :

$$\arg \min_{\theta} D_{\text{KL}}(p^*(\mathbf{x}) \| p_{\theta}(\mathbf{x})) \quad (2.6)$$

The KL divergence  $D_{\text{KL}}$  measures the dissimilarity between two probability distributions; in our case, it provides a measure of the information lost when we approximate the true distribution  $p^*(\mathbf{x})$  with our model distribution  $p_{\theta}(\mathbf{x})$ .

We can reformulate the KL divergence of the true distribution  $p^*(\mathbf{x})$  from our model distribution  $p_{\theta}(\mathbf{x})$  to provide a likelihood-based interpretation:

$$D_{\text{KL}}(p^*(\mathbf{x}) \| p_{\theta}(\mathbf{x})) = \mathbb{E}_{\mathbf{x} \sim p^*(\mathbf{x})} \left[ \log \left( \frac{p^*(\mathbf{x})}{p_{\theta}(\mathbf{x})} \right) \right] \quad (2.7)$$

$$= \mathbb{E}_{\mathbf{x} \sim p^*(\mathbf{x})} [\log p^*(\mathbf{x})] + \mathbb{E}_{\mathbf{x} \sim p^*(\mathbf{x})} [-\log p_{\theta}(\mathbf{x})] \quad (2.8)$$

$$= -\mathcal{H}(p^*(\mathbf{x})) + \mathbb{E}_{\mathbf{x} \sim p^*(\mathbf{x})} [-\log p_{\theta}(\mathbf{x})] \quad (2.9)$$

where  $\mathcal{H}(p^*(\mathbf{x}))$  is the entropy of the true distribution  $p^*(\mathbf{x})$  and is constant. As such, minimisation of the KL divergence in this context equates to minimisation of the expected negative log-likelihood of our model distribution  $p_{\theta}(\mathbf{x})$  with respect to  $\mathbf{x} \sim p^*(\mathbf{x})$ ; formally:

$$\arg \min_{\theta} D_{\text{KL}}(p^*(\mathbf{x}) \| p_{\theta}(\mathbf{x})) = \arg \min_{\theta} \mathbb{E}_{\mathbf{x} \sim p^*(\mathbf{x})} [-\log p_{\theta}(\mathbf{x})] \quad (2.10)$$

Under the assumption that each of the  $N_{\mathcal{D}}$  samples in our dataset  $\mathcal{D}$  are i.i.d. according to  $p^*(\mathbf{x})$ , we can construct an unbiased estimator:

$$\mathbb{E}_{\mathbf{x} \sim p^*(\mathbf{x})} [-\log p_{\theta}(\mathbf{x})] \simeq \frac{1}{N_{\mathcal{D}}} (-\log p_{\theta}(\mathcal{D})) = \frac{1}{N_{\mathcal{D}}} \sum_{\mathbf{x} \in \mathcal{D}} (-\log p_{\theta}(\mathbf{x})) \quad (2.11)$$

In other words, under the i.i.d assumption of  $\mathcal{D}$ , the mean negative log-likelihood of our model with respect to  $\mathcal{D}$  serves as an unbiased estimator of the expected negative log-likelihood of our model with respect to  $\mathbf{x} \sim p^*(\mathbf{x})$ . In practice, for computational efficiency reasons—as well as GPU memory limitations—we learn via mini-batches  $\mathcal{M} \subset \mathcal{D}$  of size  $N_{\mathcal{M}} < N_{\mathcal{D}}$ , which is itself an unbiased estimator:

$$\frac{1}{N_{\mathcal{D}}} (-\log p_{\theta}(\mathcal{D})) \simeq \frac{1}{N_{\mathcal{M}}} (-\log p_{\theta}(\mathcal{M})) = \frac{1}{N_{\mathcal{M}}} \sum_{\mathbf{x} \in \mathcal{M}} (-\log p_{\theta}(\mathbf{x})) \quad (2.12)$$

As such, by transitivity, the mean negative log-likelihood of our model with respect to each mini-batch  $\mathcal{M}$  is itself an unbiased estimator of the expected negative log-likelihood of our model with respect to  $\mathbf{x} \sim p^*(\mathbf{x})$ . We refer to the broad class of generative models trained to minimise the expected negative log-likelihood of  $p_{\theta}(\mathbf{x})$  with respect to  $\mathbf{x} \sim p^*(\mathbf{x})$  as *likelihood-based generative models*.

## 2.5 Variational Autoencoders

### 2.5.1 Components of the Basic Variational Autoencoder

The variational autoencoder (VAE) [20, 30] is an important example of a likelihood-based generative model. In its simplest form, the VAE is a latent-variable model  $p_{\theta}(\mathbf{x}, \mathbf{z})$  with a single latent  $\mathbf{z}$ . We assume that each observed datapoint  $\mathbf{x}$  is generated via a two-step process. First, a latent  $\mathbf{z}$  is generated from some true prior distribution  $p^*(\mathbf{z})$ , followed by an observed value  $\mathbf{x}$  generated from some true conditional distribution  $p^*(\mathbf{x}|\mathbf{z})$ . Thus, our model  $p_{\theta}(\mathbf{x}, \mathbf{z})$  we seek to optimise such that  $p_{\theta}(\mathbf{x}) \approx p^*(\mathbf{x})$  takes the following factorised form:

$$p_{\theta}(\mathbf{x}, \mathbf{z}) = p_{\theta}(\mathbf{z})p_{\theta}(\mathbf{x}|\mathbf{z}) \quad (2.13)$$

where, naturally, we need to specify our two distributions:  $p_{\theta}(\mathbf{z})$  and  $p_{\theta}(\mathbf{x}|\mathbf{z})$ . We refer to  $p_{\theta}(\mathbf{z})$  as the prior over  $\mathbf{z}$ , and one common choice is the standard Gaussian:

$$p_{\theta}(\mathbf{z}) = \mathcal{N}(\mathbf{z}; \mathbf{0}, \mathbf{I}) \quad (2.14)$$

Furthermore, we refer to  $p_{\theta}(\mathbf{x}|\mathbf{z})$  as the stochastic *decoder* since given a latent  $\mathbf{z}$  it produces a distribution over the possible corresponding values of  $\mathbf{x}$ . As an example, we can select  $p_{\theta}(\mathbf{x}|\mathbf{z})$  be a multivariate Gaussian with diagonal covariance:

$$p_{\theta}(\mathbf{x}|\mathbf{z}) = \mathcal{N}(\mathbf{x}; \boldsymbol{\mu}_{\theta}(\mathbf{z}), \text{diag}(\boldsymbol{\sigma}_{\theta}(\mathbf{z}))^{\circ 2}) \quad (2.15)$$

where  $\boldsymbol{\mu}_{\theta}(\mathbf{z})$  and  $\boldsymbol{\sigma}_{\theta}(\mathbf{z})$  are outputs from a neural network with parameters  $\theta$ . One final, crucial defining feature of the VAE is the stochastic *encoder*  $q_{\phi}(\mathbf{z}|\mathbf{x})$ , also referred to as the *inference model*, with variational parameters  $\phi$ . The stochastic encoder  $q_{\phi}(\mathbf{z}|\mathbf{x})$  approximates the intractable posterior  $p_{\theta}(\mathbf{z}|\mathbf{x})$  of the generative model. Again, a common choice is for  $q_{\phi}(\mathbf{z}|\mathbf{x})$  to be a multivariate Gaussian with diagonal covariance:

$$q_{\phi}(\mathbf{z}|\mathbf{x}) = \mathcal{N}(\mathbf{z}, \boldsymbol{\mu}_{\phi}(\mathbf{z}), \text{diag}(\boldsymbol{\sigma}_{\phi}(\mathbf{z}))^{\circ 2}) \quad (2.16)$$

Figure 2.1 provides a graphical depiction of the VAE.

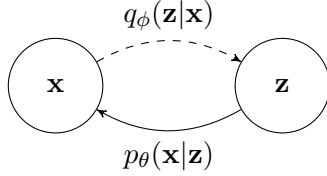


Figure 2.1: Graphical depiction of basic VAE with one observed variable  $\mathbf{x}$  and one latent variable  $\mathbf{z}$ . Solid lines depict the Bayesian network of the generative model; dashed lines depict the Bayesian network of the approximate inference model.

### 2.5.2 Evidence Lower Bound Objective

The VAE falls into the broad class of likelihood-based generative models. However, the likelihood  $p_\theta(\mathbf{x})$  cannot be optimised directly, as the VAE model does not make common simplifying assumptions about marginal and posterior probabilities. Notably, we assume the model's marginal likelihood  $p(\mathbf{x})$  given by:

$$p_\theta(\mathbf{x}) = \int p_\theta(\mathbf{x}|\mathbf{z})p_\theta(\mathbf{z})d\mathbf{z} \quad (2.17)$$

does not have an analytic solution or efficient estimator. In addition, we assume the model's posterior density  $p_\theta(\mathbf{z}|\mathbf{x})$  is intractable, so we cannot employ the expectation-maximisation algorithm.

Not making these simplifying assumptions is the reason for introducing the inference model  $q_\phi(\mathbf{z}|\mathbf{x})$  to approximate the model's intractable posterior  $p_\theta(\mathbf{z}|\mathbf{x})$ . With the introduction of the inference model, we can derive a variational bound on the negative log-likelihood:

$$-\log p_\theta(\mathbf{x}) = \mathbb{E}_{\mathbf{z} \sim q_\phi(\mathbf{z}|\mathbf{x})} [-\log p_\theta(\mathbf{x})] \quad (2.18)$$

$$= \mathbb{E}_{\mathbf{z} \sim q_\phi(\mathbf{z}|\mathbf{x})} \left[ -\log \left( \frac{p_\theta(\mathbf{x}, \mathbf{z})}{p_\theta(\mathbf{z}|\mathbf{x})} \right) \right] \quad (2.19)$$

$$= \mathbb{E}_{\mathbf{z} \sim q_\phi(\mathbf{z}|\mathbf{x})} \left[ -\log \left( \frac{p_\theta(\mathbf{x}, \mathbf{z})q_\phi(\mathbf{z}|\mathbf{x})}{p_\theta(\mathbf{z}|\mathbf{x})q_\phi(\mathbf{z}|\mathbf{x})} \right) \right] \quad (2.20)$$

$$= \mathbb{E}_{\mathbf{z} \sim q_\phi(\mathbf{z}|\mathbf{x})} \left[ -\log \left( \frac{p_\theta(\mathbf{x}, \mathbf{z})}{q(\mathbf{z}|\mathbf{x})} \right) \right] - \mathbb{E}_{\mathbf{z} \sim q_\phi(\mathbf{z}|\mathbf{x})} \left[ \log \left( \frac{q(\mathbf{z}|\mathbf{x})}{p_\theta(\mathbf{z}|\mathbf{x})} \right) \right] \quad (2.21)$$

$$= \mathbb{E}_{\mathbf{z} \sim q_\phi(\mathbf{z}|\mathbf{x})} \left[ -\log \left( \frac{p_\theta(\mathbf{x}, \mathbf{z})}{q(\mathbf{z}|\mathbf{x})} \right) \right] - D_{\text{KL}}(q_\phi(\mathbf{z}|\mathbf{x}) \| p_\theta(\mathbf{z}|\mathbf{x})) \quad (2.22)$$

The second term in Equation 2.22 is the KL divergence of  $q_\phi(\mathbf{z}|\mathbf{x})$  and  $p_\theta(\mathbf{z}|\mathbf{x})$  and is non-negative:

$$D_{\text{KL}}(q_\phi(\mathbf{z}|\mathbf{x}) \| p_\theta(\mathbf{z}|\mathbf{x})) \geq 0 \quad (2.23)$$

and zero if and only if  $q_\phi(\mathbf{z}|\mathbf{x}) = p_\theta(\mathbf{z}|\mathbf{x})$ . The first term in Equation 2.22 is the additive inverse of the *evidence lower bound objective* (ELBO); in this work, we will refer to this as the ELBO loss, denoted  $\mathcal{L}_{\text{ELBO}}$ . By the non-negativity of the KL divergence, it serves as a variational bound on the negative log-likelihood of the observed variable  $\mathbf{x}$ :

$$-\log p_\theta(\mathbf{x}) \leq \mathcal{L}_{\text{ELBO}}(\mathbf{x}) \quad (2.24)$$

$$= \mathbb{E}_{\mathbf{z} \sim q_\phi(\mathbf{z}|\mathbf{x})} \left[ -\log \left( \frac{p_\theta(\mathbf{x}, \mathbf{z})}{q(\mathbf{z}|\mathbf{x})} \right) \right] \quad (2.25)$$

As such, minimisation of the ELBO loss accomplishes two things. Firstly, it will approximately minimise the negative log-likelihood of the observed variable  $\mathbf{x}$ —the overriding goal of a likelihood-based generative model. Secondly, it will minimise the KL divergence of  $q_\phi(\mathbf{z}|\mathbf{x})$  from  $p_\theta(\mathbf{z}|\mathbf{x})$ , thus encouraging the approximate posterior  $q_\phi(\mathbf{z}|\mathbf{x})$  to approximate the true posterior  $p_\theta(\mathbf{z}|\mathbf{x})$  as closely as possible.

### 2.5.3 Markovian Hierarchical Variational Autoencoders

The Markovian hierarchical variational autoencoder (MHVAE) [21, 38] is a versatile extension of the VAE, accommodating an unrestricted number  $N_{\mathbf{z}} \geq 1$  of latent variables. Notably, the joint distribution of the observed variable and the latent variables is Markovian:

$$p_{\theta}(\mathbf{x}, \mathbf{z}_1, \dots, \mathbf{z}_{N_{\mathbf{z}}}) = p(\mathbf{x}|\mathbf{z}_1)p_{\theta}(\mathbf{z}_{N_{\mathbf{z}}}) \prod_{i=1}^{N_{\mathbf{z}}-1} p_{\theta}(\mathbf{z}_i|\mathbf{z}_{i+1}) \quad (2.26)$$

Figure 2.2 illustrates the MHVAE model. For the generative model, the observed variable  $\mathbf{x}$  is conditionally independent of  $\mathbf{z}_2$  and  $\mathbf{z}_3$  given  $\mathbf{z}_1$ . Similarly,  $\mathbf{z}_1$  is conditionally independent of  $\mathbf{z}_3$  given  $\mathbf{z}_2$ .

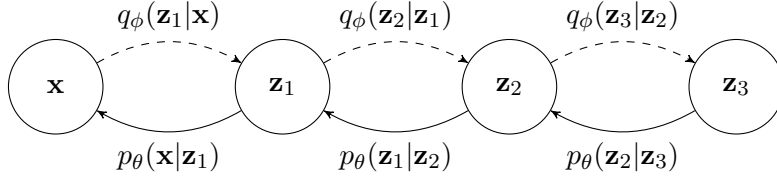


Figure 2.2: Graphical depiction of Markovian hierarchical VAE with one observed variable  $\mathbf{x}$  and three latent variables  $\mathbf{z}_1$ ,  $\mathbf{z}_2$  and  $\mathbf{z}_3$ . Solid lines depict the Bayesian network of the generative model; dashed lines depict the Bayesian network of the approximate inference model.

### 2.5.4 Infinitely Deep Markovian Hierarchical Variational Autoencoders

In the limit of  $N_{\mathbf{z}} \rightarrow \infty$ , we instead notationally write our latent variables in terms of a continuous-time variable  $t \in [0, 1]$  as:

$$\{\mathbf{z}_0, \dots, \mathbf{z}_1\} = \{\mathbf{z}_t \mid t \in [0, 1]\} \quad (2.27)$$

We can formulate the ELBO loss for the continuous-time MHVAE as follows:

$$-\log p_{\theta}(\mathbf{x}) \leq \mathcal{L}_{\text{ELBO}}(\mathbf{x}) \quad (2.28)$$

$$= \mathbb{E}_{\mathbf{z}_0, \dots, \mathbf{z}_1 \sim q_{\phi}(\mathbf{z}_0, \dots, \mathbf{z}_1 | \mathbf{x})} \left[ -\log \left( \frac{p_{\theta}(\mathbf{x}, \mathbf{z}_0, \dots, \mathbf{z}_1)}{q_{\phi}(\mathbf{z}_0, \dots, \mathbf{z}_1 | \mathbf{x})} \right) \right] \quad (2.29)$$

$$= \mathbb{E}_{\mathbf{z}_0 \sim q(\mathbf{z}_0, \mathbf{x})} [-\log p_{\theta}(\mathbf{x}|\mathbf{z}_0)] + D_{\text{KL}}(q(\mathbf{z}_0, \dots, \mathbf{z}_1 | \mathbf{x}) \| p_{\theta}(\mathbf{z}_0, \dots, \mathbf{z}_1)) \quad (2.30)$$

Per datapoint  $\mathbf{x}$ , we define  $\mathcal{L}_T(t)$  as the KL divergence of  $q_{\phi}(\mathbf{z}_t, \dots, \mathbf{z}_1 | \mathbf{x})$  from  $p_{\theta}(\mathbf{z}_t, \dots, \mathbf{z}_1)$  for a subset of timesteps from  $t$  to 1, and its corresponding time derivative  $\mathcal{L}'_T(t)$  as:

$$\mathcal{L}_T(t) = D_{\text{KL}}(q_{\phi}(\mathbf{z}_t, \dots, \mathbf{z}_1 | \mathbf{x}) \| p_{\theta}(\mathbf{z}_t, \dots, \mathbf{z}_1)) \quad (2.31)$$

$$\mathcal{L}'_T(t) = \frac{d}{dt} \mathcal{L}_T(t) \quad (2.32)$$

We can substitute this into the ELBO loss and use the second fundamental theorem of calculus to yield the following form for the ELBO loss, defined per datapoint  $\mathbf{x}$  as:

$$\mathcal{L}_{\text{ELBO}}(\mathbf{x}) = \mathbb{E}_{\mathbf{z}_0 \sim q(\mathbf{z}_0, \mathbf{x})} [-\log p_{\theta}(\mathbf{x}|\mathbf{z}_0)] + D_{\text{KL}}(q(\mathbf{z}_0, \dots, \mathbf{z}_1 | \mathbf{x}) \| p_{\theta}(\mathbf{z}_0, \dots, \mathbf{z}_1)) \quad (2.33)$$

$$= \mathbb{E}_{\mathbf{z}_0 \sim q(\mathbf{z}_0, \mathbf{x})} [-\log p_{\theta}(\mathbf{x}|\mathbf{z}_0)] + \mathcal{L}_T(0) \quad (2.34)$$

$$= \mathbb{E}_{\mathbf{z}_0 \sim q(\mathbf{z}_0, \mathbf{x})} [-\log p_{\theta}(\mathbf{x}|\mathbf{z}_0)] + \mathcal{L}_T(1) - \int_0^1 \mathcal{L}'_T(t) dt \quad (2.35)$$

This form for the ELBO may seem unconventional. However, we introduce it here to motivate a strong theoretical link between the ELBO and the weighted loss [19], which is used to train diffusion models in the broader literature. We explore the weighted loss in Section 2.7.6.

## 2.6 Score-Based Generative Models

Score-based generative models [39, 40] are an alternative to likelihood-based generative models. We define the *score* of a probability density  $p(\mathbf{x})$  to be:

$$\nabla_{\mathbf{x}} \log p(\mathbf{x}) \quad (2.36)$$

The *score network*  $\mathbf{s}_\theta$  is a neural network parameterised by  $\theta$  trained to approximate the score of the true data distribution  $p^*(\mathbf{x})$ , such that for any observed  $\mathbf{x}$ :

$$\mathbf{s}_\theta(\mathbf{x}) \approx \nabla_{\mathbf{x}} \log p^*(\mathbf{x}) \quad (2.37)$$

Importantly, we accomplish this without training a model to directly approximate the true data distribution  $p^*(\mathbf{x})$  in advance.

## 2.7 Diffusion Models

Diffusion models [37, 12, 40] are a framework for generative modelling. Diffusion models consist of a *forward diffusion process* that transforms a datapoint into noise, and a *reverse-time generative model* able to transform noise back into a datapoint. As we explore in this section, diffusion models have both likelihood and score-based interpretations.

### 2.7.1 Forward Diffusion Process

Specified in continuous time, the *forward diffusion process* is a Gaussian diffusion process that defines the model's latent variables as a sequence of increasingly noisy versions of  $\mathbf{x}$ :

$$\{\mathbf{z}_0, \dots, \mathbf{z}_1\} = \{\mathbf{z}_t \mid t \in [0, 1]\} \quad (2.38)$$

An Itô stochastic differential equation (SDE) defines the time evolution of the diffusion process [40]:

$$d\mathbf{z}_t = \mathbf{f}(\mathbf{z}_t, t)dt + g(t)d\mathbf{w}_t \quad (2.39)$$

where  $\mathbf{w}_t$  is the standard Wiener process (i.e. Brownian motion);  $\mathbf{f}(\mathbf{z}_t, t) : \mathbb{R}^D \rightarrow \mathbb{R}^D$  is a vector-valued function called the *drift* coefficient of  $\mathbf{z}$ ;  $g(t) : \mathbb{R} \rightarrow \mathbb{R}$  is a scalar-function known as the *diffusion* coefficient of  $\mathbf{z}_t$ ; and  $D$  is the dimensionality of our input data. In this work, we use a *variance-preserving* diffusion model, which we define by the following drift and diffusion coefficients:

$$\mathbf{f}(\mathbf{z}_t, t) = -\frac{1}{2} \left( \frac{d}{dt} \log (1 + \exp(-\lambda_t)) \right) \mathbf{z}_t \quad (2.40)$$

$$g(t)^2 = \frac{d}{dt} \log (1 + \exp(-\lambda_t)) \quad (2.41)$$

where  $\lambda_t \in [\lambda_{\min}, \lambda_{\max}]$  is a monotonically decreasing scalar-valued function of time  $t \in [0, 1]$ ; we provide more details on  $\lambda_t$  in Section 2.7.3. The forward process forms a conditional joint distribution  $q(\mathbf{z}_0, \dots, \mathbf{z}_1 | \mathbf{x})$ , whose marginal distribution of each latent variable  $\mathbf{z}_t$  given the observed variable  $\mathbf{x}$  is given by:

$$q(\mathbf{z}_t | \mathbf{x}) = \mathcal{N}(\mathbf{z}_t; \alpha_t \mathbf{x}, \sigma_t^2 \mathbf{I}) \quad (2.42)$$

where  $\alpha_t$  and  $\sigma_t$  are functions of  $\lambda_t$ , such that:

$$\alpha_t^2 = S(\lambda_t) \quad (2.43)$$

$$\sigma_t^2 = S(-\lambda_t) \quad (2.44)$$

where  $S$  is the sigmoid function. The joint distribution of latent variables  $\mathbf{z}_r, \mathbf{z}_s, \mathbf{z}_t$  at subsequent timesteps  $0 \leq r < s < t \leq 1$  is Markovian, and thus:

$$q(\mathbf{z}_t | \mathbf{z}_s, \mathbf{z}_r) = q(\mathbf{z}_t | \mathbf{z}_s) = \mathcal{N} \left( \mathbf{z}_t; \alpha_{t|s} \mathbf{z}_s, \sigma_{t|s}^2 \mathbf{I} \right) \quad (2.45)$$

where  $\alpha_{t|s}$  and  $\sigma_{t|s}$  are given by:

$$\alpha_{t|s} = \frac{\alpha_t}{\alpha_s} \quad (2.46)$$

$$\sigma_{t|s}^2 = \sigma_t^2 - \alpha_{t|s}^2 \sigma_s^2 \quad (2.47)$$

The true distribution  $p^*(\mathbf{x})$  plus the conditional joint distribution of the forward model  $q(\mathbf{z}_0, \dots, \mathbf{z}_1 | \mathbf{x})$  defines the following joint distribution:

$$q(\mathbf{z}_0, \dots, \mathbf{z}_1) = \int p^*(\mathbf{x}) q(\mathbf{z}_0, \dots, \mathbf{z}_1 | \mathbf{x}) d\mathbf{x} \quad (2.48)$$

### 2.7.2 Reverse-Time Generative Model

Anderson [2] shows that the forward SDE of Equation 2.39 is exactly solved by a second diffusion process, running backwards in time and given by the reverse-time SDE:

$$d\mathbf{z}_t = [\mathbf{f}(\mathbf{z}_t, t) - g(t)^2 \nabla_{\mathbf{z}_t} \log q(\mathbf{z}_t)] dt + g(t) d\bar{\mathbf{w}}_t \quad (2.49)$$

where  $\bar{\mathbf{w}}_t$  is a standard Wiener process when time flows backwards. Let  $\mathbf{s}_\theta(\mathbf{z}_t, \lambda_t)$  be a  $\lambda_t$ -dependent score network [39] that approximates the score of  $q(\mathbf{z}_t)$  such that:

$$\mathbf{s}_\theta(\mathbf{z}_t, \lambda_t) \approx \nabla_{\mathbf{z}_t} \log q(\mathbf{z}_t) \quad (2.50)$$

Thus, if we have a perfect score model  $\mathbf{s}_\theta(\mathbf{z}_t, \lambda_t) = \nabla_{\mathbf{z}_t} q(\mathbf{z}_t)$ , then the reverse-time SDE is exactly:

$$d\mathbf{z}_t = [\mathbf{f}(\mathbf{z}_t, t) - g(t)^2 \mathbf{s}_\theta(\mathbf{z}_t, \lambda_t)] dt + g(t) d\bar{\mathbf{w}}_t \quad (2.51)$$

In the broader literature, diffusion models utilise a variety of numerical solvers to provide approximate trajectories of the reverse-time SDE. In this work, we sequentially generate latent variables starting from  $t = 1$  and working backwards to  $t = 0$ , over  $T$  uniformly-spaced discrete timesteps. More formally, this comprises a hierarchical generative model that defines a joint distribution over latent variables as follows:

$$p_\theta(\mathbf{z}_0, \dots, \mathbf{z}_1) = p_\theta(\mathbf{z}_1) \prod_{i=1}^T p_\theta(\mathbf{z}_{s(i)} | \mathbf{z}_{t(i)}) \quad (2.52)$$

where  $s(i) = (i - 1) \cdot T^{-1}$  and  $t(i) = i \cdot T^{-1}$ . For large enough  $\lambda_{\max}$ ,  $\mathbf{z}_0$  is almost noiseless, so learning a model  $p_\theta(\mathbf{z}_0)$  is practically equivalent to learning a model  $p_\theta(\mathbf{x})$ . For sufficiently small  $\lambda_{\min}$ ,  $\mathbf{z}_1$  contains almost no information about  $\mathbf{x}$ . As such, there exists a distribution  $p_\theta(\mathbf{z}_1)$  such that:

$$D_{\text{KL}}(q(\mathbf{z}_1 | \mathbf{x}) \| p_\theta(\mathbf{z}_1)) \approx 0 \quad (2.53)$$

For variance-preserving diffusion models, as used in this work, we model  $p_\theta(\mathbf{z}_1)$  as the multivariate standard Gaussian:

$$p_\theta(\mathbf{z}_1) = \mathcal{N}(\mathbf{z}_1; \mathbf{0}, \mathbf{I}) \quad (2.54)$$

Once we have sampled  $\mathbf{z}_1 \sim p_\theta(\mathbf{z}_1)$ , we use the discrete-time ancestral sampler [12] to sequentially generate each latent variable  $\mathbf{z}_s$  from  $\mathbf{z}_t$  where  $0 \leq s < t \leq 1$ . This corresponds to a particular discretisation of the reverse-time variance-preserving SDE, as shown by Song et al. [40]. More formally, from a given latent  $\mathbf{z}_t$  we generate  $\mathbf{z}_s \sim p_\theta(\mathbf{z}_s|\mathbf{z}_t)$  via:

$$p_\theta(\mathbf{z}_s|\mathbf{z}_t) = q(\mathbf{z}_s|\mathbf{z}_t, \mathbf{x} = \hat{\mathbf{x}}_\theta(\mathbf{z}_t, \lambda_t)) \quad (2.55)$$

$$= \mathcal{N}\left(\tilde{\mu}_{s|t}(\mathbf{z}_t, \mathbf{x} = \hat{\mathbf{x}}_\theta(\mathbf{z}_t, \lambda_t)), \tilde{\sigma}_{s|t}\mathbf{I}\right) \quad (2.56)$$

where  $\hat{\mathbf{x}}_\theta(\mathbf{z}_t, \lambda_t)$  is our denoised estimate of the original data  $\mathbf{x}$  given latent  $\mathbf{z}_t$  and log signal-to-noise ratio  $\lambda_t$ , and

$$\tilde{\mu}_{s|t}(\mathbf{z}_t, \mathbf{x}) = \frac{\alpha_{t|s}\sigma_s^2}{\sigma_t^2}\mathbf{z}_t + \frac{\alpha_s\sigma_{t|s}^2}{\sigma_t^2}\mathbf{x} \quad (2.57)$$

$$\tilde{\sigma}_{s|t} = \frac{\sigma_{t|s}\sigma_s}{\sigma_t} \quad (2.58)$$

Interestingly, in Equation 2.55 we introduced a denoiser network  $\hat{\mathbf{x}}_\theta(\mathbf{z}_t, \lambda_t)$  to define the discrete-time ancestral sampler, while in Equation 2.50 we described diffusion models as learning a score network  $\mathbf{s}_\theta(\mathbf{z}_t, \lambda_t)$ . One of the powerful aspects of diffusion models is that we can freely switch between different parameterisations. For example, we can train a neural network  $\mathbf{s}_\theta(\mathbf{z}_t, \lambda_t)$  to predict the score of  $\mathbf{z}_t$  and then convert the output to a denoised estimate of  $\mathbf{z}_t$ , as if we had trained a denoiser network  $\mathbf{x}_\theta(\mathbf{z}_t, \lambda_t)$  directly. This reparameterisation property can be exceptionally advantageous. In this work, we explicitly train neither a score nor a denoiser network but rather use the  $\mathbf{v}$ -prediction parameterisation [35]; we describe this in detail in Section 2.7.4.

### 2.7.3 Noise Schedule

We formalise the notion that  $\mathbf{z}_t$  is increasingly noisy by defining the log signal-to-noise ratio

$$\lambda_t = \log\left(\frac{\alpha_t^2}{\sigma_t^2}\right) \in [\lambda_{\min}, \lambda_{\max}] \quad (2.59)$$

as a strictly monotonically decreasing function  $f_\Lambda$  of time  $t \in [0, 1]$ , known as the *noise schedule*.

In this work, we use a truncated continuous-time version of the  $\alpha$ -cosine schedule [26], introduced in its original discrete-time form by Nichol and Dhariwal [26]. The  $\alpha$ -cosine schedule was motivated by the fact that the ‘linear’ schedule introduced in prior work by Ho et al. [12] causes  $\alpha_t$  to fall to zero more quickly than is optimal. Nichol and Dhariwal empirically found that this induces too much noise in the latter stages of the forward diffusion process; as such, the latent variables  $\mathbf{z}_t$  in these stages contribute little to sample quality. In response, they proposed the original discrete-time  $\alpha$ -cosine schedule. In this work, we use a continuous-time diffusion model and therefore use an adapted model described in [16]. More formally, we define:

$$\lambda_t = f_\Lambda(t) = -2 \log\left(\tan\left(\frac{\pi}{2}(t_0 + t(t_1 - t_0))\right)\right) \quad (2.60)$$

where  $t_0$  and  $t_1$  truncate  $f_\Lambda(t)$  to the desired range  $[\lambda_{\min}, \lambda_{\max}]$  for  $t \in [0, 1]$ , and are themselves defined as:

$$t_0 = \frac{2}{\pi} \arctan\left(\exp\left(-\frac{1}{2}\lambda_{\max}\right)\right) \quad (2.61)$$

$$t_1 = \frac{2}{\pi} \arctan\left(\exp\left(-\frac{1}{2}\lambda_{\min}\right)\right) \quad (2.62)$$

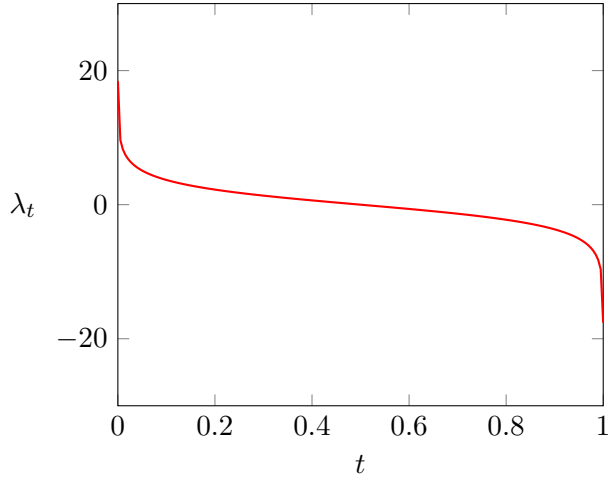


Figure 2.3: Relationship between time  $t$  and the log signal-to-noise ratio  $\lambda_t$  for the truncated continuous-time  $\alpha$ -cosine noise schedule  $f_\Lambda(t)$  as defined in Equation 2.60 with  $\lambda_{\min} = -30$  and  $\lambda_{\max} = 30$ . The horizontal axis is time  $t \in [0, 1]$ ; the vertical axis is  $\lambda_t = f_\Lambda(t) \in [\lambda_{\min}, \lambda_{\max}] = [-30, 30]$ .

Figure 2.3 visualises how the log signal-to-noise ratio  $\lambda_t \in [\lambda_{\min}, \lambda_{\max}]$  varies with time  $t \in [0, 1]$  using the  $\alpha$ -cosine schedule detailed above.

We can compute  $\alpha_t$  and  $\sigma_t$  from either  $\lambda_t$  or  $t$  via the following equations:

$$\alpha_t = \sqrt{S(\lambda_t)} = \cos\left(\frac{\pi}{2}(t_0 + t(t_1 - t_0))\right) \quad (2.63)$$

$$\sigma_t = \sqrt{S(-\lambda_t)} = \sin\left(\frac{\pi}{2}(t_0 + t(t_1 - t_0))\right) \quad (2.64)$$

where  $S$  is the sigmoid function. Figure 2.4 visualises how the values of  $\alpha_t$  and  $\sigma_t$  vary with time  $t \in [0, 1]$  using the  $\alpha$ -cosine schedule detailed above.

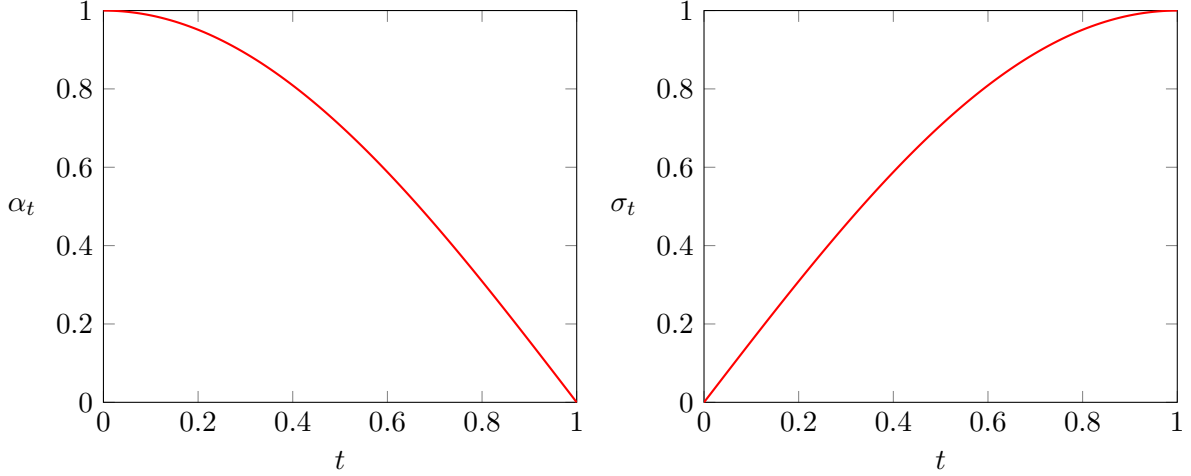


Figure 2.4: Relationship between time  $t$  and  $\alpha_t$  (left) and  $\sigma_t$  (right) for the same truncated continuous-time  $\alpha$ -cosine noise schedule as that in Figure 2.3. The horizontal axis is time  $t \in [0, 1]$ ; the vertical axis is the value of  $\alpha_t$  (left) and  $\sigma_t$  (right).

We can, in theory, use two different noise schedules: one to train the model and another to generate new samples. During training, the noise schedule affects the variance of the gradients [19]. During generation, we typically want to use a noise schedule that optimises the quality of the generated samples. However, in this work, we use the  $\alpha$ -cosine schedule for training and

generation, as we found it to provide empirically good results for both. During training, we sampling  $t \sim \mathcal{U}(0, 1)$  uniformly at random, then compute  $\lambda = f_\Lambda(t)$ , which equates to sampling  $\lambda \sim p_\Lambda(\lambda)$ , where  $p_\Lambda(\lambda)$  is the probability density function for the  $\alpha$ -cosine schedule, and given by:

$$p_\Lambda(\lambda) = \frac{1}{2\pi(t_1 - t_0)} \operatorname{sech}\left(\frac{\lambda}{2}\right) \quad (2.65)$$

Figure 2.5 displays the probability density function.

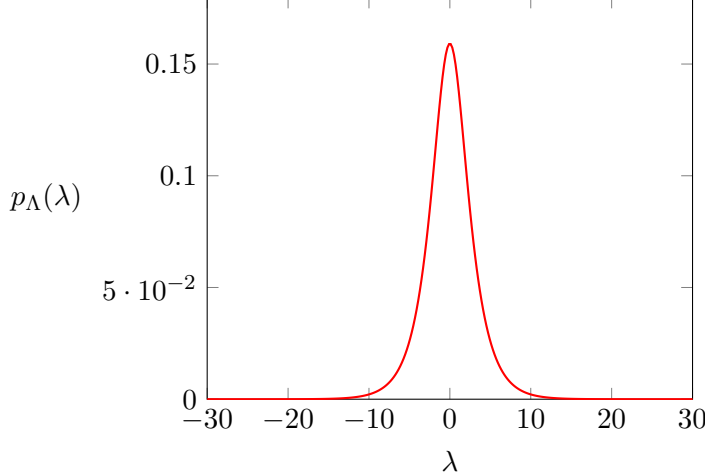


Figure 2.5: Probability density function  $p_\Lambda(\lambda)$  for the same truncated continuous-time  $\alpha$ -cosine schedule as that in Figure 2.3. The horizontal axis is the log signal-to-noise ratio  $\lambda \in [\lambda_{\min}, \lambda_{\max}]$ ; the vertical axis is the corresponding probability density  $p_\Lambda$ .

#### 2.7.4 Parameterisations

In Section 2.7.2, we defined our reverse-time generative model  $p_\theta(\mathbf{x})$  in terms of a denoiser network  $\hat{\mathbf{x}}_\theta(\mathbf{z}_t, \lambda_t)$ . The network takes as input some noisy latent variable  $\mathbf{z}_t$  and a log signal-to-noise ratio  $\lambda_t$  and subsequently outputs a denoised estimate of the latent. Training a neural network to predict  $\mathbf{x} \approx \hat{\mathbf{x}}_\theta(\mathbf{z}_t, \lambda_t)$  directly is referred to as the  $\mathbf{x}$ -prediction parameterisation, but is seldom adopted in the broader literature due to sub-optimal sample quality [12]. Recent diffusion models instead typically adopted different parameterisations, most commonly the  $\epsilon$ -prediction parameterisation (see e.g. [12, 14, 33]). In this framework, we instead train a neural network to predict the noise  $\epsilon \approx \hat{\epsilon}_\theta(\mathbf{z}_t, \lambda_t)$ , from which we can compute a denoised estimate of noisy latent  $\mathbf{z}_t$  via the relationship:

$$\hat{\mathbf{x}}_\theta(\mathbf{z}_t, \lambda_t) = \frac{1}{\alpha_t} (\mathbf{z}_t - \sigma_t \hat{\epsilon}_\theta(\mathbf{z}_t, \lambda_t)) \quad (2.66)$$

In practice, the differences in sample quality that arise from employing different parameterisations are due to the various loss functions employing different implicit weighting functions; we explore this in more detail in Section 2.7.6.

In this work, we employ the  $\mathbf{v}$ -prediction parameterisation, introduced originally by Salimans and Ho [35], and commonly employed in video diffusion models (see e.g. [15, 11]). The  $\mathbf{v}$ -prediction parameterisation was introduced initially to facilitate progressive distillation for faster sampling, though we utilise it here for its additional benefits highlighted by Ho et al. [11]. Namely, faster convergence of sample quality and prevention of temporal colour shifting observed with  $\epsilon$ -prediction video diffusion models. Let  $\psi$  be:

$$\psi = \arctan\left(\frac{\sigma_t}{\alpha_t}\right) = \frac{\pi}{2}(t_0 + t(t_1 - t_0)) \quad (2.67)$$

Formally, for a given datapoint  $\mathbf{x}$ , we define the velocity of latent  $\mathbf{z}_t$  as:

$$\mathbf{v}_t = \frac{d\mathbf{z}_t}{d\psi} = \cos(\psi)\boldsymbol{\epsilon} - \sin(\psi)\mathbf{x} \quad (2.68)$$

$$= \alpha_t \boldsymbol{\epsilon} - \sigma_t \mathbf{x} \quad (2.69)$$

where  $\boldsymbol{\epsilon} \sim \mathcal{N}(\mathbf{0}, \mathbf{I})$  is multivariate standard Gaussian noise. We train our neural network  $\hat{\mathbf{v}}_\theta(\mathbf{z}_t, \lambda_t)$  to predict  $\mathbf{v}_t$  by minimising the following loss function, defined per datapoint  $\mathbf{x}$  as:

$$\mathbb{E}_{\lambda \sim p_\Lambda(\lambda), \boldsymbol{\epsilon} \sim \mathcal{N}(\mathbf{0}, \mathbf{I})} [\|\mathbf{v}_t - \hat{\mathbf{v}}_\theta(\mathbf{z}_t, \lambda_t)\|_2^2] \quad (2.70)$$

We can trivially convert our estimate of the velocity  $\hat{\mathbf{v}}_\theta(\mathbf{z}_t, \lambda_t)$  into an estimate of the denoised latent  $\hat{\mathbf{x}}_\theta(\mathbf{z}_t, \lambda_t)$ , an estimate of the noise  $\hat{\boldsymbol{\epsilon}}_\theta(\mathbf{z}_t, \lambda_t)$ , or an estimate of the score  $\hat{\mathbf{s}}_\theta(\mathbf{z}_t, \lambda_t)$  due to the following relationships:

$$\mathbf{x} = \alpha_t \mathbf{z}_t - \sigma_t \mathbf{v}_t \quad (2.71)$$

$$\boldsymbol{\epsilon} = \sigma_t \mathbf{z}_t + \alpha_t \mathbf{v}_t \quad (2.72)$$

$$\nabla_{\mathbf{z}_t} q(\mathbf{z}_t) = -\mathbf{z}_t - \frac{\alpha_t}{\sigma_t} \mathbf{v}_t \quad (2.73)$$

### 2.7.5 ELBO for Diffusion Models

We can interpret the variance-preserving diffusion model used in this work as an MHVAE with several additional restrictions. Firstly, the dimensionality of each latent  $\mathbf{z}_t$  equals the dimensionality of the observed variable. Secondly, we have pre-defined  $q(\mathbf{z}_t | \mathbf{z}_s)$  where  $0 \leq s < t \leq 1$  as a Gaussian diffusion process with no learnable inference parameters. Finally, the marginal distribution of the final latent  $q(\mathbf{z}_1)$  is approximately the multivariate standard Gaussian  $\mathcal{N}(\mathbf{0}, \mathbf{I})$ , and thus holds effectively no information about the observed variable  $\mathbf{x}$ . VAEs and MHVAEs do not typically have these restrictions. Nonetheless, much like VAEs and MHVAEs, we can optimise the generative parameters  $\theta$  of diffusion models by minimising the ELBO loss. As a notable example, Sohl-Dickstein et al. [37] optimised the original discrete-time diffusion model via the ELBO loss.

For a given datapoint  $\mathbf{x}$ , we define  $\mathcal{L}_\Lambda(\lambda)$  as the KL divergence of  $q(\mathbf{z}_t, \dots, \mathbf{z}_1 | \mathbf{x})$  from  $p_\theta(\mathbf{z}_t, \dots, \mathbf{z}_1)$  for a subset of timesteps from  $t = f_\Lambda^{-1}(\lambda)$  to 1 for datapoint  $\mathbf{x}$ :

$$\mathcal{L}_\Lambda(\lambda) = D_{\text{KL}}(q(\mathbf{z}_t, \dots, \mathbf{z}_1 | \mathbf{x}) \| p_\theta(\mathbf{z}_t, \dots, \mathbf{z}_1)) \quad (2.74)$$

Notably,  $\mathcal{L}_\Lambda(\lambda)$  equates to  $\mathcal{L}_T(t)$  defined in Equation 2.31 under a simple change of variable:

$$\mathcal{L}_\Lambda(\lambda) = \mathcal{L}_T(t = f_\Lambda^{-1}(\lambda)) \quad (2.75)$$

Similarly, we can reformulate the ELBO loss for a continuous-time MHVAE given in Equation 2.35 to provide the ELBO loss in terms of the log signal-to-noise ratio  $\lambda$ ; it is given per datapoint  $\mathbf{x}$  by:

$$\mathcal{L}_{\text{ELBO}}(\mathbf{x}) = \mathbb{E}_{\mathbf{z}_0 \sim q(\mathbf{z}_0, \mathbf{x})} [-\log p_\theta(\mathbf{x} | \mathbf{z}_0)] + \mathcal{L}_\Lambda(\lambda_{\max}) \quad (2.76)$$

$$= \underbrace{\mathbb{E}_{\mathbf{z}_0 \sim q(\mathbf{z}_0, \mathbf{x})} [-\log p_\theta(\mathbf{x} | \mathbf{z}_0)]}_{\text{Reconstruction Loss}} + \underbrace{\mathcal{L}_\Lambda(\lambda_{\min}) + \int_{\lambda_{\min}}^{\lambda_{\max}} \mathcal{L}'_\Lambda(\lambda) d\lambda}_{\text{Prior Loss}} \quad (2.77)$$

With sufficiently large  $\lambda_{\max}$ , the reconstruction loss is approximately zero since we can almost perfectly reconstruct  $\mathbf{x}$  from  $\mathbf{z}_0$ —this is particularly true for discrete  $\mathbf{x}$ . Mathematically, as  $\lambda_{\max} \rightarrow \infty$ , we have:

$$\lim_{\lambda_{\max} \rightarrow \infty} q(\mathbf{z}_0 | \mathbf{x}) = \delta(\mathbf{z}_0 - \mathbf{x}) \quad (2.78)$$

where  $\delta$  is the Dirac delta distribution. Similarly, with sufficiently small  $\lambda_{\min}$ , the prior loss is approximately zero; as  $\lambda_{\min} \rightarrow -\infty$ , we have:

$$\lim_{\lambda_{\min} \rightarrow -\infty} q(\mathbf{z}_t | \mathbf{x}) = \mathcal{N}(\mathbf{0}, \mathbf{I}) = p_\theta(\mathbf{z}_t) \quad (2.79)$$

so the KL divergence prior loss term likewise approaches zero.

In Appendix C of [19], Kingma and Gao showed that  $\mathcal{L}'_\Lambda(\lambda)$ —which, with a slight abuse of terminology, they refer to as the *time derivative*—simplifies to a remarkable degree:

$$\mathcal{L}'_\Lambda(\lambda) = \frac{d}{d\lambda} \mathcal{L}_\Lambda(\lambda) = \frac{1}{2} \mathbb{E}_{\epsilon \sim \mathcal{N}(\mathbf{0}, \mathbf{I})} [\|\epsilon - \hat{\epsilon}_\theta(\mathbf{z}_t, \lambda)\|_2^2] \quad (2.80)$$

### 2.7.6 Weighted Loss

Most diffusion models in the broader literature—including state-of-the-art models—do not optimise their parameters  $\theta$  via minimisation of the ELBO loss. In practice, the various objectives used are all special cases of a *weighted loss* [19], which is defined per datapoint  $\mathbf{x}$  as:

$$\mathcal{L}_{WL} = w(\lambda_{\min}) \mathcal{L}_\Lambda(\lambda_{\min}) + \int_{\lambda_{\min}}^{\lambda_{\max}} w(\lambda) \mathcal{L}'_\Lambda(\lambda) d\lambda \quad (2.81)$$

where  $w(\lambda)$  is a weighting function. Note that, assuming the reconstruction loss is approximately zero, the ELBO loss given in Equation 2.77 is a special case of the weighted loss  $\mathcal{L}_{WL}$  with  $w(\lambda) = 1$ . Substituting the form of  $\mathcal{L}'_\Lambda(\lambda)$  given in Equation 2.80 yields the following form for the weighted loss:

$$\mathcal{L}_{WL} = w(\lambda_{\min}) \mathcal{L}_\Lambda(\lambda_{\min}) + \frac{1}{2} \int_{\lambda_{\min}}^{\lambda_{\max}} w(\lambda) \mathbb{E}_{\epsilon \sim \mathcal{N}(\mathbf{0}, \mathbf{I})} [\|\epsilon - \hat{\epsilon}_\theta(\mathbf{z}_t, \lambda)\|_2^2] d\lambda \quad (2.82)$$

This form provides several useful insights. Since the first term—the weighted prior loss—contains no learnable parameters, minimisation of the weighted loss  $\mathcal{L}_{WL}$  equates to minimisation of the intractable integral. In practice, we minimise the integral via an importance-weighted Monte Carlo integrator:

$$\int_{\lambda_{\min}}^{\lambda_{\max}} w(\lambda) \mathbb{E}_{\epsilon \sim \mathcal{N}(\mathbf{0}, \mathbf{I})} [\|\epsilon - \hat{\epsilon}_\theta(\mathbf{z}_t, \lambda)\|_2^2] d\lambda = \mathbb{E}_{\lambda \sim p_\Lambda(\lambda)} \left[ \frac{w(\lambda)}{p_\Lambda(\lambda)} \mathbb{E}_{\epsilon \sim \mathcal{N}(\mathbf{0}, \mathbf{I})} [\|\epsilon - \hat{\epsilon}_\theta(\mathbf{z}_t, \lambda)\|_2^2] \right] \quad (2.83)$$

$$= \mathbb{E}_{\lambda \sim p_\Lambda(\lambda), \epsilon \sim \mathcal{N}(\mathbf{0}, \mathbf{I})} \left[ \frac{w(\lambda)}{p_\Lambda(\lambda)} \|\epsilon - \hat{\epsilon}_\theta(\mathbf{z}_t, \lambda)\|_2^2 \right] \quad (2.84)$$

$$\simeq \frac{w(\lambda)}{p_\Lambda(\lambda)} \|\epsilon - \hat{\epsilon}_\theta(\mathbf{z}_t, \lambda)\|_2^2 \quad (2.85)$$

Notable further analysis by Kingma and Gao [19] shows that the weighted loss also has a likelihood-based interpretation. Simple integration by parts enables us to write the weighted loss as:

$$\mathcal{L}_{WL} = w(\lambda_{\max}) \mathcal{L}_\Lambda(\lambda_{\max}) + \int_{\lambda_{\min}}^{\lambda_{\max}} -w'(\lambda) \mathcal{L}_\Lambda(\lambda) d\lambda \quad (2.86)$$

The likelihood-based interpretation comes from the fact that  $\mathcal{L}_\Lambda(\lambda)$  serves as a variational bound on the negative marginal likelihood of the noise-perturbed data  $\mathbf{z}_t \sim q(\mathbf{z}_t | \mathbf{x})$ :

$$\mathcal{L}_\Lambda(\lambda) \geq D_{KL}(q(\mathbf{z}_t | \mathbf{x}) \| p(\mathbf{z}_t)) \quad (2.87)$$

$$= \mathbb{E}_{\mathbf{z}_t \sim q(\mathbf{z}_t | \mathbf{x})} [-\log p(\mathbf{z}_t)] + \mathbb{E}_{\mathbf{z}_t \sim q(\mathbf{z}_t | \mathbf{x})} [\log q(\mathbf{z}_t | \mathbf{x})] \quad (2.88)$$

As such, minimisation of  $\mathcal{L}_\Lambda(\lambda)$  equates to maximisation of the expected log-likelihood of the noise-perturbed data  $\mathbf{z}_t \sim q(\mathbf{z}_t|\mathbf{x})$  with noise level  $\lambda$ . If the weighting function  $w(\lambda)$  is a monotonically decreasing function of  $\lambda \in [\lambda_{\min}, \lambda_{\max}]$ , then by definition  $-w'(\lambda)$  will be positive for all  $\lambda \in [\lambda_{\min}, \lambda_{\max}]$ . In which case, minimisation of  $\mathcal{L}_{WL}$  itself equates to maximisation of the weighted expected log-likelihood of the noise-perturbed data  $\mathbf{z}_t \sim q(\mathbf{z}_t|\mathbf{x})$  with weighting  $-w'(\lambda)$ .

Kingma and Gao's [19] analysis directly justifies our use of the  $\mathbf{v}$ -prediction parameterisation with the  $\alpha$ -cosine noise schedule. The  $\alpha$ -cosine schedule used in conjunction with the  $\mathbf{v}$ -prediction parameterisation loss function given in Equation 2.70 equates to the weighted loss with:

$$w(\lambda) = \frac{1}{2\pi(t_1 - t_0)} \exp\left(-\frac{\lambda}{2}\right) \quad (2.89)$$

$$-w'(\lambda) = \frac{1}{4\pi(t_1 - t_0)} \exp\left(-\frac{\lambda}{2}\right) \quad (2.90)$$

Figure 2.6 shows the weighting function  $w(\lambda)$  and the negative of its derivative  $-w'(\lambda)$  for the  $\mathbf{v}$ -parameterisation loss. As evident from the graphs, the weighting function  $w(\lambda)$  is a monotonically decreasing function of  $\lambda$ , and as such  $-w'(\lambda)$  is positive for all  $\lambda \in [\lambda_{\min}, \lambda_{\max}]$ . Therefore, during training, we are maximising a weighted expected log-likelihood of noise-perturbed data  $\mathbf{z}_t \sim q(\mathbf{z}_t|\mathbf{x})$  for all  $\lambda \in [\lambda_{\min}, \lambda_{\max}]$ . In contrast, most diffusion models in the broader literature (see e.g. [12, 26, 33]) undergo training with non-monotonic weighting functions. In such cases, for noise levels whereby  $-w'(\lambda)$  is negative, the weighted loss has a counterintuitive interpretation of minimisation of the weighted expected log-likelihood of the noise-perturbed data  $\mathbf{z}_t \sim q(\mathbf{z}_t|\mathbf{x})$ .

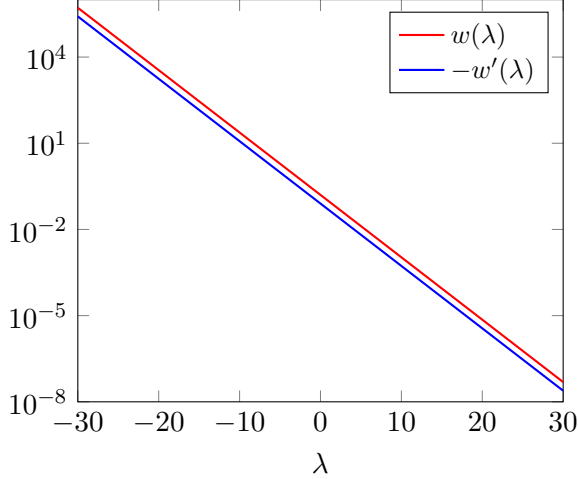


Figure 2.6: Relationship between the log signal-to-noise ratio  $\lambda$  and the functions  $w(\lambda)$  and  $-w'(\lambda)$  for the  $\mathbf{v}$ -parameterisation with the same truncated continuous-time  $\alpha$ -cosine schedule as that in Figure 2.3. The horizontal axis is the log signal-to-noise level  $\lambda$ ; the vertical axis is the value of  $w(\lambda)$  and  $-w'(\lambda)$ ; the vertical axis is logarithmic.

### 2.7.7 Imputation for Conditional Generation

In Section 2.2, we introduced the concept of conditional generation. In this work, however, we do not train a conditional model explicitly. Instead, we utilise *reconstruction-guided sampling* [15]: a sophisticated technique that derives a conditional model approximately from an unconditional model. More specifically, reconstruction-guided sampling facilitates the conditional generation of the unknown dimensions of some observed datapoint  $\mathbf{x}$  given the known dimensions. Deriving such a conditional model approximately from an unconditional model is advantageous:

it enables us to train only a single unconditional model, which we can then flexibly use to facilitate the conditional generation of any unknown subset of dimensions. In this work, we utilise reconstruction-guided sampling to facilitate three distinct conditional generation tasks: temporal interpolation, forecasting, and autoregressive generation of arbitrarily long samples.

Reconstruction-guided sampling extends a prior technique known as *imputation*, introduced by Song et al. [40]. Thus, we first introduce imputation for completeness and to better motivate our use of reconstruction-guided sampling in this work.

We denote by  $\Omega(\mathbf{x})$  and  $\bar{\Omega}(\mathbf{x})$  the known and unknown dimensions of some observed datapoint  $\mathbf{x}$ , respectively. Formally, our goal is to derive the following conditional model without training it explicitly:

$$p_\theta(\bar{\Omega}(\mathbf{x})|\Omega(\mathbf{x})) \quad (2.91)$$

We can write the forward diffusion process for the unknown dimensions as the following SDE:

$$d\bar{\Omega}(\mathbf{z}_t) = \mathbf{f}(\bar{\Omega}(\mathbf{z}_t), t) + g(t)d\mathbf{w}_t \quad (2.92)$$

Anderson [2] shows that the corresponding reverse-time SDE conditioned on the known dimensions  $\Omega(\mathbf{x})$  is given by:

$$d\bar{\Omega}(\mathbf{z}_t) = \left[ \mathbf{f}(\bar{\Omega}(\mathbf{z}_t), t) - g(t)^2 \nabla_{\bar{\Omega}(\mathbf{z}_t)} \log q(\bar{\Omega}(\mathbf{z}_t)|\Omega(\mathbf{x})) \right] dt + g(t)d\bar{\mathbf{w}}_t \quad (2.93)$$

Although  $q(\bar{\Omega}(\mathbf{z}_t)|\Omega(\mathbf{x}))$  is intractable, we can approximate it as follows:

$$q(\bar{\Omega}(\mathbf{z}_t)|\Omega(\mathbf{x})) = \int q(\bar{\Omega}(\mathbf{z}_t), \Omega(\mathbf{z}_t)|\Omega(\mathbf{x})) d\Omega(\mathbf{z}_t) \quad (2.94)$$

$$= \int q(\bar{\Omega}(\mathbf{z}_t)|\Omega(\mathbf{x}), \Omega(\mathbf{z}_t)) q(\Omega(\mathbf{z}_t)|\Omega(\mathbf{x})) d\Omega(\mathbf{z}_t) \quad (2.95)$$

$$= \mathbb{E}_{\Omega(\mathbf{z}_t) \sim q(\Omega(\mathbf{z}_t)|\Omega(\mathbf{x}))} [q(\bar{\Omega}(\mathbf{z}_t)|\Omega(\mathbf{x}), \Omega(\mathbf{z}_t))] \quad (2.96)$$

$$\approx \mathbb{E}_{\Omega(\mathbf{z}_t) \sim q(\Omega(\mathbf{z}_t)|\Omega(\mathbf{x}))} [q(\bar{\Omega}(\mathbf{z}_t)|\Omega(\mathbf{z}_t))] \quad (2.97)$$

Song et al. [40] argue that the approximation in Equation 2.97 is appropriate since for small  $t$ ,  $\Omega(\mathbf{x})$  is almost the same as  $\Omega(\mathbf{z}_t)$ ; and for larger  $t$ ,  $\Omega(\mathbf{x})$  is further away from  $\bar{\Omega}(\mathbf{z}_t)$  in the Markov chain, and thus has a smaller impact on  $\bar{\Omega}(\mathbf{z}_t)$ . Assuming the approximation holds, we can derive an unbiased estimator of  $q(\bar{\Omega}(\mathbf{z}_t)|\Omega(\mathbf{x}))$  as:

$$q(\bar{\Omega}(\mathbf{z}_t)|\Omega(\mathbf{x})) \approx \mathbb{E}_{\Omega(\mathbf{z}_t) \sim q(\Omega(\mathbf{z}_t)|\Omega(\mathbf{x}))} [q(\bar{\Omega}(\mathbf{z}_t)|\Omega(\mathbf{z}_t))] \simeq q(\bar{\Omega}(\mathbf{z}_t)|\Omega(\mathbf{z}_t)) \quad (2.98)$$

The score of the natural logarithm of the unbiased estimator is given by:

$$\nabla_{\bar{\Omega}(\mathbf{z}_t)} \log q(\bar{\Omega}(\mathbf{z}_t)|\Omega(\mathbf{z}_t)) = \nabla_{\bar{\Omega}(\mathbf{z}_t)} \log q(\bar{\Omega}(\mathbf{z}_t), \Omega(\mathbf{z}_t)) - \nabla_{\bar{\Omega}(\mathbf{z}_t)} \log q(\Omega(\mathbf{z}_t)) \quad (2.99)$$

$$= \nabla_{\bar{\Omega}(\mathbf{z}_t)} \log q(\bar{\Omega}(\mathbf{z}_t), \Omega(\mathbf{z}_t)) \quad (2.100)$$

$$= \nabla_{\bar{\Omega}(\mathbf{z}_t)} \log q([\bar{\Omega}(\mathbf{z}_t); \Omega(\mathbf{z}_t)]) \quad (2.101)$$

where  $[\bar{\Omega}(\mathbf{z}_t); \Omega(\mathbf{z}_t)]$  denotes a vector such that:

$$\Omega([\bar{\Omega}(\mathbf{z}_t); \Omega(\mathbf{z}_t)]) = \Omega(\mathbf{z}_t) \quad (2.102)$$

$$\bar{\Omega}([\bar{\Omega}(\mathbf{z}_t); \Omega(\mathbf{z}_t)]) = \bar{\Omega}(\mathbf{z}_t) \quad (2.103)$$

Thus, assuming the assumption given in Equation 2.97 holds, we can consequently approximate the reverse-time SDE conditioned on  $\Omega(\mathbf{x})$  given in Equation 2.93 as follows:

$$d\bar{\Omega}(\mathbf{z}_t) = \left[ \mathbf{f}(\bar{\Omega}(\mathbf{z}_t), t) - g(t)^2 \nabla_{\bar{\Omega}(\mathbf{z}_t)} \log q([\bar{\Omega}(\mathbf{z}_t); \Omega(\mathbf{z}_t)]) \right] dt + g(t)d\bar{\mathbf{w}}_t \quad (2.104)$$

If we have a perfect score model,  $\mathbf{s}_\theta(\mathbf{z}_t, \lambda_t) = \nabla_{\mathbf{z}_t} q(\mathbf{z}_t)$ , then the reverse-time SDE is thus given by:

$$d\bar{\Omega}(\mathbf{z}_t) = [\mathbf{f}(\bar{\Omega}(\mathbf{z}_t), t) - g(t)^2 \mathbf{s}_\theta([\bar{\Omega}(\mathbf{z}_t); \Omega(\mathbf{z}_t)], \lambda_t)] dt + g(t) d\bar{\mathbf{w}}_t \quad (2.105)$$

To provide a more intuitive link between Equation 2.105 and the generative procedure in Section ??, we also define the imputation method as a conditional denoiser  $\hat{\mathbf{x}}_\theta^C(\mathbf{z}_t, \lambda_t, \Omega(\mathbf{x}))$ , which takes the known dimensions of  $\mathbf{x}$  as input:

$$\hat{\mathbf{x}}_\theta^C(\mathbf{z}_t, \lambda_t, \Omega(\mathbf{x})) = \bar{\Omega}(\hat{\mathbf{x}}_\theta([\bar{\Omega}(\mathbf{z}_t); \Omega(\mathbf{z}_t)], \lambda_t)) \quad (2.106)$$

Thus, the imputation method for conditional generation yields only a slight adjustment to the generative procedure defined in Section 2.7.2. Namely, at each step of the discrete-time ancestral sampler, we replace the dimensions of  $\mathbf{z}_t$  corresponding to the known dimensions of  $\mathbf{x}$  with an exact sample from the forward process:  $\Omega(\mathbf{z}_t) \sim q(\Omega(\mathbf{z}_t) | \Omega(\mathbf{x}))$ .

### 2.7.8 Reconstruction-Guided Sampling for Conditional Generation

Ho et al. [15] showed that the imputation process produces incoherent samples when applied to video diffusion models. Namely, although a given  $\bar{\Omega}(\mathbf{x})$  will often appear reasonable in isolation, it will often not be coherent with  $\Omega(\mathbf{x})$ . This incoherency is likely because the assumption in Equation 2.97 does not hold for all  $t \in [0, 1]$ . Avoiding the assumption, we instead construct an unbiased estimator for  $q(\bar{\Omega}(\mathbf{z}_t) | \Omega(\mathbf{x}))$  as:

$$q(\bar{\Omega}(\mathbf{z}_t) | \Omega(\mathbf{x})) = \mathbb{E}_{\Omega(\mathbf{z}_t) \sim q(\Omega(\mathbf{z}_t) | \Omega(\mathbf{x}))} [q(\bar{\Omega}(\mathbf{z}_t) | \Omega(\mathbf{x}), \Omega(\mathbf{z}_t))] \simeq q(\bar{\Omega}(\mathbf{z}_t) | \Omega(\mathbf{x}), \Omega(\mathbf{z}_t)) \quad (2.107)$$

The score of the natural logarithm of the unbiased estimator is given by:

$$\nabla_{\bar{\Omega}(\mathbf{z}_t)} \log q(\bar{\Omega}(\mathbf{z}_t) | \Omega(\mathbf{x}), \Omega(\mathbf{z}_t)) = \nabla_{\bar{\Omega}(\mathbf{z}_t)} \log q(\bar{\Omega}(\mathbf{z}_t), \Omega(\mathbf{x}), \Omega(\mathbf{z}_t)) - \nabla_{\bar{\Omega}(\mathbf{z}_t)} \log q(\Omega(\mathbf{z}_t), \Omega(\mathbf{x})) \quad (2.108)$$

$$= \nabla_{\bar{\Omega}(\mathbf{z}_t)} \log q(\bar{\Omega}(\mathbf{z}_t), \Omega(\mathbf{x}), \Omega(\mathbf{z}_t)) \quad (2.109)$$

$$= \nabla_{\bar{\Omega}(\mathbf{z}_t)} \log q(\bar{\Omega}(\mathbf{z}_t), \Omega(\mathbf{z}_t)) + \nabla_{\bar{\Omega}(\mathbf{z}_t)} \log q(\Omega(\mathbf{x}) | \bar{\Omega}(\mathbf{z}_t), \Omega(\mathbf{z}_t)) \quad (2.110)$$

$$= \nabla_{\bar{\Omega}(\mathbf{z}_t)} \log q([\bar{\Omega}(\mathbf{z}_t); \Omega(\mathbf{z}_t)]) + \nabla_{\bar{\Omega}(\mathbf{z}_t)} \log q(\Omega(\mathbf{x}) | [\bar{\Omega}(\mathbf{z}_t); \Omega(\mathbf{z}_t)]) \quad (2.111)$$

The second term in Equation 2.111 is missing in the imputation approach. Plugging in this missing term would make conditional sampling exact. However, since  $q(\Omega(\mathbf{x}) | [\bar{\Omega}(\mathbf{z}_t); \Omega(\mathbf{z}_t)])$  is not available in closed form, we must approximate it. Ho et al. [15] proposed to approximate it with a multivariate Gaussian of the form:

$$q(\Omega(\mathbf{x}) | [\bar{\Omega}(\mathbf{z}_t); \Omega(\mathbf{z}_t)]) \approx \mathcal{N}\left(\Omega(\mathbf{x}); \Omega(\hat{\mathbf{x}}_\theta([\bar{\Omega}(\mathbf{z}_t); \Omega(\mathbf{z}_t)], \lambda_t)), \left(\frac{\sigma_t^2}{\alpha_t^2}\right) \mathbf{I}\right) \quad (2.112)$$

Under this approximation, the second term of Equation 2.111 is thus itself approximated by:

$$\nabla_{\bar{\Omega}(\mathbf{z}_t)} \log q(\Omega(\mathbf{x}) | [\bar{\Omega}(\mathbf{z}_t); \Omega(\mathbf{z}_t)]) \approx -\frac{\alpha_t^2}{2\sigma_t^2} \nabla_{\bar{\Omega}(\mathbf{z}_t)} \|\Omega(\mathbf{x}) - \Omega(\hat{\mathbf{x}}_\theta([\bar{\Omega}(\mathbf{z}_t); \Omega(\mathbf{z}_t)], \lambda_t))\|_2^2 \quad (2.113)$$

Ho et al. [15] interpret the inclusion of this term—absent in the imputation method—as a form of *guidance* based on the model’s reconstruction of the conditioning data. They found empirically that—as with other forms of guidance—including a large weighting term  $w_r > 1$  tends to improve sample quality further. They refer to this technique as *reconstruction-guided sampling*. Formally, assuming we have a perfect score model  $\mathbf{s}_\theta(\mathbf{z}_t, \lambda_t) = \nabla_{\mathbf{z}_t} q(\mathbf{z}_t)$ , reconstruction-guided sampling

derives a conditional model from an unconditional model by approximating the score given in Equation 2.93 by:

$$\nabla_{\bar{\Omega}(\mathbf{z}_t)} \log q(\bar{\Omega}(\mathbf{z}_t) | \Omega(\mathbf{x})) \approx \mathbf{s}_\theta([\bar{\Omega}(\mathbf{z}_t); \Omega(\mathbf{z}_t)], \lambda_t) \quad (2.114)$$

$$- \frac{w_r \alpha_t^2}{2\sigma_t^2} \nabla_{\bar{\Omega}(\mathbf{z}_t)} \|\Omega(\mathbf{x}) - \Omega(\hat{\mathbf{x}}_\theta([\bar{\Omega}(\mathbf{z}_t); \Omega(\mathbf{z}_t)], \lambda_t))\|_2^2 \quad (2.115)$$

Writing the reconstruction-guidance method as a conditional denoiser  $\hat{\mathbf{x}}_\theta^C(\mathbf{z}_t, \lambda_t, \Omega(\mathbf{x}))$  yields:

$$\hat{\mathbf{x}}_\theta^C(\mathbf{z}_t, \lambda_t, \Omega(\mathbf{x})) = \bar{\Omega}(\hat{\mathbf{x}}_\theta([\bar{\Omega}(\mathbf{z}_t); \Omega(\mathbf{z}_t)], \lambda_t)) - \frac{w_r \alpha_t}{2} \nabla_{\bar{\Omega}(\mathbf{z}_t)} \|\Omega(\mathbf{x}) - \Omega(\hat{\mathbf{x}}_\theta([\bar{\Omega}(\mathbf{z}_t); \Omega(\mathbf{z}_t)]))\|_2^2 \quad (2.116)$$

### 2.7.9 3D U-Net

In this work, our  $\mathbf{v}$ -prediction model  $\mathbf{v}_\theta(\mathbf{z}_t, \lambda_t)$  uses the 3D U-Net architecture from [15]. The 3D U-Net architecture is an extension of the 2D U-Net [32, 36], the standard architecture employed in recent work on image modelling. It comprises a spatial downsampling pass followed by a spatial upsampling pass with skip connections to the downsampling pass activations. The network contains layers of space-only 3D convolutional residual blocks [15], with each block followed by a spatial attention block [42, 43, 6], which treats the temporal axis as a batch axis. A temporal attention block follows each spatial attention block, performing attention over the temporal axis and treating the two spatial axes as batch axes. This form of factorised space-time attention is known for its computational efficiency [3, 4, 13].

---

# Chapter 3

## Related Work

Recent developments in generative artificial intelligence have unveiled new opportunities within the realm of climate science. Researchers are increasingly exploring generative AI techniques to address pressing issues. We can broadly classify a considerable proportion of this research into two main categories. The first encompasses machine-learning-based statistical downscaling: generating high-resolution climate simulations from low-resolution simulations. The second category involves using generative models for nowcasting: forecasting with local detail from the present up to six hours ahead [44].

### 3.1 Statistical Downscaling

As the world’s climate evolves rapidly, the need for reliable simulations based on emission scenarios has become increasingly pressing. Climate simulations provide plausible projections of climate change for different emission pathways. As such, they provide crucial insights for researchers, governments and organisations alike seeking to mitigate the effects of climate change and formulate policies to shape the future of our planet.

Climate simulations exist on a spectrum of spatial and temporal resolutions. Global climate models (GCMs), situated at the lower-resolution end of the spectrum, provide spatial resolutions of 60–300 km and demand relatively low computational resources. However, GCMs necessitate parameterisation schemes to represent the average effects of convection, as explicit representation on the grid is impossible [17]. This simplification serves as a known source of model error with several associated problems, including deficiencies in the daily timing on convection and an inability to represent hourly extremes [10, 9].

Conversely, convection-permitting models (CPMs), a specialised type of regional climate model (RCM) situated at the high-resolution end of the spectrum, offer spatial resolutions of typically only a few kilometres and thus enable explicit representation of convective storms [17]. CPMs employ realistic physical representations of relevant climate processes, providing significant advantages such as realistic representation of hourly rainfall characteristics, including extremes, compared to models that run at coarser spatial scales [18]. High-resolution simulations of this nature facilitate assessments of future risks for extreme events like localised flash flooding; notably, CPMs have shown a substantial increase in hourly precipitation extremes in the UK’s summers, which coarser simulations failed to capture [18]. However, the substantial computational cost of CPMs is a barrier to their wider deployment [17].

Machine-learning-based statistical downscaling presents an alternative approach for generating high-resolution simulations with reduced computational costs. These methods utilise machine learning to establish a statistical relationship between lower-resolution climate variables and higher-resolution values. A notable example of such an approach is the work of Doury et al. [7], who employ a variation of the original U-Net architecture [32] to emulate an RCM with a 12 km spatial resolution based on GCM inputs for regions in France and Spain. However,

### 3.2. NOWCASTING

---

deterministic systems like these tend to generate blurry samples [29] and produce only a single output for each input.

In the domain of stochastic systems, Leinenon et al. [22] apply a generative adversarial network (GAN) [8] to generate time-evolving high-resolution atmospheric fields from low-resolution input sequences. GANs, however, are prone to mode collapse [41], indicating they potentially underestimate the probability of extreme atmospheric events. In contrast, diffusion models better capture the complete data distribution and should not encounter the same issues. Addison et al. [1] present the first application of diffusion models for climate downscaling, showcasing a machine-learning model capable of generating realistic high-resolution precipitation samples based on a physical model that resolves atmospheric convection.

This work, too, employs a diffusion model to generate high-resolution precipitation samples. However, in two significant aspects, our research distinguishes itself from Addison et al.'s [1]. Firstly, while their diffusion model operates on individual daily mean snapshots, we focus on time-evolving hourly mean snapshots, acknowledging the importance of temporal patterns in precipitation and the strong autocorrelation inherent in precipitation data. Daily mean snapshots, as employed by Addison et al., may potentially overlook crucial information such as hourly peaks. These can be important, for example, in the context of flash flooding. Secondly, our research does not concern spatial downscaling; instead, we establish an initial proof of principle for generating realistic time-evolving hourly precipitation sequences. In this respect, much of our work thus concentrates on the unconditional setting.

## 3.2 Nowcasting

Numerical weather prediction (NWP) systems are crucial to modern weather forecasting; they utilise physical equations to generate accurate and realistic predictions several days ahead. However, these systems encounter substantial challenges in producing high-resolution short-term forecasts owing to prevailing computational limitations [45]. In practice, the major limitation of NWP systems is their operational forecast update cycle, which typically spans several hours, whilst phenomena typically exhibit lifetimes of the order of tens of minutes [27]. This limitation has significant implications, as nowcasting directly supports the real-world socioeconomic needs of various sectors that rely on weather-dependent decision-making [45].

Prediction systems typically employ alternative approaches that utilise composite radar observations to address the issue of short lead times. Established probabilistic nowcasting methods (see e.g. [5]) instead predict precipitation using the advection equation with a radar source term.

In recent years, researchers have explored stochastic machine-learning-based nowcasting systems that surpass the reliance on the advection equation to improve the quality of nowcasts. The current state-of-the-art generative model for nowcasting is the GAN-based model proposed by Ravuri et al. [29]. Their GAN-based model provides realistic and spatiotemporally coherent nowcasts with lead times ranging between 5 and 90 minutes.

Although nowcasting is not the central focus of this work, we present preliminary proof-of-principle results for nowcasting using a diffusion model in Section 4.5. The results presented are not directly comparable to those of Ravuri et al. [29], due to our use of a different dataset and the nowcasting implemented encompassing longer timeframes with a lower temporal resolution. Nonetheless, the results provide a promising initial indication of the potential of diffusion models for nowcasting applications and serve to encourage future research into the application of diffusion models for nowcasting purposes. As diffusion models have demonstrated superior performance over GANs in much of the broader literature on generative models (see e.g. [12, 14, 33]), we anticipate this trend will similarly extend to nowcasting applications.

---

# Chapter 4

# Experiments and Results

## 4.1 Dataset

### 4.1.1 UKCP18

For this study, we employ a dataset derived from the United Kingdom Climate Projections 2018 (UKCP18) [25] dataset, the UK Met Office’s latest generational of national climate projections. The broader UKCP18 dataset contains simulations encompassing diverse climate components under various Representative Concentration Pathways (RCPs), which are trajectories for greenhouse gas concentration adopted by the Intergovernmental Panel on Climate Change.

Within the extensive UKCP18 collection, we utilise the first ensemble member of the local-scale precipitation simulations with 2.2 km grid spacing and an hourly temporal resolution. These high-resolution simulations, known as ‘convection-permitting’, possess a resolution sufficient for explicitly representing convective storms [17]. Such a high resolution facilitates improved simulation of small-scale atmospheric phenomena, including the influence of mountains, coastlines and urban areas on precipitation patterns. The hourly 2.2 km resolution data covers 1981–2000, 2021–2040 and 2061–2080 and is exclusively available for RCP8.5 [24], a scenario where greenhouse gas emissions continue to grow unmitigated.

### 4.1.2 Preprocessing

As part of a preprocessing stage before training our diffusion model, we addressed memory limitations inherent in modern GPUs by coarsening the spatial resolution by 4x in both directions, resulting in a spatial resolution of 8.8 km. This reduced resolution retains many benefits of high-resolution climate data—such as capturing the influence of local-scale topography on precipitation—while adhering to GPU memory constraints. To further accommodate these limitations, we restrict the spatial range of the dataset, focusing on a  $563.2 \text{ km} \times 563.2 \text{ km}$  region centred on Birmingham, UK. This region approximately corresponds to England and Wales. Figure 4.1 illustrates the area covered in our study. The significant variation in mean precipitation values across different regions suggests that we have retained much spatial structure in the preprocessed dataset influenced by topography and other local-scale factors.

In order to ensure that our neural network operates on consistently scaled inputs during the reverse-time generative process, starting from the multivariate standard Gaussian prior, we additionally scale each input data element to the range  $[-1, 1]$ .

### 4.1.3 Seasonally Stratified Train/Test Split

We adopted a stratified-by-season approach to devise an effective train/test split for our dataset. More specifically, we designated 80% of the data for training and 20% for testing, allocating every fifth season to the test set. This approach ensures that the test set encompasses a diverse range

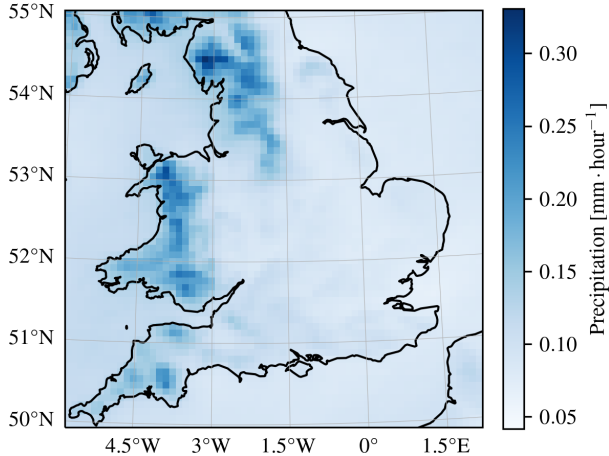


Figure 4.1: Mean precipitation rate for each  $8.8 \text{ km} \times 8.8 \text{ km}$  subarea in our dataset.

of samples—including an equal number of samples from each season and no two seasons from the same year—while preserving adequate independence between the train and test sets.

The rationale behind this stratification strategy stems from the dataset’s composition, which features hourly precipitation samples spanning 60 years. Given the substantial similarity between adjacent hourly samples in our dataset, a random split would be unsuitable. Such a split could result in many test samples originating from nearly identical temporal instances as those in the training set, thereby diminishing the independence of the train and test sets. By adopting a season stratification, we enhance the independence between the sets while ensuring a diverse range of samples.

We considered a stratified-by-year split but ultimately rejected it. A few notably wet or dry years could lead to a test set with a distribution that significantly deviates from the train set, resulting in biased model evaluation. The season-by-season stratification addresses this concern, achieving an equilibrium between minimising the inclusion of adjacent samples in both sets and guaranteeing significant variety over longer timeframes.

## 4.2 Importance of the Transformation

### 4.2.1 No Transformation

One of the primary contributions of this work is demonstrating that a transformation of the input data is critical to the model’s performance. Since no directly comparable results exist in the broader literature, we first establish a benchmark by providing results for our model trained without any transformation to the input data; we refer to this model as our *no-transformation model* for brevity.

Notably, the model produced samples with two significant, related issues. First and foremost, the generated samples all contain significant perceptible noise at the lower end of the precipitation scale; Figure 4.2a depicts an example of this. Additionally, many samples exhibit a baseline shift in precipitation rates; that is, samples generated by the model have a modal precipitation rate significantly higher than those observed in the test set. Most samples in the test set have a modal precipitation rate of approximately zero—indicating typically dry conditions. Conversely, many samples generated by our no-transformation model have a modal precipitation rate significantly higher, with little to no subareas below it. In practice, this indicates at least a trace quantity of precipitation across the entirety of the  $563.2 \text{ km} \times 563.2 \text{ km}$  region for the entire ten hours. Even in isolation, this would be an unnatural scenario and thus should certainly not occur at the frequency we observed. Figure 4.2b depicts a sample exhibiting this baseline shift.

## 4.2. IMPORTANCE OF THE TRANSFORMATION

---

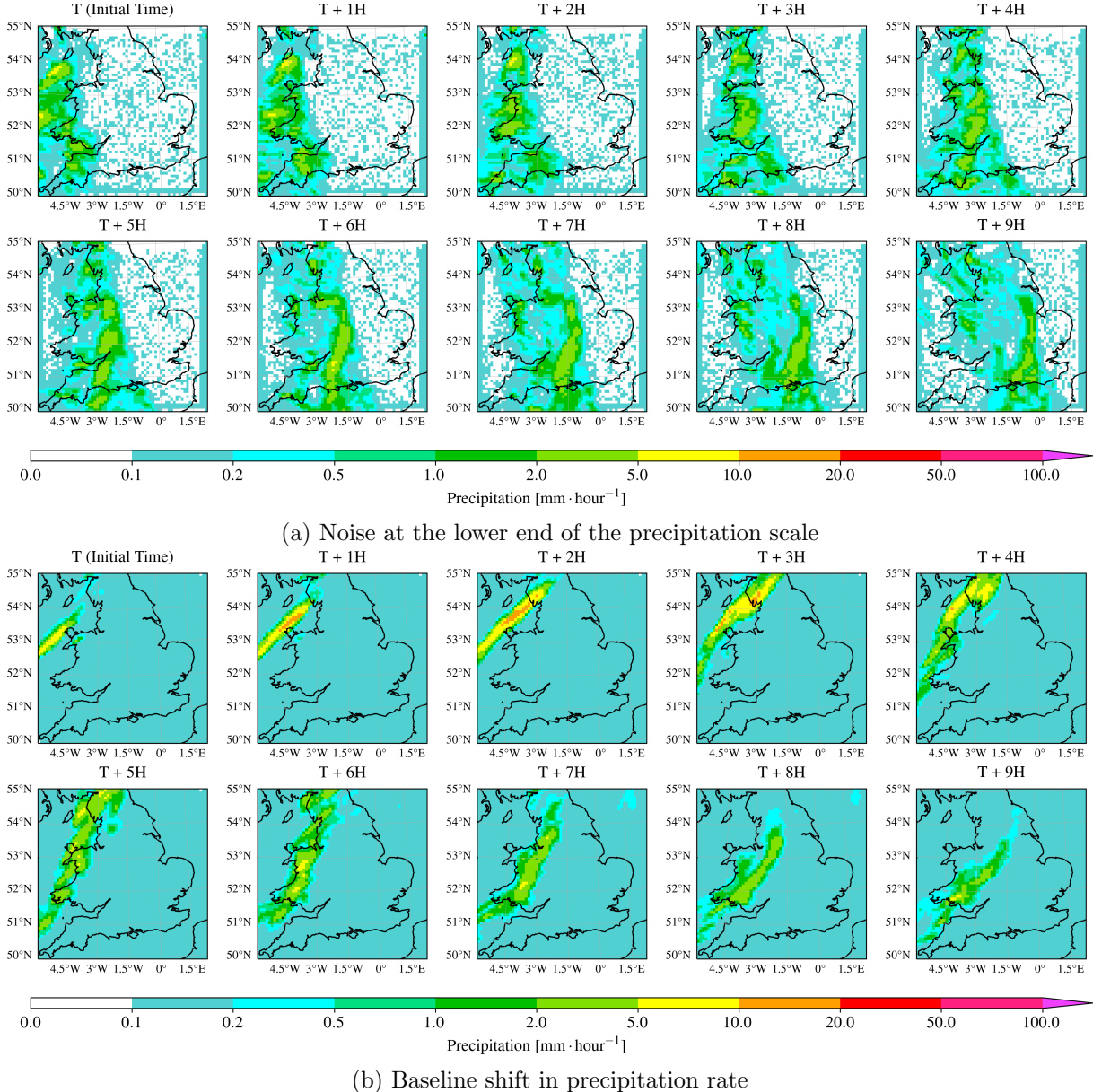


Figure 4.2: Two samples generated via our no-transformation model. The sample depicts hourly precipitation for the same  $563.2 \text{ km} \times 563.2 \text{ km}$  region centred on Birmingham, UK, over ten hours. Each grid cell illustrates the mean precipitation rate, measured in millimetres per hour, for an  $8.8 \text{ km} \times 8.8 \text{ km}$  subarea. The top sample exhibits significant noise at the lower end of the precipitation scale, while the bottom sample exhibits a baseline shift in precipitation rate.

## 4.2. IMPORTANCE OF THE TRANSFORMATION

To motivate these phenomena beyond individual examples, Figure 4.3a depicts the distribution of precipitation rates of our generated samples compared to those in our test set at the lower end of the scale (i.e. less than 0.3 millimetres per hour) where the noise is most perceptible. As can be seen, below approximately 0.2 millimetres per hour, the distribution of precipitation rates in our generated samples significantly deviates from that of the test set. While precipitation of this scale equates only to trace amounts, it is still non-negligible. Thus, using the generated samples in real-world contexts—such as hydrological studies—may present significant challenges.

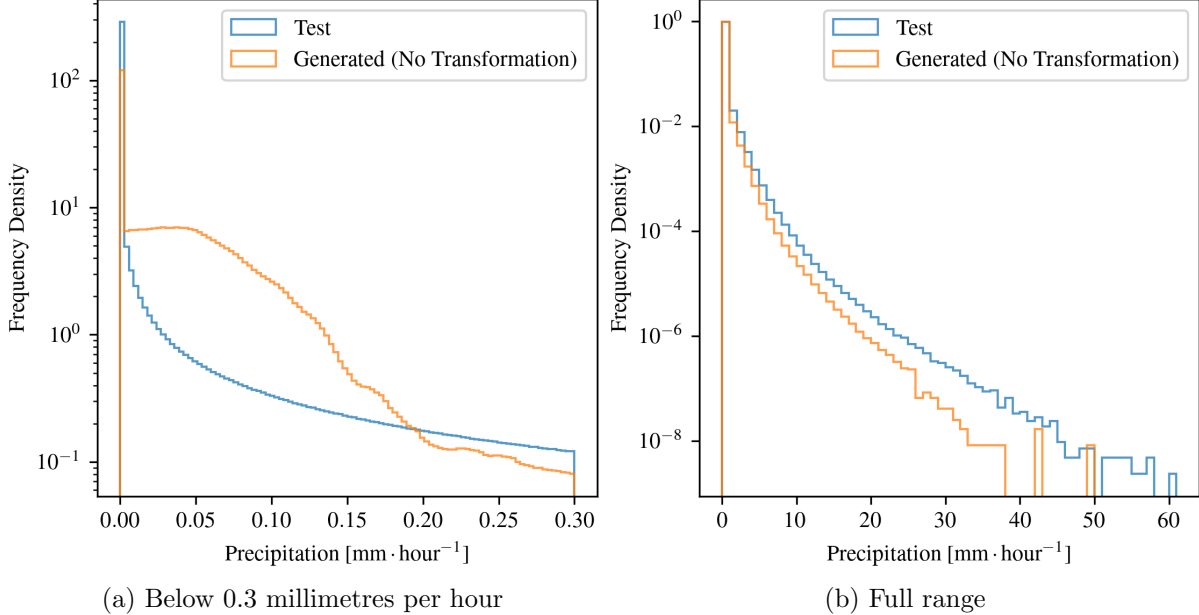


Figure 4.3: Distribution of individual precipitation intensities in samples generated via our no-transformation model and the test set. The horizontal axis is the precipitation rate, measured in millimetres per hour; the vertical axis is frequency density. The vertical axis is scaled logarithmically. The left graph depicts the distribution of precipitation rates below 0.3 millimetres per hour, while the right graph depicts the full distribution.

We can attribute this deviation to the two aforementioned issues but cannot pinpoint the underlying cause. We hypothesise that there are multiple contributory factors. Firstly, our score model  $\mathbf{s}_\theta(\mathbf{z}_t, \lambda_t)$  is not perfect; in other words, there will exist  $\mathbf{z}_t$  such that  $\mathbf{s}_\theta(\mathbf{z}_t, \lambda_t)$  does not serve as a good approximation for the true score  $\nabla_{\mathbf{z}_t} \log q(\mathbf{z}_t)$ . As such, by traversing the reverse-time SDE via the score model  $\mathbf{s}_\theta(\mathbf{z}_t, \lambda_t)$ , our reverse-time generative process will frequently not adjust the latent  $\mathbf{z}_t$  in the optimal direction to maximise the log-likelihood. Furthermore, since we can only approximate the reverse-time SDE, the discretised numerical solver introduces errors itself—this would be the case even if we had a perfect score model. We speculate that the errors introduced by these two contributory factors manifest as the noise at the lower end of the precipitation scale and the baseline shift in precipitation rate.

Noise of the observed magnitude creates unique challenges for diffusion models generating precipitation data—challenges that do not present as significant an issue in the more common domain of image generation. There are two primary reasons for this. First and foremost, the distribution of precipitation rates in our data is far more skewed than the distribution of colours in image data. This skew is evident in Figure 4.3b, which contains the full distribution of precipitation rates in our test set from UKCP18. 83% of the cells in the test set are of a precipitation rate lower than 0.01 millimetres per hour; to put this into perspective, the highest precipitation rate in our test set is approximately 60 millimetres per hour. As a direct result of this extreme distribution, even relatively small amounts of noise at the lower end of the scale

## 4.2. IMPORTANCE OF THE TRANSFORMATION

---

or minute inaccuracies in the reverse-time generative model can significantly impact the quality of the generated samples. The second challenge that generating precipitation data presents in contrast to image data is that precipitation is a continuous variable, in contrast to the discrete values that comprise each colour channel in an image. Thus, a final discretisation step at the end of the generative process for images eliminates much of the noise. We cannot take advantage of this approach for precipitation data. In the context of Figure 4.2a wherein the significant deviation from the true distribution is evident below the 0.2 millimetres per hour threshold, this constitutes approximately 0.2% of our output space. If this were an image with 256 discrete values per colour channel, this relative amount of the output space represents less than a single discrete value. Thus, a final discretisation step would eliminate the problem almost entirely.

Moving our attention beyond the lower extremity of the precipitation scale, Figure 4.3b illustrates the distribution of individual intensities within the samples generated by our model, contrasting them with those from the test set. The model demonstrates merit in capturing the overall shape of the true distribution. This similarity suggests that the model has a reasonable degree of success in learning the overall frequency of precipitation of varying intensity levels. However, it is evident that as we progress to more intense precipitation levels, the frequency discrepancy between the generated samples and the test set becomes more pronounced, suggesting a limitation in the model’s ability to generate extreme precipitation sufficiently frequently.

To gain a more detailed understanding of the model’s performance in a similar respect, we employ a quantile-quantile (QQ) plot, which offers a complementary perspective to the histogram by comparing the quantiles of the generated samples against the quantiles of the test set. QQ plots are particularly useful for detecting deviations in the distribution. From the QQ plot in Figure 4.4, it is evident that for a given intensity across most of the precipitation range, our model underestimates the frequency of all precipitation less than that intensity. There is typically a 25% discrepancy between the value of any given quantile in the test set and its corresponding quantile in the generated samples.

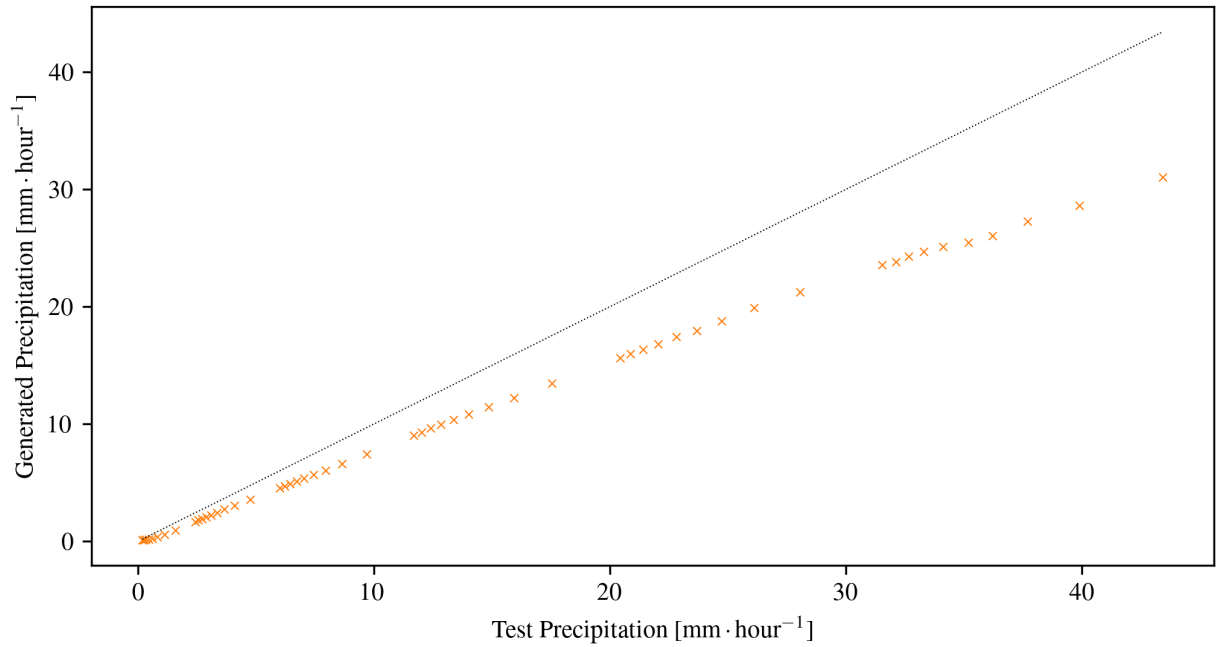


Figure 4.4: QQ plot comparing the distribution of individual precipitation intensities in samples generated via our no-transformation model with the test set. Quantiles plotted are  $\{1 - 10^{-n_1} + n_2 \cdot 10^{-n_1-1} \mid n_1, n_2 \in \mathbb{N}, 1 \leq n_1 \leq 6, 1 \leq n_2 \leq 9\}$ . The black line is the reference line, indicating where the quantiles of the generated samples would lie if they were equal to the quantiles of the test set.

## 4.2. IMPORTANCE OF THE TRANSFORMATION

---

Importantly, we observe a notable duality in the model’s shortcomings across the precipitation spectrum. Below approximately 0.2 millimetres per hour, the model introduces excessive noise, resulting in an overrepresentation of precipitation of this region in the generated samples. In contrast, the model underpredicts quantiles by about 25% at higher intensities. The quantiles only align where the overrepresented and underrepresented regions intersect. At this point, the adverse effects of the two issues cancel each other out. This dual issue underscores the challenges the model faces in accurately representing the true distribution of precipitation intensities, which could present potential problems in real-world applications.

Evaluating our model goes beyond analysing the distribution of individual cells’ values; it is essential to determine the extent to which our model has learnt the geographical structure of the true precipitation distribution across the UK. Ideally, our model must capture regional nuances influenced by topography and local climate patterns. For example, Wales experiences more precipitation on average than England, as the former is more mountainous. Accurate representation of this spatial structure is vital for reliable predictions and well-informed decision-making in agriculture, flood management and infrastructure development. To evaluate the effectiveness of our model in capturing the correct amount of precipitation in different subareas, we employ mean-normalised bias plots as an assessment tool. We calculate mean-normalised bias by subtracting the target mean from the sample mean and dividing the result by the target mean. Figure 4.5 depicts the mean-normalised bias for each  $8.8 \text{ km} \times 8.8 \text{ km}$  subarea. There is a weak negative correlation between mean precipitation and mean-normalised bias with a coefficient of determination of 0.31—the samples generated via the model typically have lower precipitation in areas with higher mean precipitation in the test set. Figure 4.1 shows that Wales, North West England and South West England broadly have the highest mean precipitation; these regions directly correspond to the regions with the lowest mean-normalised bias in Figure 4.5.

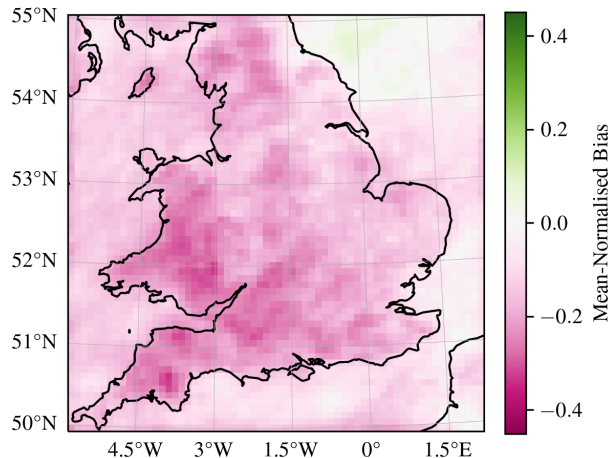


Figure 4.5: Mean-normalised bias at each cell representing the same  $8.8 \text{ km} \times 8.8 \text{ km}$  geographical area in the samples generated via our no-transformation model.

We must also assess how successfully our model has learnt the true distribution’s underlying spatial and temporal structure. This analysis is crucial: theoretically, we could trivially train a model to generate pure noise whereby the distribution of individual cells’ values perfectly matches that of the test set for each  $8.8 \text{ km} \times 8.8 \text{ km}$  subarea. While an extreme example, this motivates the necessity of ensuring our generated samples also capture the structure and characteristics of the true distribution. To assess the degree to which this is the case, we employ power spectral density (PSD) graphs, which depict a signal’s power distribution. In general terms, a PSD graph provides information on the distribution of frequencies present in a signal. In this work, we employ two different PSD graphs: spatial PSD graphs for individual one-hour snapshots of the entire  $563.2 \text{ km} \times 563.2 \text{ km}$  region; and temporal PSD graphs for multiple

## 4.2. IMPORTANCE OF THE TRANSFORMATION

consecutive one-hour snapshots of a single  $8.8 \text{ km} \times 8.8 \text{ km}$  subarea. Our interpretation of a PSD graph depends on the nature of the signal. For spatial PSD graphs, greater power at higher spatial frequencies reveals sharp boundaries between areas with and without precipitation, likely indicating the presence of localised showers. On the other hand, greater power at lower spatial frequencies points to smooth variations in precipitation intensity, suggesting a sizeable frontal system. For temporal PSD graphs, greater power at higher temporal frequencies reveals rapid fluctuations in precipitation, indicating the presence of briefer precipitation events such as convective showers. Conversely, greater power at lower temporal frequencies suggests stabler events—potentially a continuous dry spell.

From Figure 4.6, it is evident that the samples in the test set contain more power at both lower spatial and temporal frequencies than at higher temporal and spatial frequencies, on average. The samples generated via our no-transformation model follow a similar trend in both cases, as indicated by the similar shapes of the PSD graphs. We can interpret this as the model having broadly learnt the true distribution’s underlying spatial and temporal structure. In other words, the model has broadly learnt the relative frequency of precipitation events at different spatial and temporal scales, from short localised showers to long-lasting frontal systems. However, the samples generated via our model contain less power than those in the test set at all scales.

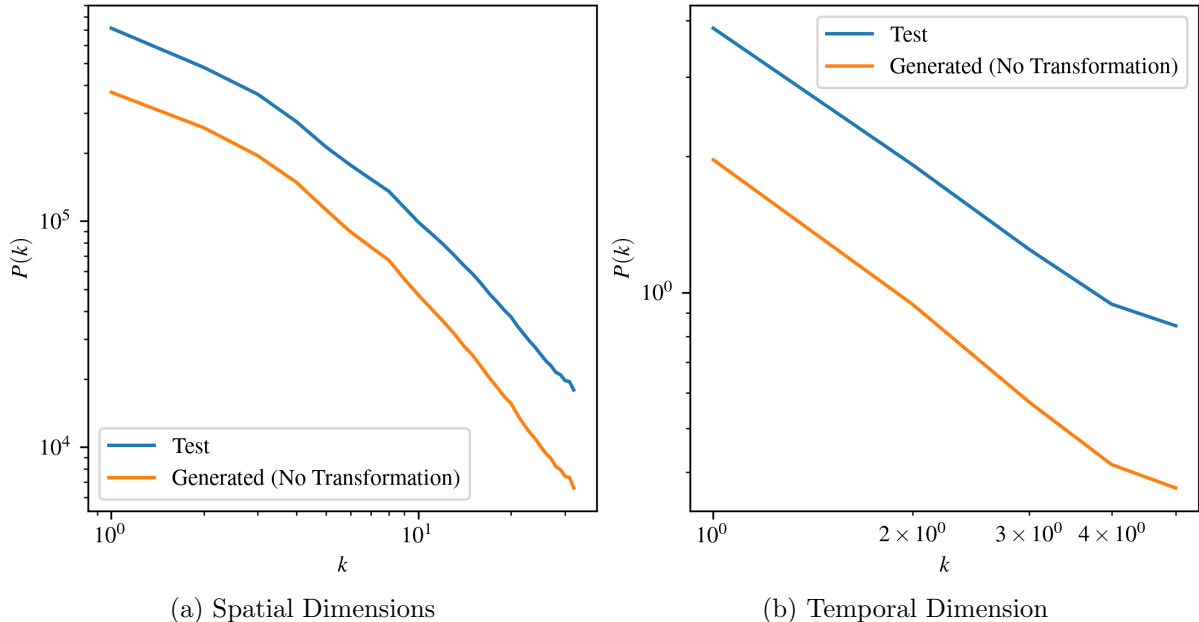


Figure 4.6: Power spectral density (PSD) graphs for samples generated via our no-transformation model and the test set. The horizontal axis is the number of waves, denoted  $k$ ; the vertical axis is the mean power across all samples for a given  $k$ , denoted  $P(k)$ . Both axes are logarithmic. The left graph is for the two spatial dimensions, and the right graph is for the temporal dimension.

### 4.2.2 Square-Root Transformation

In the previous section, we introduced baseline results for our model trained without any transformation applied to the input data. In this section, we build upon this foundation by presenting results for a model employing a square-root transformation to the input, which we henceforth refer to as our *square-root-transformation model* for brevity. The results showcased herein provide compelling evidence that implementing a suitable transformation can significantly enhance the performance of a diffusion model.

Foremost, applying the square-root transformation to the input data effectively addressed

## 4.2. IMPORTANCE OF THE TRANSFORMATION

the two primary concerns observed in the samples generated by our no-transformation model. Specifically, it eliminated the discernible noise at the lower end of the precipitation scale and averted the unnatural baseline shift in precipitation rates. The improvement is clearly illustrated in Figure 4.7a. Notably, the deviation from the test distribution shape below 0.2 millimetres per hour—observed in our no-transformation model—is absent in samples generated by our square-root-transformation model, exemplifying the effectiveness of incorporating an appropriate transformation during the model training process.

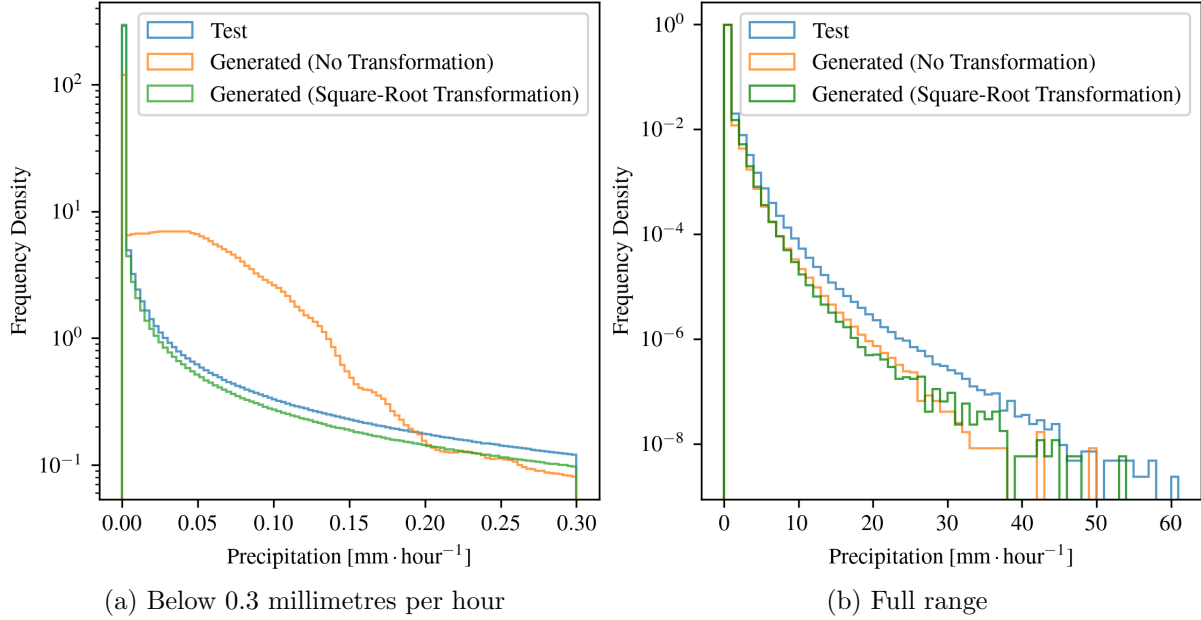


Figure 4.7: Distribution of individual precipitation intensities in samples generated via our square-root-transformation model, samples generated via our no-transformation model and the test set. The format of each graph is the same as Figure 4.3

We hypothesise that the improvement is due to the transformation allocating a more significant portion of the output space  $[-1, 1]$  to the lower end of the precipitation scale. Without transformation, the input data is scaled linearly to the range  $[-1, 1]$ , resulting in the region below 0.2 millimetres per hour occupying only about 0.2% of the output space. In contrast, the square-root transformation involves computing the square root of each input data element before applying the same linear scaling; consequently, the region below 0.2 millimetres per hour occupies approximately 5% of the output space, representing a 20-fold increase. We cannot conclusively determine why allocating a more significant portion of the output space to the same region resolves the aforementioned issues. We recommend this as an investigation for future work.

Applying the square-root transformation not only addresses the two previously mentioned issues but also enhances the overall quality of our samples by most measures. As evident in Figure 4.7b, up to approximately 12 millimetres per hour, the frequency of precipitation intensity in 1 millimetre per hour intervals more closely aligns with the test set’s distribution compared to samples generated via our no-transformation model. We observe from the QQ plot in Figure 4.8 that this represents approximately 99.99% of all precipitation intensities in the test set. Beyond this range—encompassing the most intense 0.01% of precipitation—the dominance of either model is less discernible.

Figure 4.9 depicts the mean-normalised bias for each  $8.8 \text{ km} \times 8.8 \text{ km}$  subarea in samples generated via our square-root-transformation model. Compared to the mean-normalised bias for our no-transformation model, given in Figure 4.5, the bias is worse for most subareas. However,

## 4.2. IMPORTANCE OF THE TRANSFORMATION

---

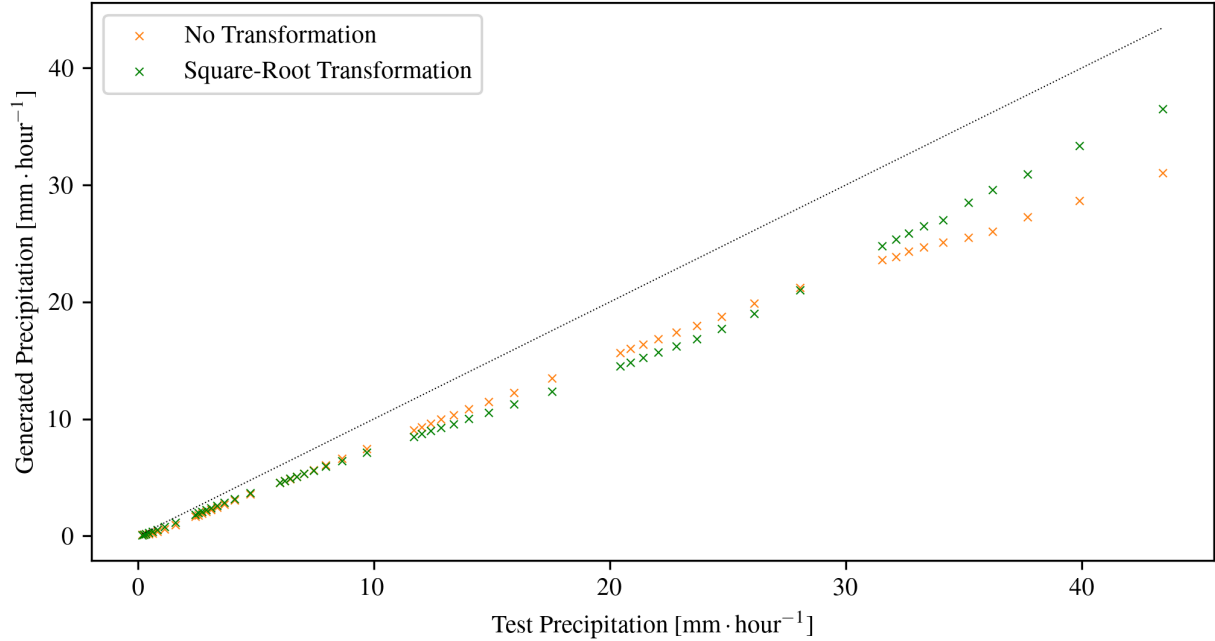


Figure 4.8: QQ plot comparing the distribution of individual cells' values in samples generated by our square-root transformed model to samples generated by our untransformed model and the UKCP18 test set. The format is the same as Figure 4.4.

we argue that the relatively good mean-normalised bias of the no-transformation model is an artefact resulting from the two aforementioned issues at the lower end of the precipitation spectrum. These issues contribute to a reduced probability of the model generating precipitation rates of approximately zero, consequently inducing an artificial increase in the mean precipitation rate. As such, we argue that the relatively severe bias in our square-root-transformation model does not represent an actual regression in performance. Notably, when employing the square-root transformation, we observe no correlation with our no-transformation model in the mean-normalised bias across different subareas, indicating that the choice of transformation can influence the spatial distribution of the bias. Unlike our no-transformation model, our square-root-transformation model exhibits severe mean-normalised bias across Central England, East of England, London, and South East England.

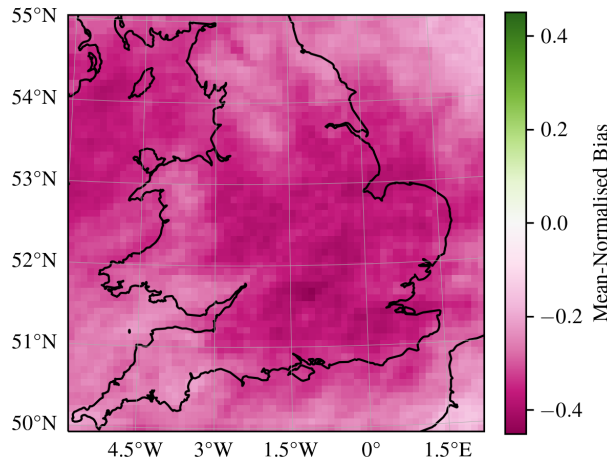


Figure 4.9: Mean-normalised bias at each cell representing the same  $8.8 \text{ km} \times 8.8 \text{ km}$  geographical area in the samples generated by our square-root-transformation model.

Moving beyond the intensity of individual cells, we found that the square-root transformation

benefited the power in our samples. More specifically, the average power over the spatial and temporal dimensions more closely aligns with the test set in samples generated via the square-root-transformation model. The improvement is observable over all scales, as demonstrated by the spatial and temporal PSD graphs in Figure 4.10. The consistent enhancement suggests that the square-root transformation facilitates the model’s ability to learn and represent the spatial and temporal features inherent in the true precipitation distribution with better proficiency.

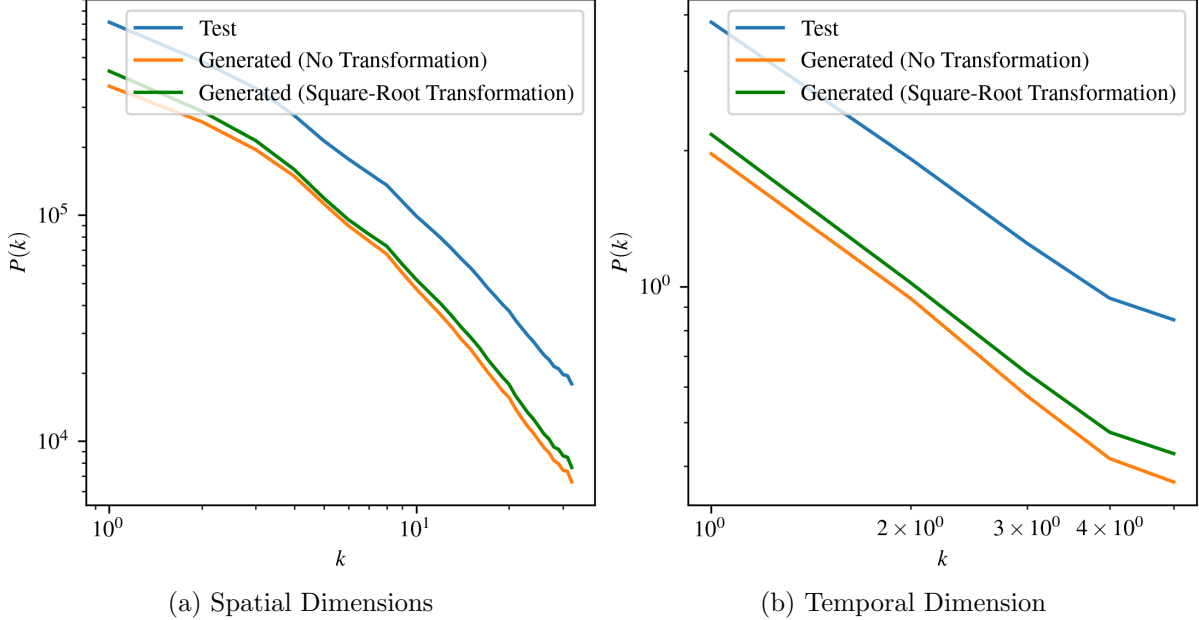


Figure 4.10: PSD graphs for samples generated via our square-root transformed model, samples generated via our untransformed model, and the test set from UKCP18. The format is the same as Figure 4.6.

## 4.3 Learning a Transformation

In this section, we build upon the significant improvements achieved with the square-root transformation; we introduce an approach that enables our model to learn a transformation rather than depending on a predefined function. By facilitating the adaptive discovery of a suitable transformation, we posit that this approach may hold the potential for generalisation with different distributions, not limited to precipitation. This adaptability could prove particularly valuable for distributions lacking an easily identifiable transformation to enhance performance, thus offering a flexible solution to enhance the performance of diffusion models across various applications.

### 4.3.1 Change of Variable Rule

Suppose we transform our observed variable  $\mathbf{x}$  via an element-wise vector-valued function  $\mathbf{h} : [-1, 1]^D \rightarrow [-1, 1]^D$ , such that:

$$\mathbf{h}(\mathbf{x}) = \begin{bmatrix} h(x_1) \\ h(x_2) \\ \vdots \\ h(x_D) \end{bmatrix} \quad (4.1)$$

$x_i$  is the  $i$ -th element of  $\mathbf{x}$ , and  $h : [-1, 1] \rightarrow [-1, 1]$  is a scalar-valued monotonically increasing function applied to each element of  $\mathbf{x}$ . The change of variable rule states that:

$$p_\theta(\mathbf{x}) = \tilde{p}_\theta(\mathbf{h}(\mathbf{x})) \left| \det \left( \frac{d\mathbf{h}(\mathbf{x})}{d\mathbf{x}} \right) \right| \quad (4.2)$$

where  $\tilde{p}_\theta(\mathbf{h}(\mathbf{x}))$  is the probability density of our transformed observed variable  $\mathbf{h}(\mathbf{x})$ ,  $\det$  is the determinant operator, and  $d\mathbf{h}(\mathbf{x})/d\mathbf{x}$  is the Jacobian of transformation  $\mathbf{h}$ . Since  $\mathbf{h}$  is an element-wise transformation, the Jacobian matrix is diagonal:

$$\frac{d\mathbf{h}(\mathbf{x})}{d\mathbf{x}} = \begin{bmatrix} \frac{\partial \tilde{x}_1}{\partial x_1} & 0 & \cdots & 0 \\ 0 & \frac{\partial \tilde{x}_2}{\partial x_2} & \cdots & 0 \\ \vdots & \vdots & \ddots & \vdots \\ 0 & 0 & \cdots & \frac{\partial \tilde{x}_D}{\partial x_D} \end{bmatrix} \quad (4.3)$$

The determinant of a diagonal matrix is simply the product of its diagonal elements; thus, we can write:

$$\det \left( \frac{d\mathbf{h}(\mathbf{x})}{d\mathbf{x}} \right) = \prod_{i=1}^D \frac{\partial h(x_i)}{\partial x_i}. \quad (4.4)$$

Therefore, we can rewrite the change of variables rule under transformation  $\mathbf{h}$  in the following simplified form:

$$p_\theta(\mathbf{x}) = \tilde{p}_\theta(\mathbf{h}(\mathbf{x})) \prod_{i=1}^D \frac{\partial h(x_i)}{\partial x_i} \quad (4.5)$$

We can thus formulate the negative log-likelihood of  $\mathbf{x}$  as follows:

$$-\log p_\theta(\mathbf{x}) = -\log \left( \tilde{p}_\theta(\mathbf{h}(\mathbf{x})) \prod_{i=1}^D \frac{\partial h(x_i)}{\partial x_i} \right) \quad (4.6)$$

$$= -\log \tilde{p}_\theta(\mathbf{h}(\mathbf{x})) - \log \left( \prod_{i=1}^D \frac{\partial h(x_i)}{\partial x_i} \right) \quad (4.7)$$

$$= -\log \tilde{p}_\theta(\mathbf{h}(\mathbf{x})) - \sum_{i=1}^D \log \left( \frac{\partial h(x_i)}{\partial x_i} \right) \quad (4.8)$$

### 4.3.2 ELBO Loss with a Change of Variable

The ELBO loss for a transformed datapoint  $\mathbf{h}(\mathbf{x})$ , denoted  $\tilde{\mathcal{L}}_{\text{ELBO}}(\mathbf{h}(\mathbf{x}))$ , serves as a variational bound on the negative log-likelihood of  $\mathbf{h}(\mathbf{x})$  and is given by:

$$-\log \tilde{p}_\theta(\mathbf{h}(\mathbf{x})) \leq \tilde{\mathcal{L}}_{\text{ELBO}}(\mathbf{h}(\mathbf{x})) = \mathbb{E}_{\mathbf{z}_0, \dots, \mathbf{z}_1 \sim \tilde{q}(\mathbf{z}_0, \dots, \mathbf{z}_1 | \mathbf{h}(\mathbf{x}))} \left[ \log \frac{\tilde{p}_\theta(\mathbf{z}_0, \dots, \mathbf{z}_1, \mathbf{h}(\mathbf{x}))}{\tilde{q}(\mathbf{z}_0, \dots, \mathbf{z}_1 | \mathbf{h}(\mathbf{x}))} \right] \quad (4.9)$$

Plugging the inequality into Equation 4.8, we obtain:

$$-\log p_\theta(\mathbf{x}) \leq \tilde{\mathcal{L}}_{\text{ELBO}}(\mathbf{h}(\mathbf{x})) - \sum_{i=1}^D \log \left( \frac{\partial h(x_i)}{\partial x_i} \right) \quad (4.10)$$

Thus, if we were to parameterise the transformation  $\mathbf{h}_\omega$ , with transformative parameters  $\omega$ , we would theoretically be able to learn some optimal transformation that enables us to approximately minimise the negative log-likelihood of the observed variable  $\mathbf{x}$ . For completeness, the

loss with transformative parameters  $\omega$  yields only a minor modification to Equation 4.10 and is given by:

$$p_\theta(\mathbf{x}) \leq \tilde{\mathcal{L}}_{\text{ELBO}}(\mathbf{h}_\omega(\mathbf{x})) - \sum_{i=1}^D \log \left( \frac{\partial h_\omega(x_i)}{\partial x_i} \right) \quad (4.11)$$

However, as detailed in Section 2.7.6, optimising our generative parameters  $\theta$  via the ELBO loss yields suboptimal results. Diffusion models in the broader literature have achieved far superior results via optimisation with the weighted loss  $\mathcal{L}_{\text{WL}}$ .

### 4.3.3 Weighted Loss with a Change of Variable

The  $\lambda$ -dependent weighting function  $w(\lambda)$  in the weighted loss  $\mathcal{L}_{\text{WL}}$  causes it to lose a direct theoretical relationship with the negative log-likelihood of the observed variable  $\mathbf{x}$ . Thus, we cannot directly apply the change of variable approach to the weighted loss as we did for the ELBO loss. However, we can consider the individual contribution of the negative log-determinant term in the loss given in Equation 4.11 to derive an empirically good loss function for our diffusion model that jointly optimises the generative parameters  $\theta$  and the transformative parameters  $\omega$ . Importantly, since we constrain the output range of  $h_\omega$  to be  $[-1, 1]$ , the neural network cannot infinitely extend the output range. As such, it has to learn some optimal monotonically increasing function to minimise:

$$-\sum_{i=1}^D \log \left( \frac{\partial h_\omega(x_i)}{\partial x_i} \right) \quad (4.12)$$

Intuitively, since the log function itself is monotonically increasing, the negative log-determinant term will encourage a steeper gradient for areas of the input space  $[-1, 1]$  wherein individual elements  $x_i$  occur most often. Conversely, the term will individually encourage a shallower gradient for areas of the input space  $[-1, 1]$  wherein individual elements  $x_i$  occur least often. Using this intuition, we hypothesised that we could add the negative log-determinant term to the weighted loss to jointly optimise the generative parameters  $\theta$  and the transformative parameters  $\omega$  to achieve higher-quality samples. We denote the weighted loss for a transformed datapoint  $\mathbf{h}_\omega(\mathbf{x})$  by  $\tilde{\mathcal{L}}_{\text{WL}}(\mathbf{h}_\omega(\mathbf{x}))$ , and thus our new loss function is given by:

$$\tilde{\mathcal{L}}_{\text{WL}}(\mathbf{h}_\omega(\mathbf{x})) - \sum_{i=1}^D \log \left( \frac{\partial h_\omega(x_i)}{\partial x_i} \right) \quad (4.13)$$

### 4.3.4 Transformation Neural Network

We utilise a simple neural network with two fully-connected hidden layers to learn the transformation  $h_\omega$  from Equation 4.13. The network contains only a single neuron in both the input and output layers and 16 neurons in each hidden layer; we use the tanh activation function for each neuron in both hidden layers and for the output neuron. We restrict all the weights—not including biases—to be positive to ensure the learnt transformation is monotonically increasing. Since the logarithm of zero is undefined, we add a small multiple of the input to the network’s output to prevent the gradient from being zero at any point. We scale the output to the range  $[-1, 1]$ .

### 4.3.5 Improved Weighted Loss with a Change of Variable

We found that, in practice, the weighted loss with a change of variable given in Equation 4.13 gave rise to poor-quality samples. The transformation it induced was too aggressive, with a significantly large gradient at the lowest end of the input space around  $x_i = -1$ . Consequently,

### 4.3. LEARNING A TRANSFORMATION

except for that region, the learnt transformation was  $h_\omega(x_i) \approx 1$ . As such, the loss function gave rise to the effect depicted in Figure 4.11. Constraining much of the input space to  $h_\omega(x_i) \approx 1$  prevents the model from learning the distribution of the transformed observed variable  $\mathbf{h}_\omega(\mathbf{x})$  correctly. As such, the samples contain unnaturally high precipitation rates: many areas depicted in Figure 4.11 receive over half a metre of precipitation over the ten hours.

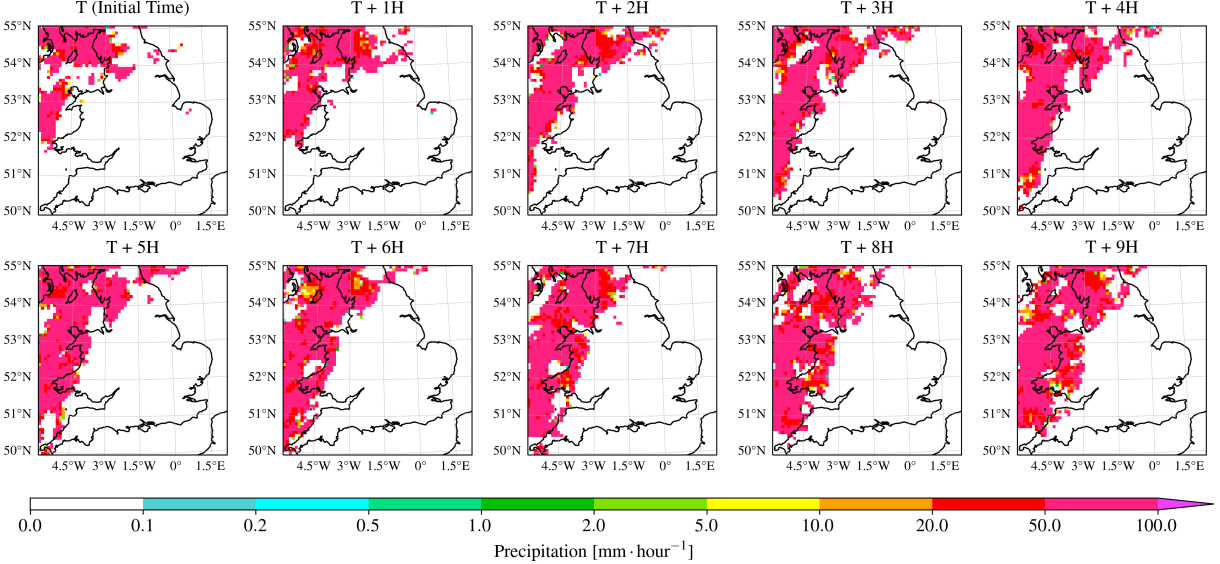


Figure 4.11: Randomly selected sample generated via our model trained with the loss function given in Equation 4.13. The format is the same as Figure 4.2a.

To address this issue, we introduce two interventions which, in conjunction, we found to yield a significant improvement in the quality of the samples generated by our model. Firstly, we significantly increase the multiple by which we add the input to the transformation network to its output. Consequently, at no point is the gradient of the transformation less than a predetermined value. We thus refer to this small multiple as our *minimum gradient coefficient*. Empirically, we found a minimum gradient coefficient of 0.1 yielded good results.

Secondly, we introduce a *masking function*, denoted  $m : [-1, 1] \rightarrow \{0, 1\}$ , that takes a single element  $x_i$  of some datapoint  $\mathbf{x}$  as input and outputs a binary value:

$$m(x_i) = \begin{cases} 1 & \text{if } x_i \in \mathcal{M} \\ 0 & \text{otherwise} \end{cases} \quad (4.14)$$

where  $\mathcal{M} \subseteq [-1, 1]$  is a pre-defined masking set with no learnable parameters, which we use to assert greater control over the transformation learnt by our transformation neural network. We incorporate the masking function into our loss given in Equation 4.13 to yield:

$$\tilde{\mathcal{L}}_{WL}(\mathbf{h}_\omega(\mathbf{x})) - \sum_{i=1}^D \log \left( \frac{\partial h_\omega(x_i)}{\partial x_i} \right) \cdot m(x_i) \quad (4.15)$$

As such, we can use the masking function and masking set to influence the gradient of the learnt transformation. Only elements  $x_i$  within the masking set  $\mathcal{M}$  will contribute to the negative log-determinant term in the loss. On one end of the scale, if we were to set  $\mathcal{M} = [-1, 1]$ , this would equate to the loss of Equation 4.13. Conversely, if we were to set  $\mathcal{M} = \emptyset$ , then the log-determinant term would be redundant—it would never contribute to the loss. Empirically, we found  $\mathcal{M} = [-0.99975, 1]$  prevented the transformation network from learning too extreme a transformation. In simple terms, we prevent the elements of our training set that are extremely small—to the extent that they can almost be considered ‘dry’ for all practical intents and

purposes—contributing to the transformation. Figure 4.12 shows the transformation learnt by our model trained with the loss function given in Equation 4.15. We refer to this model as our *learnt-transformation model* for brevity.

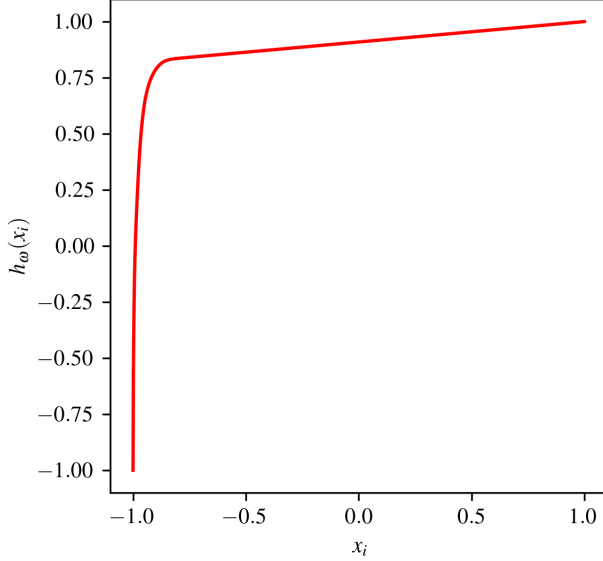


Figure 4.12: The transformation learnt by our model trained with the loss function given in Equation 4.15. The horizontal axis is the value of some element  $x_i \in [-1, 1]$  input to the transformation network; the vertical axis is the corresponding output  $h_\omega(x_i) \in [-1, 1]$ .

Importantly, for both of these solutions, we did not conduct any systematic hyperparameter search; thus, it is likely that more optimal combinations of the minimum gradient coefficient and masking set exist.

#### 4.3.6 Evaluation of the Learnt Transformation

To evaluate the performance of our model with the learnt transformation, we primarily focus our analysis against benchmarks set by the square-root-transformation model since it outperformed our no-transformation model by most measures.

Notably, samples generated via our learnt-transformation model better capture the true frequency of individual precipitation intensities for most rates observed in the test set, as evident from Figure 4.13. In particular, our learnt-transformation model outperforms our square-root-transformation model in every one-millimetre-per-hour interval up to six millimetres-per-hour. Due to the skewed distribution of precipitation, this represents all but the 0.01% most intense precipitation, as evident from the QQ plot in Figure 4.14. Beyond this region, our learnt-transformation model similarly excels at capturing precipitation with intensities of 10–26 millimetres per hour, with a 15% absolute reduction on average in the relative discrepancy in frequency compared to our square-root-transformation model. In all other regions, the dominance of either model is less clear.

Figure 4.15 depicts the mean-normalised bias at each  $8.8 \text{ km} \times 8.8 \text{ km}$  subarea in samples generated via our learnt-transformation model. We observe a remarkable improvement in the mean-normalised bias in almost all subareas compared to that of the square-root transformation model in Figure 4.9. We attribute this improvement to the decreased overrepresentation of precipitation below one millimetre per hour, which account for approximately 97% of all intensities in our test set. As a direct result, our learnt-transformation model equally lessens the underrepresentation of more intense precipitation. Thus, the mean precipitation intensity in the generated samples is significantly higher in almost all subareas.

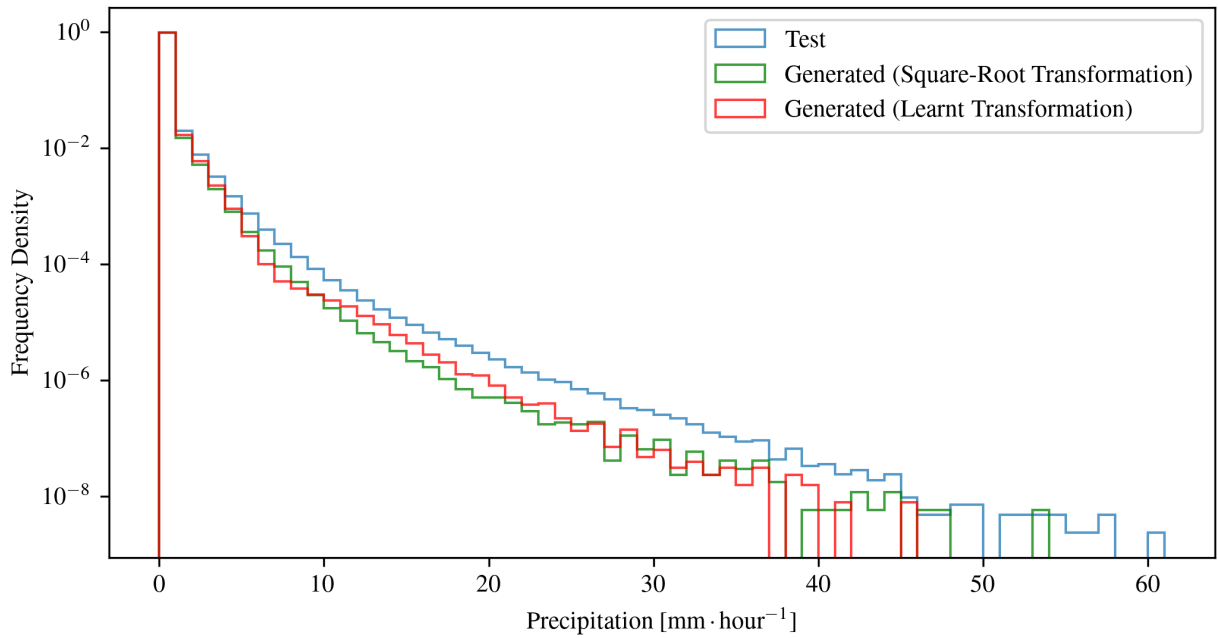


Figure 4.13: Distribution of precipitation rates in samples generated via our learnt-transformation model compared to samples generated via our square-root-transformation model and the test set from UKCP18. The format is the same as Figure 4.3.

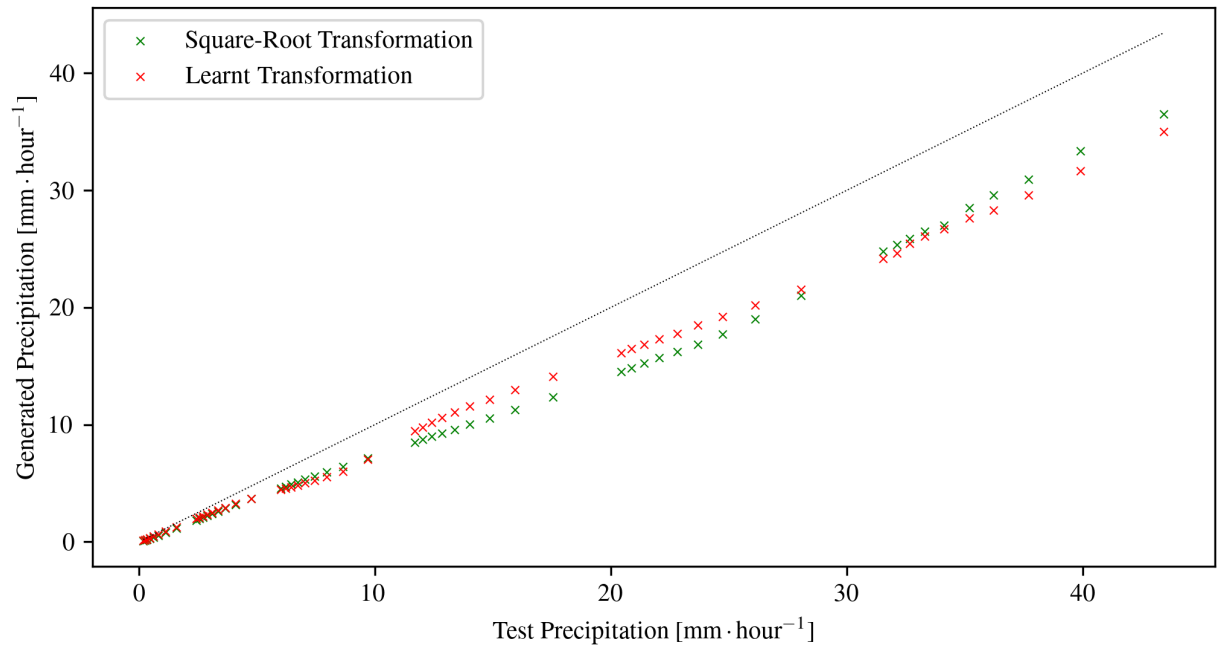


Figure 4.14: QQ plots for individual cells within the test set from UKCP18 against both samples generated via our square-root-transformation model and samples generated via our learnt-transformation model. The format is the same as Figure 4.4.  $\mathcal{Q} = \{1 - 10^{-n_1} + n_2 \cdot 10^{-n_1-1} \mid n_1, n_2 \in \mathbb{N}, 1 \leq n_2 \leq 9\}$ .

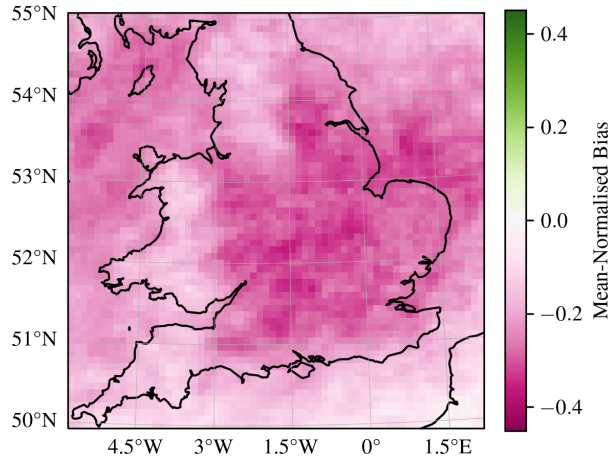


Figure 4.15: Mean-normalised bias at each cell representing the same  $8.8 \text{ km} \times 8.8 \text{ km}$  geographical area in the samples generated via our learnt-transformation model.

Interestingly, we observe a notable positive linear association—characterised by a coefficient of determination of 0.59—between the mean-normalised bias of a given subarea in samples generated via our no-transformation model and those generated via our square-root transformation model, as evident from the scatter plot in Figure 4.16. Similar to our square-root-transformation model, our learnt-transformation model exhibits particularly pronounced bias in Central England, East of England, London and South East England. This association stands in contrast to the absence of any discernible relationship between the mean-normalised bias of a given sub-area in samples generated via our square-root-transformation model and those generated via our learnt-transformation model. The contrasting associations potentially warrant further exploration in future work to gain a deeper understanding of the underlying causes and potential implications of different transformation techniques on model performance.

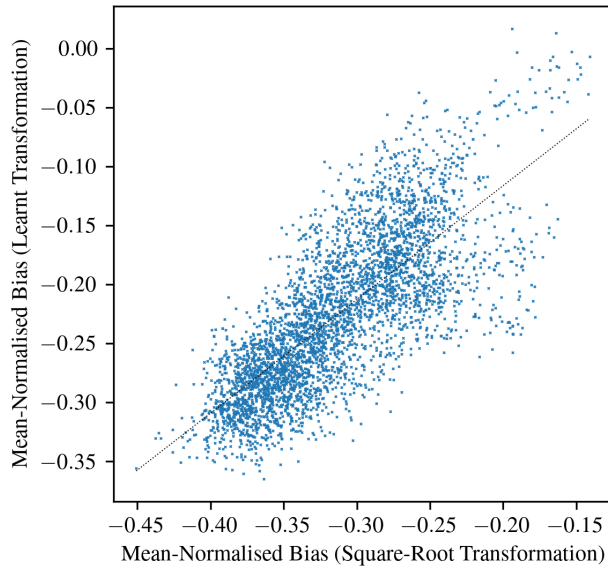


Figure 4.16: Relationship between the mean-normalised bias at each cell representing the same  $8.8 \text{ km} \times 8.8 \text{ km}$  geographical area in the samples generated via our square-root-transformation model and our learnt-transformation model. The horizontal axis is the mean-normalised bias for the square-root transformation; the vertical axis is the mean-normalised bias for the learnt transformation. The black line shows linear regression with a coefficient of determination of  $R^2 = 0.59$ .

Although the dominance of our learnt-transformation model is not absolute regarding capturing the distribution of individual precipitation intensities, our study demonstrates that it consistently outperforms in terms of the power in its generated samples. At any given temporal or spatial resolution, the power in samples produced via our learnt-transformation model is closer to the power in our test set from UKCP18 than those produced via our square-root-transformation model, as evident in Figure 4.17. The power at each scale is, on average, 50% lower in samples generated via the square-root transformation model in both the spatial and temporal dimensions. For our learnt-transformation model, the discrepancy reduces to 45%, an absolute reduction of 5%. These improvements suggest that enabling the model to learn its transformation empowers it to learn precipitation’s spatial and temporal characteristics more effectively.

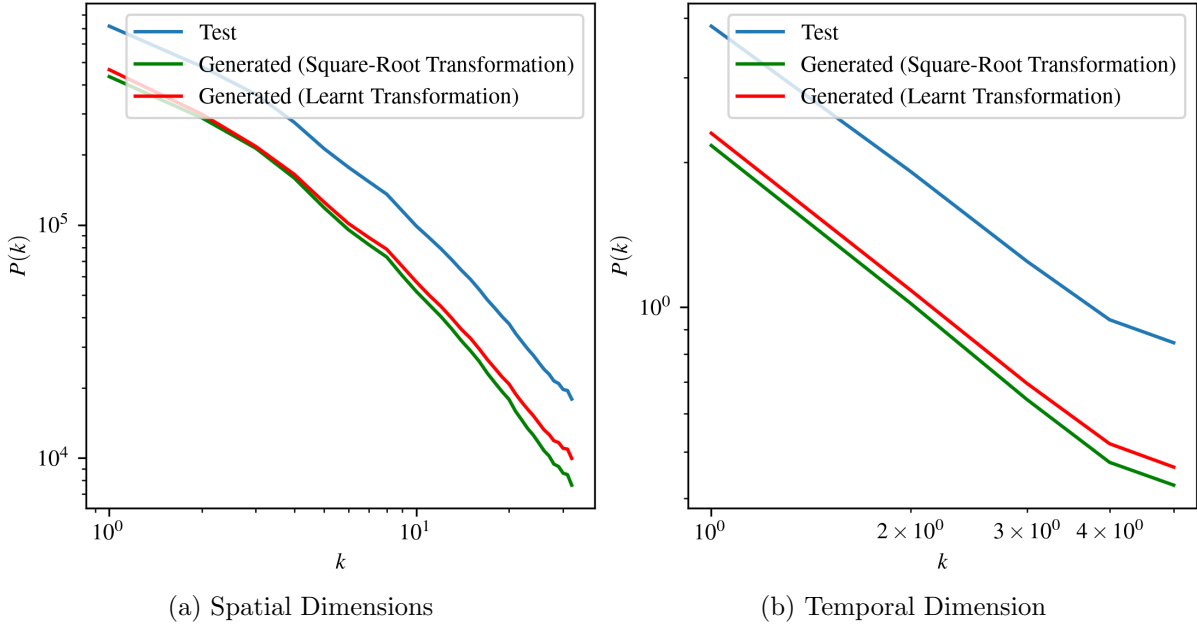


Figure 4.17: PSD graphs for samples generated via our learnt-transformation model, our square-root-transformation model and the test set from UKCP18. The format is the same as Figure 4.6.

Our analysis demonstrates that our learnt-transformation model consistently outperforms the square-root-transformation model in several key aspects. These aspects include capturing the true frequency of individual precipitation rates for most intensities, reducing the mean-normalised bias in generated samples, and offering better power across the spatial and temporal domains at all scales. We attribute the improved performance to the ability of the learnt-transformation model to learn a suitable transformation for the given data. Moreover, the adaptability of our approach holds potential for generalisation to different distributions—not limited to precipitation—thus offering a flexible and powerful solution for enhancing the performance of diffusion models across various potential applications. Although the dominance of our learnt-transformation model is not absolute, we believe the overall improvements warrant further exploration and refinement in future work.

## 4.4 Temporal Interpolation

In Section 2.7.8, we detailed reconstruction-guided sampling [15] as a technique for deriving a conditional diffusion model approximately from an unconditional model. In this section, we employ this method to facilitate *temporal interpolation*: the generation of intermediate samples

#### 4.4. TEMPORAL INTERPOLATION

---

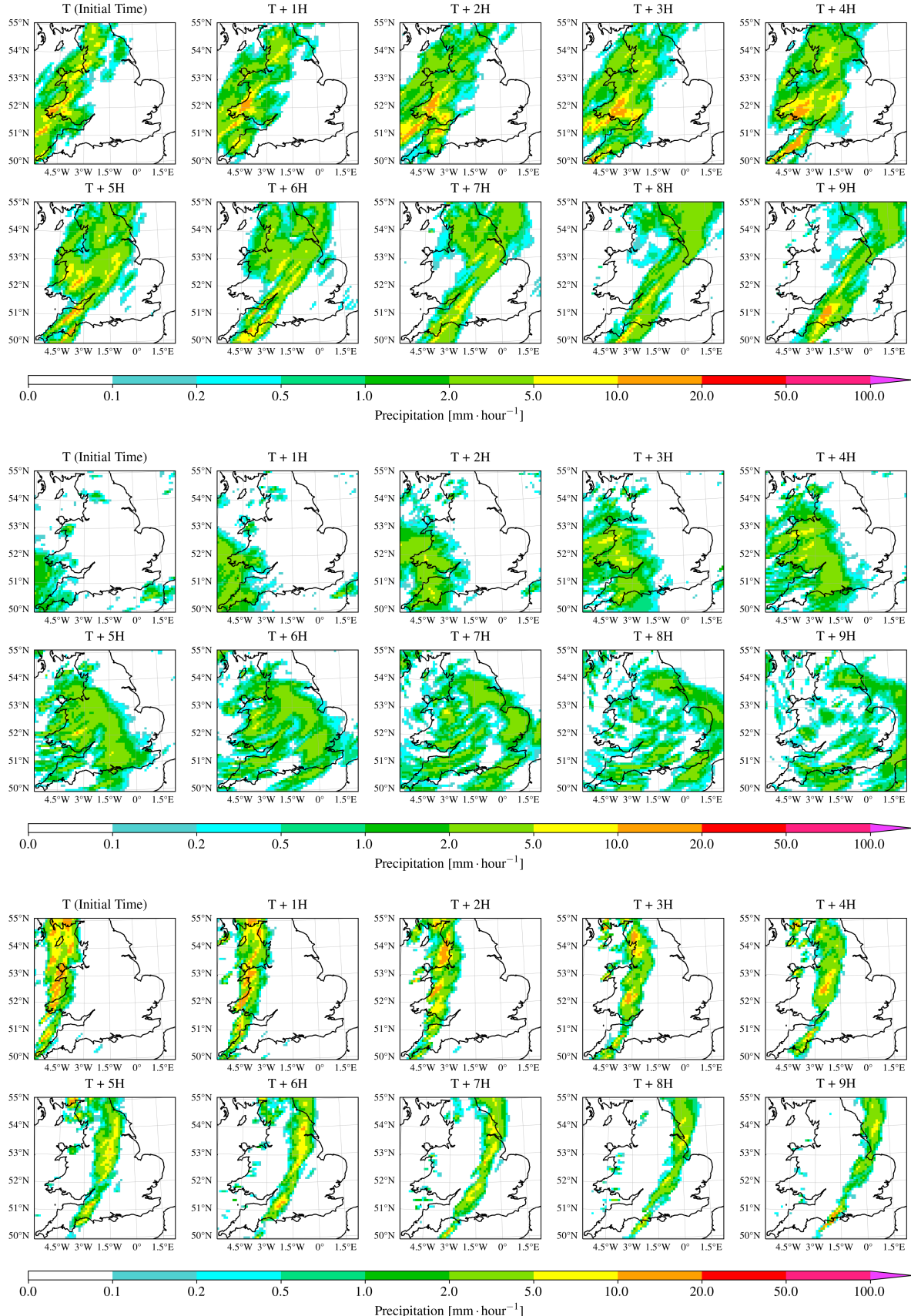


Figure 4.18: Three samples generated via our learnt-transformation model. The format is the same as Figure 4.2a.

#### 4.4. TEMPORAL INTERPOLATION

---

between known samples in a sequence. The critical contribution of this section lies in demonstrating the potential of reconstruction-guided sampling to facilitate the generation of hourly precipitation samples that maintain coherency with adjacent samples of a bi-hourly temporal resolution. We emphasise the crucial role of the reconstruction-guidance weighting in achieving this goal.

Temporal interpolation of precipitation holds the potential to significantly benefit numerous real-world applications, such as the generation of high-resolution climate simulations. As detailed in Section 3.1, the extensive computational cost of producing such simulations hinders their widespread deployment [17]. Developing efficient interpolation techniques could address this challenge by enabling the generation of high-resolution climate simulations through a two-step process: initially generating data at a lower temporal resolution, followed by interpolating it to the desired temporal resolution. The benefits of such an approach hinge on two crucial aspects: ensuring that the computational savings realised during the initial generation of lower temporal resolution data are not negated by the cost of the subsequent interpolation process and the effectiveness of the interpolation technique in maintaining the coherence of the interpolated samples. Reconstruction-guided sampling plausibly contributes to the former by enabling multiple conditional generation tasks using a single unconditional model, thereby circumventing the need for separate conditional models for each task, which would incur significant computational expenses. Nevertheless, in the present study, our primary emphasis is on the latter: providing a proof of principle for temporal interpolation in the context of time-evolving hourly precipitation data while reserving a comprehensive analysis of the computational cost trade-offs for future research.

As demonstrated by Figure 4.19 and Figure 4.20, the quality of the interpolated samples is highly contingent upon an adequately high reconstruction-guidance weighting. With a reconstruction-guidance weight of  $w_r = 0$ , our conditional sampling procedure is equivalent to the imputation method [40] and results in a distribution that significantly deviates from the observed distribution, particularly in the underestimation of the probability of more intense precipitation. Interestingly, even with a reconstruction-guidance weight of  $w_r = 10^3$ , the improvement over the imputation method remains marginal.

By employing a reconstruction-guidance weight of  $w_r = 10^6$ , we obtain a distribution closely resembling the observed distribution of the corresponding withheld samples from the test set. We can regard the limitations observed in the interpolated samples generated with a low reconstruction-guidance weighting as accentuated manifestations of the shortcomings inherent in our unconditional model. Specifically, samples generated in the unconditional setting tend to underrepresent the probability of more intense precipitation, a problem mirrored and magnified in the interpolated samples generated under a low reconstruction-guidance weighting. Intriguingly, utilising a sufficiently large reconstruction-guidance weight effectively mitigates these issues, resulting in interpolated samples that better represent the probability of more intense precipitation.

In examining the spatial characteristics of the interpolated samples, we observe a similar trend, as illustrated in Figure 4.21a. Notably, interpolated samples generated with a reconstruction-guidance weight of  $w_r = 0$  or  $w_r = 10^3$  exhibit power in the spatial dimensions that significantly deviates from the corresponding withheld samples in the test set. In contrast, when utilising a reconstruction-guidance weight of  $w_r = 10^6$ , the power in the spatial dimensions of the interpolated samples closely aligns with that of the corresponding withheld samples.

The temporal PSD graph in Figure 4.21b further supports this trend, reinforcing the inadequacy of lower reconstruction-guidance weightings. We observe that the interpolated samples generated with a lower weighting have significantly too much power at the lowest temporal scales, attributable to the deviation in the distribution of individual precipitation intensities. More specifically, due to the substantial deviation in the distribution of individual intensities,

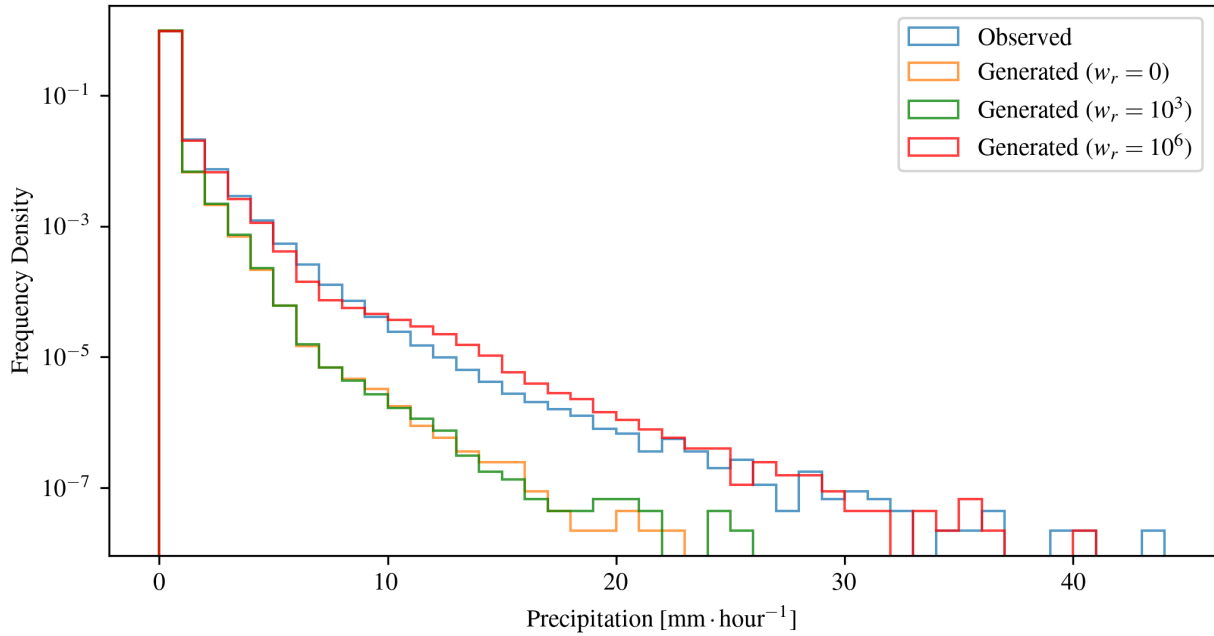


Figure 4.19: Distribution of individual precipitation rates in the conditionally generated interpolated samples produced by our learnt-transformation model with varying reconstruction-guidance weights, and the observed distribution of the corresponding withheld samples from 12 seasons in our test set. The format is the same as Figure 4.3.

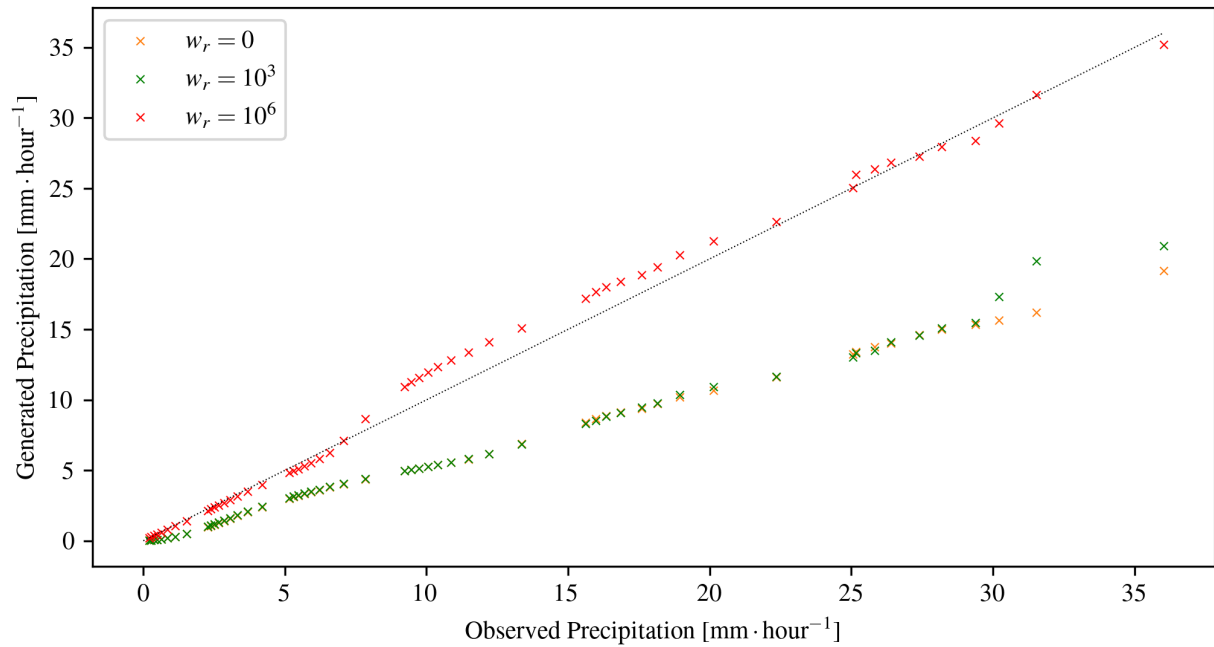


Figure 4.20: QQ plot comparing the distribution of individual precipitation rates in the conditionally generated interpolated samples produced by our learnt-transformation model with varying reconstruction-guidance weights against the corresponding observed withheld samples from 12 seasons in our test set. The format is the same as Figure 4.4.

the interpolated samples bear little resemblance to their adjacent samples, resulting in a high power at the most minute temporal scales. However, when employing a reconstruction-guidance weight of  $w_r = 10^6$ , the temporal PSD graph of the interpolated samples is remarkably similar to that of the corresponding withheld samples. The most pronounced deviation similarly occurs at the lowest temporal scale, albeit to a significantly lesser extent.

Figure 4.22 further underscores the critical role of the reconstruction-guidance weighting by visually representing a single interpolated sample generated with different weightings; only the hourly samples generated with a weight of  $w_r = 10^6$  exhibit a resemblance to the corresponding withheld samples from the test set.

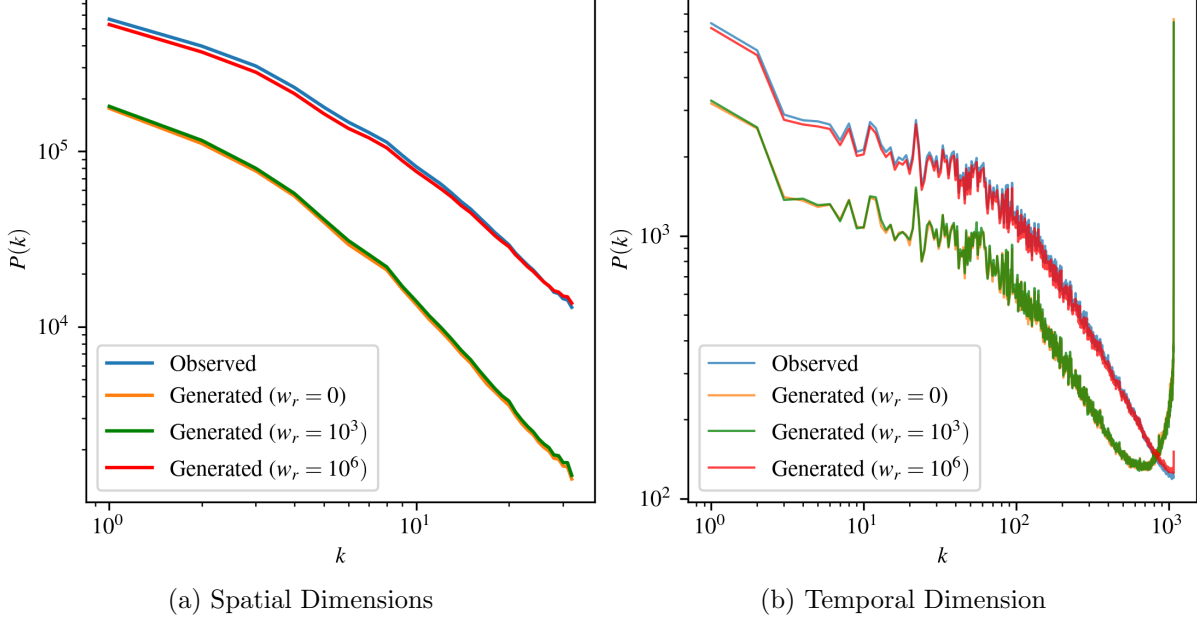


Figure 4.21: PSD graphs for samples generated via our learnt-transformation model with different reconstruction-guidance weights and the test set from UKCP18. The format is the same as Figure 4.6.

In summary, this section establishes the potential for generating interpolated samples with a distribution of individual intensities and spatiotemporal characteristics that closely resemble the corresponding withheld samples from the test set, achieved by employing an adequate reconstruction-guidance weighting. The discrepancies observed between the interpolated and corresponding withheld samples are considerably less pronounced than those observed in the unconditional setting, making the results particularly encouraging. Despite the model’s inherent limitations in the unconditional context, a substantial reconstruction-guidance weighting allows the same unconditional model to generate interpolated samples that overcome these limitations.

## 4.5 Nowcasting

Following the successful application of reconstruction-guided sampling for temporal interpolation, as demonstrated in the previous section, we extend our study to its potential applicability for nowcasting. This section presents preliminary proof-of-principle results for using a diffusion model to generate nowcasts.

As demonstrated by Figure 4.23 and Figure 4.24, the distribution of individual intensities in the conditionally generated nowcasts resembles the distribution of the corresponding withheld samples from the test set. The similar distribution suggests that the nowcasts broadly contain the correct amount of precipitation. However, there are notable discrepancies. Specifically, the nowcasts underrepresent precipitation less intense than 10 millimetres per hour and overrepresent

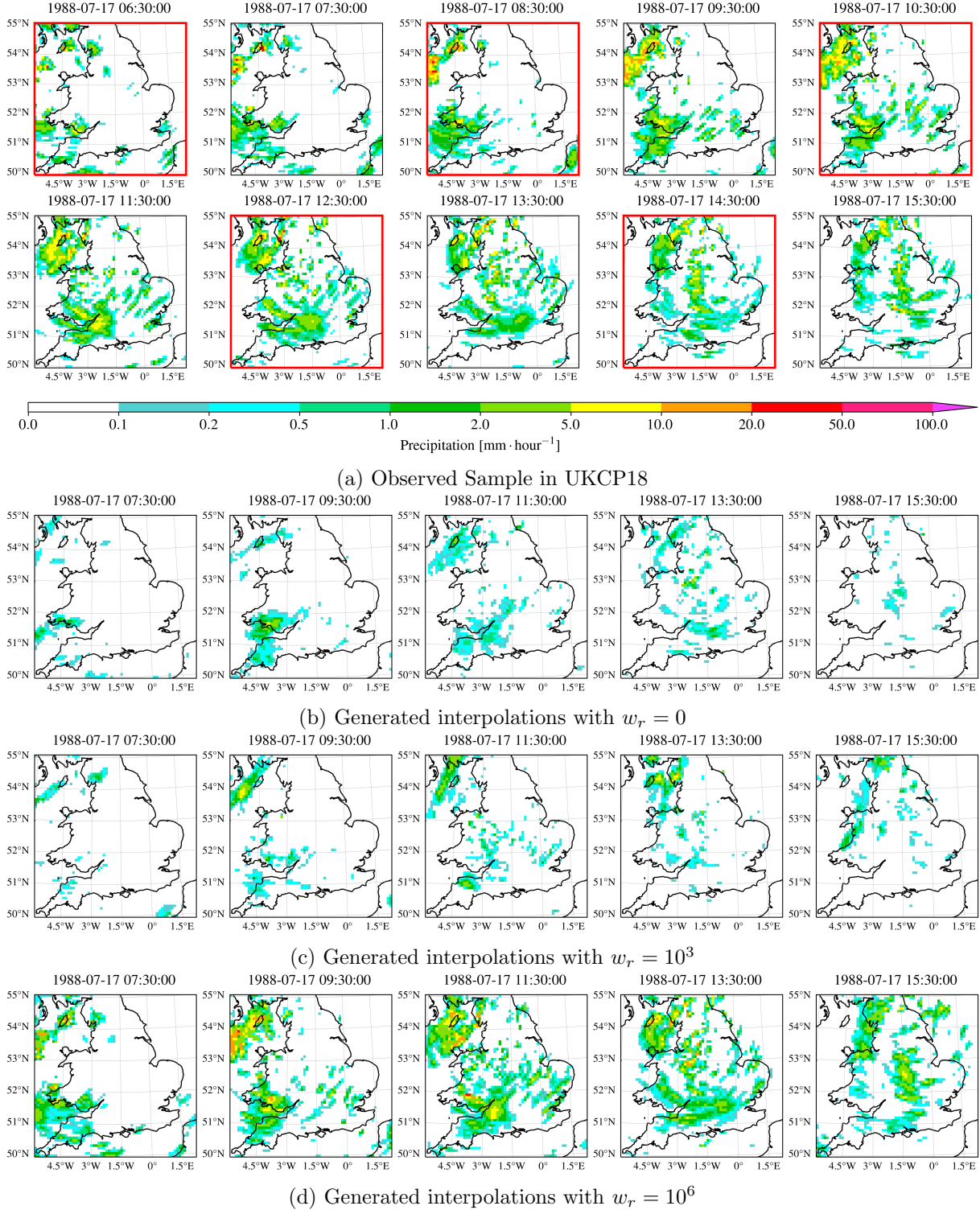


Figure 4.22: Temporally interpolated samples generated via our learnt-transformation model. Figure 4.22a depicts the observed sample in UKCP18, with the hourly snapshots conditioned on highlighted in red. The three subsequent figures depict interpolated samples generated with different reconstruction-guidance weights; captions below each figure indicate the reconstruction-guidance weight  $w_r$ . Ideally, each hourly snapshot should be identical, or very similar, to the corresponding true snapshot in Figure 4.22a. The format of each hourly snapshot is the same as Figure 4.2a.

## 4.5. NOWCASTING

---

more intense precipitation. Interestingly, the discrepancies appear to be accentuated versions of those observed in the interpolated samples generated with an identical reconstruction-guidance weighting of  $w_r = 10^6$ . This similarity suggests that developing techniques to address the discrepancies in the interpolated samples may also apply to the nowcasts and vice versa.

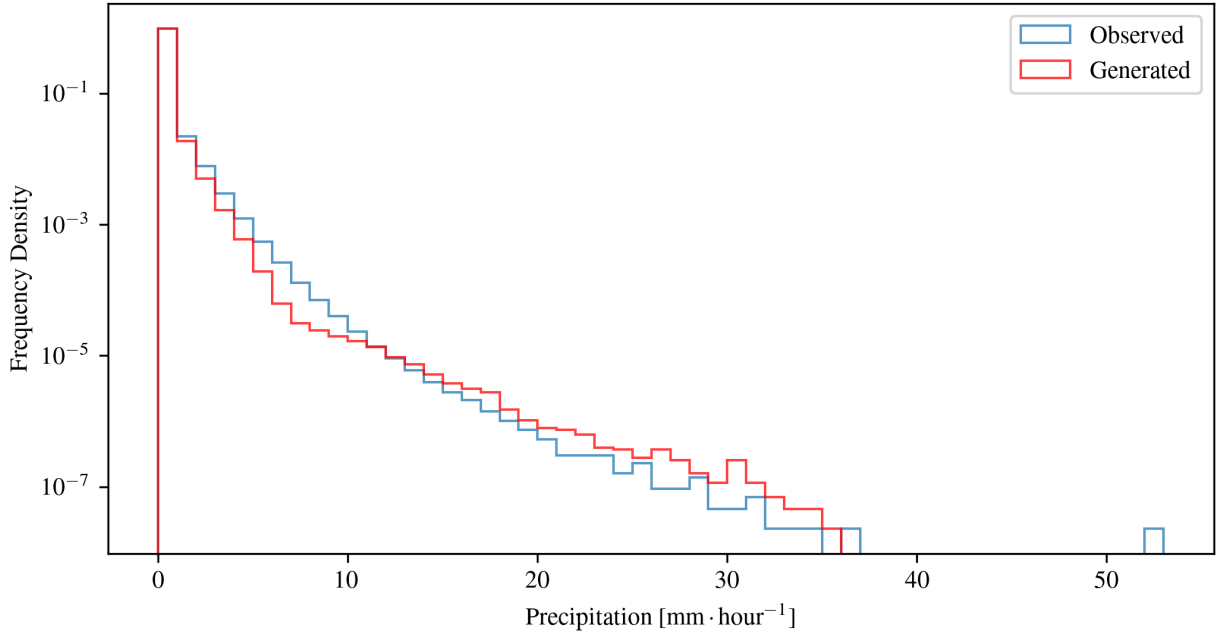


Figure 4.23: Distribution of individual precipitation rates in the conditionally generated nowcasts produced by our learnt-transformation model, and the observed distribution of the corresponding withheld samples from 12 seasons in our test set. The format is the same as Figure 4.3.

Figure 4.25 depicts PSD graphs for the spatial and temporal dimensions of the nowcasts and the corresponding withheld samples from the test set. As evident from the spatial PSD graph in Figure 4.25a, the nowcasts exhibit similar spatial characteristics to their corresponding withheld samples from the test set. The similarity is better at more minor spatial scales; at the most minute spatial scale, the difference in power is negligible. At all scales, the discrepancy between the nowcasts and the withheld samples is less pronounced than the discrepancy between the unconditionally generated samples and the test set. The consistently lesser discrepancy reaffirms our earlier observation that an adequate reconstruction-guidance weight enables the same unconditional model to generate samples conditionally that partially overcome the model’s inherent limitations in the unconditional setting.

Figure 4.26 presents a nowcast sample generated by our model, which showcases the model’s proficiency in several aspects. In particular, the model demonstrates its merit in accurately capturing the easterly movement of the precipitation band, as evidenced by the alignment of the predicted and actual precipitation patterns. Moreover, the model exhibits its ability to capture the correct movement of the precipitation band. For instance, in the final snapshot provided to the model, the precipitation band is just entering the South West of England. Remarkably, the nowcast reveals that the model has adeptly captured the band’s progress, extending as far as Exeter four hours later. The model has also successfully identified the relative immobility of the most easterly part of the precipitation band. In the final snapshot provided to the model, the most easterly segment of the band has a longitude of approximately 1.5 degrees west. In both the nowcast five hours later and the corresponding observed snapshot, the most easterly segment of the band similarly has a longitude of approximately 1.5 degrees west.

In summary, this section establishes a proof-of-principle for the ability of diffusion models to generate nowcasts. We leave the development of techniques to address the discrepancies

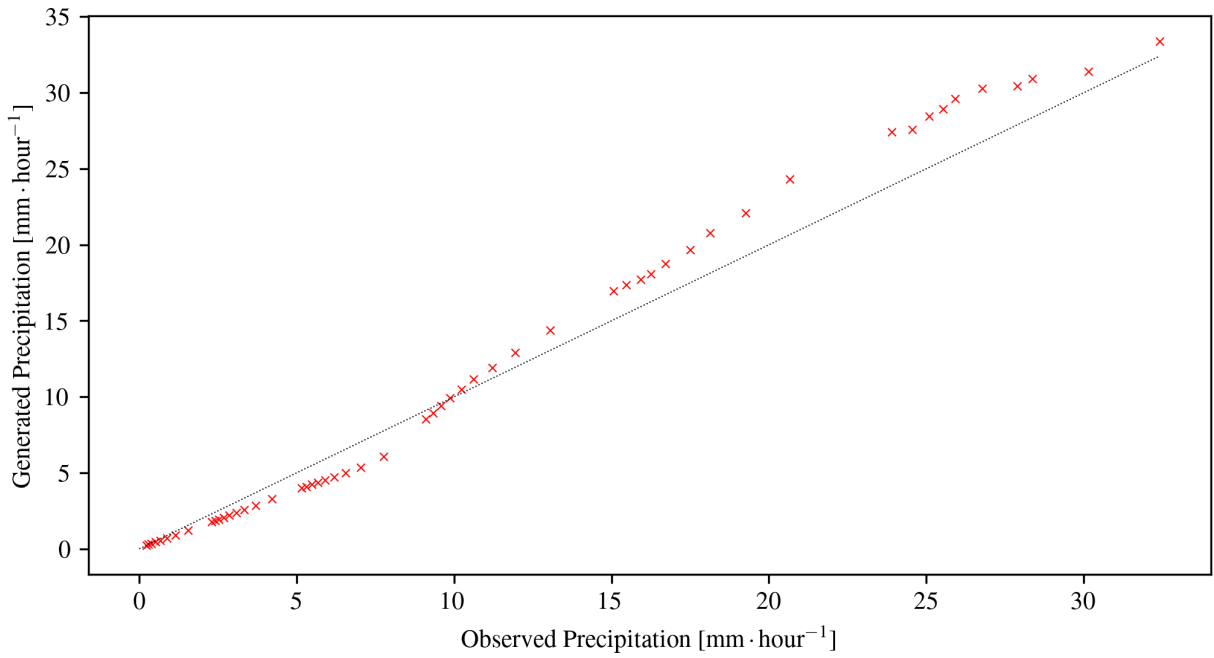


Figure 4.24: QQ plot comparing the distribution of individual precipitation rates in the conditionally generated nowcasts produced by our learnt-transformation model against the corresponding observed withheld samples from 12 seasons in our test set. The format is the same as Figure 4.4.

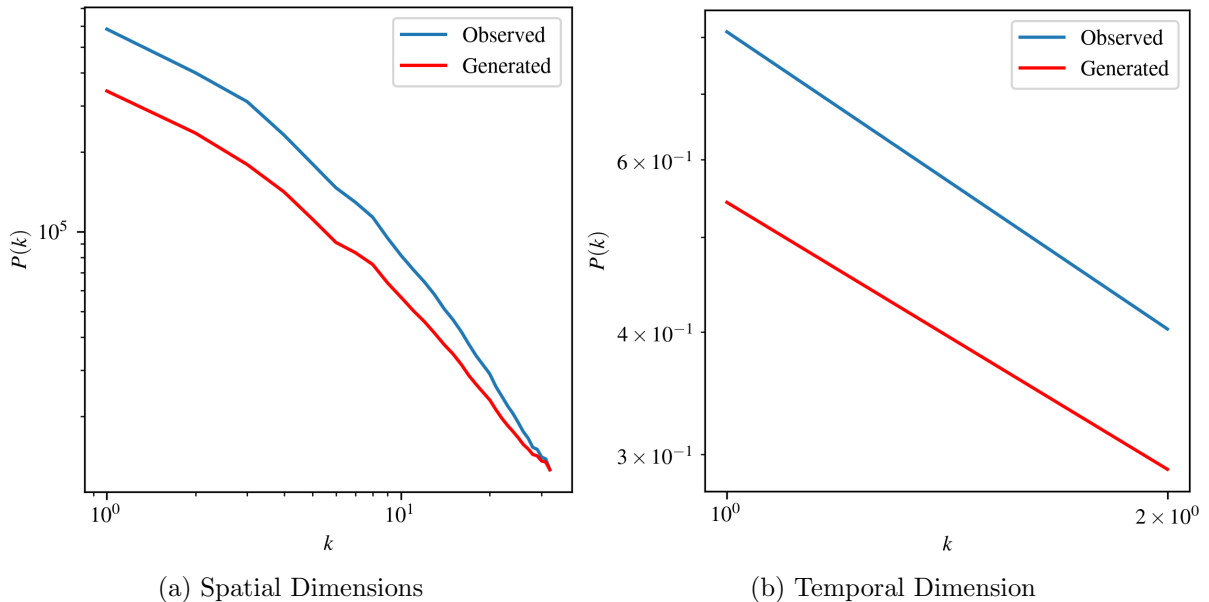


Figure 4.25: PSD graphs for conditionally generated nowcasts produced via our learnt-transformation model against the corresponding observed withheld samples from 12 seasons in our test set. The format is the same as Figure 4.6.

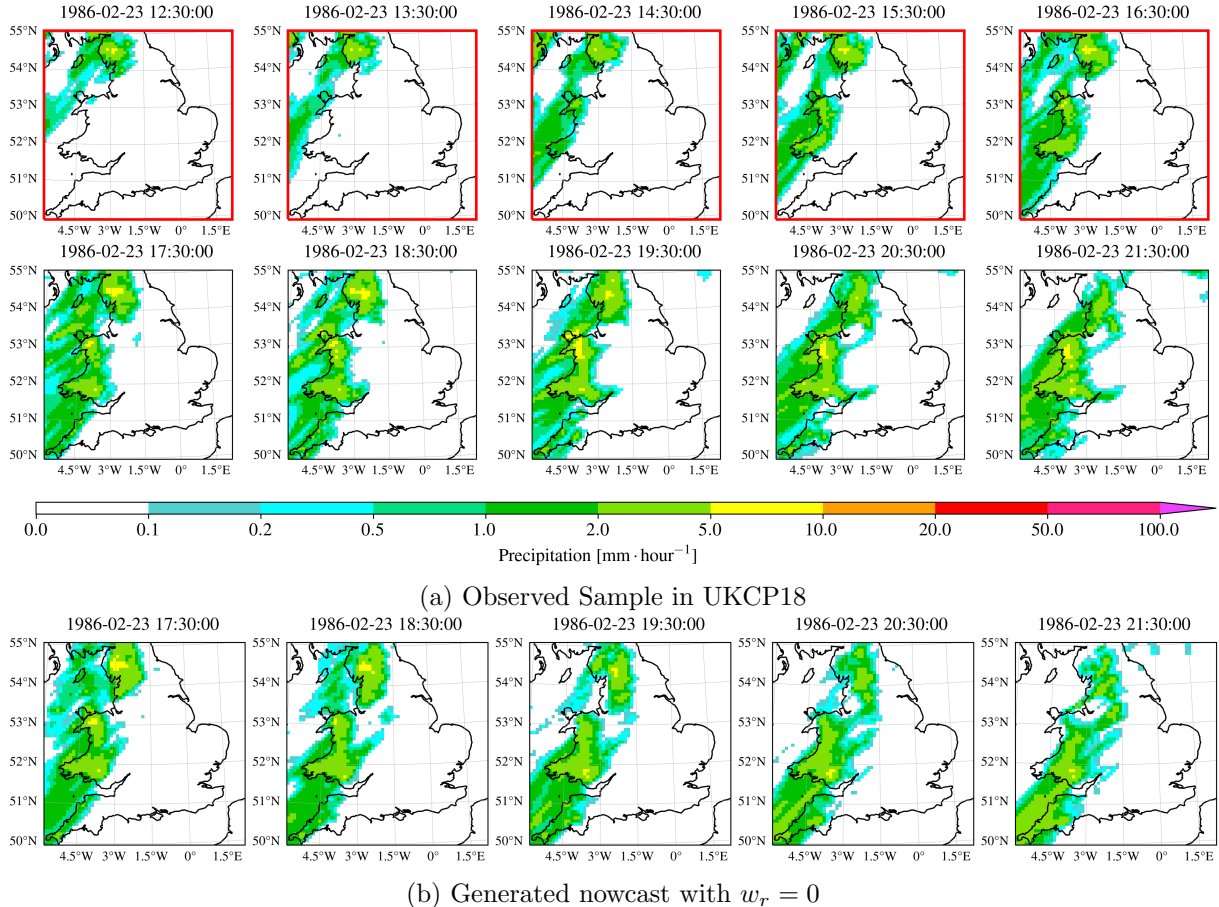


Figure 4.26: Nowcast sample generated via our learnt-transformation model. Figure 4.26a depicts an observed sample in UKCP18, with the hourly samples conditioned on in the subsequent nowcast highlighted in red. Figure 4.26b depicts the corresponding nowcast. Ideally, each hourly snapshot in the nowcast should resemble the corresponding observed snapshot. The format of each hourly snapshot is the same as Figure 4.2a.

#### *4.5. NOWCASTING*

---

observed in the nowcasts and a more comprehensive analysis for future work.

---

## Chapter 5

# Conclusion

### 5.1 Main Contributions

### 5.2 Future Work

---

# Bibliography

- [1] Henry Addison, Elizabeth Kendon, Suman V. Ravuri, Laurence Aitchison, and Peter A. G. Watson. Machine learning emulation of a local-scale UK climate model. *CoRR*, abs/2211.16116, 2022. [arXiv:2211.16116](https://arxiv.org/abs/2211.16116), doi:10.48550/arXiv.2211.16116.
- [2] Brian D.O. Anderson. Reverse-time diffusion equation models. *Stochastic Processes and their Applications*, 12(3):313–326, 1982. URL: <https://www.sciencedirect.com/science/article/pii/0304414982900515>, doi:[https://doi.org/10.1016/0304-4149\(82\)90051-5](https://doi.org/10.1016/0304-4149(82)90051-5).
- [3] Anurag Arnab, Mostafa Dehghani, Georg Heigold, Chen Sun, Mario Lucic, and Cordelia Schmid. Vivit: A video vision transformer. In *2021 IEEE/CVF International Conference on Computer Vision, ICCV 2021, Montreal, QC, Canada, October 10-17, 2021*, pages 6816–6826. IEEE, 2021. doi:10.1109/ICCV48922.2021.00676.
- [4] Gedas Bertasius, Heng Wang, and Lorenzo Torresani. Is space-time attention all you need for video understanding? In Marina Meila and Tong Zhang, editors, *Proceedings of the 38th International Conference on Machine Learning, ICML 2021, 18-24 July 2021, Virtual Event*, volume 139 of *Proceedings of Machine Learning Research*, pages 813–824. PMLR, 2021. URL: <http://proceedings.mlr.press/v139/bertasius21a.html>.
- [5] Neill E. Bowler, Clive Pierce, and Alan W. Seed. Steps: A probabilistic precipitation forecasting scheme which merges an extrapolation nowcast with downscaled nwp. *Quarterly Journal of the Royal Meteorological Society*, 132, 2006.
- [6] Xi Chen, Nikhil Mishra, Mostafa Rohaninejad, and Pieter Abbeel. Pixelsnail: An improved autoregressive generative model. In Jennifer G. Dy and Andreas Krause, editors, *Proceedings of the 35th International Conference on Machine Learning, ICML 2018, Stockholm, Sweden, July 10-15, 2018*, volume 80 of *Proceedings of Machine Learning Research*, pages 863–871. PMLR, 2018. URL: <http://proceedings.mlr.press/v80/chen18h.html>.
- [7] Antoine Doury, Samuel Somot, Sébastien Gadat, Aurélien Ribes, and Lola Corre. Regional climate model emulator based on deep learning: concept and first evaluation of a novel hybrid downscaling approach. *Climate Dynamics*, 60(5):1751–1779, Mar 2023. doi:10.1007/s00382-022-06343-9.
- [8] Ian J. Goodfellow, Jean Pouget-Abadie, Mehdi Mirza, Bing Xu, David Warde-Farley, Sherjil Ozair, Aaron C. Courville, and Yoshua Bengio. Generative adversarial networks. *CoRR*, abs/1406.2661, 2014. URL: <http://arxiv.org/abs/1406.2661>, arXiv:1406.2661.
- [9] Ida Bülow Gregersen, Hjalte Jomo Danielsen Sørup, Henrik Madsen, Dan Rosbjerg, Peter Steen Mikkelsen, and Karsten Arnbjerg-Nielsen. Assessing future climatic changes of rainfall extremes at small spatio-temporal scales. *Climatic Change*, 118(3):783–797, Jun 2013. doi:10.1007/s10584-012-0669-0.

## BIBLIOGRAPHY

---

- [10] Martin Hanel and T. Adri Buishand. On the value of hourly precipitation extremes in regional climate model simulations. *Journal of Hydrology*, 393(3):265–273, 2010. URL: <https://www.sciencedirect.com/science/article/pii/S002216941000541X>, doi:<https://doi.org/10.1016/j.jhydrol.2010.08.024>.
- [11] Jonathan Ho, William Chan, Chitwan Saharia, Jay Whang, Ruiqi Gao, Alexey A. Gritsenko, Diederik P. Kingma, Ben Poole, Mohammad Norouzi, David J. Fleet, and Tim Salimans. Imagen video: High definition video generation with diffusion models. *CoRR*, abs/2210.02303, 2022. arXiv:2210.02303, doi:10.48550/arXiv.2210.02303.
- [12] Jonathan Ho, Ajay Jain, and Pieter Abbeel. Denoising diffusion probabilistic models. In Hugo Larochelle, Marc'Aurelio Ranzato, Raia Hadsell, Maria-Florina Balcan, and Hsuan-Tien Lin, editors, *Advances in Neural Information Processing Systems 33: Annual Conference on Neural Information Processing Systems 2020, NeurIPS 2020, December 6-12, 2020, virtual*, 2020. URL: <https://proceedings.neurips.cc/paper/2020/hash/4c5bcfec8584af0d967f1ab10179ca4b-Abstract.html>.
- [13] Jonathan Ho, Nal Kalchbrenner, Dirk Weissenborn, and Tim Salimans. Axial attention in multidimensional transformers. *CoRR*, abs/1912.12180, 2019. URL: <http://arxiv.org/abs/1912.12180>, arXiv:1912.12180.
- [14] Jonathan Ho, Chitwan Saharia, William Chan, David J. Fleet, Mohammad Norouzi, and Tim Salimans. Cascaded diffusion models for high fidelity image generation. *J. Mach. Learn. Res.*, 23:47:1–47:33, 2022. URL: <http://jmlr.org/papers/v23/21-0635.html>.
- [15] Jonathan Ho, Tim Salimans, Alexey A. Gritsenko, William Chan, Mohammad Norouzi, and David J. Fleet. Video diffusion models. *CoRR*, abs/2204.03458, 2022. arXiv:2204.03458, doi:10.48550/arXiv.2204.03458.
- [16] Emiel Hoogeboom, Jonathan Heek, and Tim Salimans. simple diffusion: End-to-end diffusion for high resolution images. *CoRR*, abs/2301.11093, 2023. arXiv:2301.11093, doi:10.48550/arXiv.2301.11093.
- [17] Elizabeth Kendon, Giorgia Fosser, James Murphy, Steven Chan, Robin Clark, Glen Harris, Adrian Lock, Jason Lowe, Gill Martin, Jenny Pirret, Nigel Roberts, Mike Sanderson, and Simon Tucker. UKCP Convection-permitting model projections. Science report, Met Office Hadley Centre, September 2019. URL: <https://www.metoffice.gov.uk/pub/data/weather/uk/ukcp18/science-reports/UKCP-Convection-permitting-model-projections-report.pdf>.
- [18] Elizabeth J. Kendon, Nigel M. Roberts, Hayley J. Fowler, Malcolm J. Roberts, Steven C. Chan, and Catherine A. Senior. Heavier summer downpours with climate change revealed by weather forecast resolution model. *Nature Climate Change*, 4(7):570–576, Jul 2014. doi:10.1038/nclimate2258.
- [19] Diederik P. Kingma and Ruiqi Gao. Understanding the diffusion objective as a weighted integral of elbos. *CoRR*, abs/2303.00848, 2023. arXiv:2303.00848, doi:10.48550/arXiv.2303.00848.
- [20] Diederik P. Kingma and Max Welling. Auto-encoding variational bayes. In Yoshua Bengio and Yann LeCun, editors, *2nd International Conference on Learning Representations, ICLR 2014, Banff, AB, Canada, April 14-16, 2014, Conference Track Proceedings*, 2014. URL: <http://arxiv.org/abs/1312.6114>.

## BIBLIOGRAPHY

---

- [21] Durk P Kingma, Tim Salimans, Rafal Jozefowicz, Xi Chen, Ilya Sutskever, and Max Welling. Improved variational inference with inverse autoregressive flow. In D. Lee, M. Sugiyama, U. Luxburg, I. Guyon, and R. Garnett, editors, *Advances in Neural Information Processing Systems*, volume 29. Curran Associates, Inc., 2016. URL: [https://proceedings.neurips.cc/paper\\_files/paper/2016/file/ddeebdeefdb7e7e7a697e1c3e3d8ef54-Paper.pdf](https://proceedings.neurips.cc/paper_files/paper/2016/file/ddeebdeefdb7e7e7a697e1c3e3d8ef54-Paper.pdf).
- [22] Jussi Leinonen, Daniele Nerini, and Alexis Berne. Stochastic super-resolution for downscaling time-evolving atmospheric fields with a generative adversarial network. *IEEE Trans. Geosci. Remote. Sens.*, 59(9):7211–7223, 2021. doi:10.1109/TGRS.2020.3032790.
- [23] Andreas Lugmayr, Martin Danelljan, Andrés Romero, Fisher Yu, Radu Timofte, and Luc Van Gool. Repaint: Inpainting using denoising diffusion probabilistic models. In *IEEE/CVF Conference on Computer Vision and Pattern Recognition, CVPR 2022, New Orleans, LA, USA, June 18-24, 2022*, pages 11451–11461. IEEE, 2022. doi:10.1109/CVPR52688.2022.01117.
- [24] Met Office Hadley Centre. UKCP18 guidance: Representative concentration pathways. Technical report, 2018. URL: <https://www.metoffice.gov.uk/binaries/content/assets/metofficegovuk/pdf/research/ukcp/ukcp18-guidance---representative-concentration-pathways.pdf>.
- [25] Met Office Hadley Centre. UKCP18 probabilistic climate projections, 2018. URL: <http://catalogue.ceda.ac.uk/uuid/9842e395f2d04f48a177c3550756bf98>.
- [26] Alexander Quinn Nichol and Prafulla Dhariwal. Improved denoising diffusion probabilistic models. In Marina Meila and Tong Zhang, editors, *Proceedings of the 38th International Conference on Machine Learning, ICML 2021, 18-24 July 2021, Virtual Event*, volume 139 of *Proceedings of Machine Learning Research*, pages 8162–8171. PMLR, 2021. URL: <http://proceedings.mlr.press/v139/nichol21a.html>.
- [27] Clive Pierce, Alan Seed, Sue Ballard, David Simonin, and Zhihong Li. Nowcasting. In Joan Bech and Jorge Luis Chau, editors, *Doppler Radar Observations*, chapter 4. IntechOpen, Rijeka, 2012. doi:10.5772/39054.
- [28] Aditya Ramesh, Mikhail Pavlov, Gabriel Goh, Scott Gray, Chelsea Voss, Alec Radford, Mark Chen, and Ilya Sutskever. Zero-shot text-to-image generation. *CoRR*, abs/2102.12092, 2021. URL: <https://arxiv.org/abs/2102.12092>, arXiv:2102.12092.
- [29] Suman V. Ravuri, Karel Lenc, Matthew Willson, Dmitry Kangin, Rémi Lam, Piotr Mirowski, Megan Fitzsimons, Maria Athanassiadou, Sheleem Kashem, Sam Madge, Rachel Prudden, Amol Mandhane, Aidan Clark, Andrew Brock, Karen Simonyan, Raia Hadsell, Niall H. Robinson, Ellen Clancy, Alberto Arribas, and Shakir Mohamed. Skillful precipitation nowcasting using deep generative models of radar. *CoRR*, abs/2104.00954, 2021. URL: <https://arxiv.org/abs/2104.00954>, arXiv:2104.00954.
- [30] Danilo Jimenez Rezende, Shakir Mohamed, and Daan Wierstra. Stochastic backpropagation and approximate inference in deep generative models. In *Proceedings of the 31th International Conference on Machine Learning, ICML 2014, Beijing, China, 21-26 June 2014*, volume 32 of *JMLR Workshop and Conference Proceedings*, pages 1278–1286. JMLR.org, 2014. URL: <http://proceedings.mlr.press/v32/rezende14.html>.
- [31] Robin Rombach, Andreas Blattmann, Dominik Lorenz, Patrick Esser, and Björn Ommer. High-resolution image synthesis with latent diffusion models. In *IEEE/CVF Conference on Computer Vision and Pattern Recognition, CVPR 2022, New Orleans, LA, USA, June 18-24, 2022*, pages 10674–10685. IEEE, 2022. doi:10.1109/CVPR52688.2022.01042.

## BIBLIOGRAPHY

---

- [32] Olaf Ronneberger, Philipp Fischer, and Thomas Brox. U-net: Convolutional networks for biomedical image segmentation. *CoRR*, abs/1505.04597, 2015. URL: <http://arxiv.org/abs/1505.04597>, arXiv:1505.04597.
- [33] Chitwan Saharia, William Chan, Saurabh Saxena, Lala Li, Jay Whang, Emily Denton, Seyed Kamyar Seyed Ghasemipour, Burcu Karagol Ayan, S. Sara Mahdavi, Rapha Gontijo Lopes, Tim Salimans, Jonathan Ho, David J. Fleet, and Mohammad Norouzi. Photorealistic text-to-image diffusion models with deep language understanding. *CoRR*, abs/2205.11487, 2022. arXiv:2205.11487, doi:10.48550/arXiv.2205.11487.
- [34] Chitwan Saharia, Jonathan Ho, William Chan, Tim Salimans, David J. Fleet, and Mohammad Norouzi. Image super-resolution via iterative refinement. *CoRR*, abs/2104.07636, 2021. URL: <https://arxiv.org/abs/2104.07636>, arXiv:2104.07636.
- [35] Tim Salimans and Jonathan Ho. Progressive distillation for fast sampling of diffusion models. In *The Tenth International Conference on Learning Representations, ICLR 2022, Virtual Event, April 25-29, 2022*. OpenReview.net, 2022. URL: <https://openreview.net/forum?id=TIdIXIpzh0I>.
- [36] Tim Salimans, Andrej Karpathy, Xi Chen, and Diederik P. Kingma. Pixelcnn++: Improving the pixelcnn with discretized logistic mixture likelihood and other modifications. *CoRR*, abs/1701.05517, 2017. URL: <http://arxiv.org/abs/1701.05517>, arXiv:1701.05517.
- [37] Jascha Sohl-Dickstein, Eric A. Weiss, Niru Maheswaranathan, and Surya Ganguli. Deep unsupervised learning using nonequilibrium thermodynamics. In Francis R. Bach and David M. Blei, editors, *Proceedings of the 32nd International Conference on Machine Learning, ICML 2015, Lille, France, 6-11 July 2015*, volume 37 of *JMLR Workshop and Conference Proceedings*, pages 2256–2265. JMLR.org, 2015. URL: <http://proceedings.mlr.press/v37/sohl-dickstein15.html>.
- [38] Casper Kaae Sønderby, Tapani Raiko, Lars Maaløe, Søren Kaae Sønderby, and Ole Winther. Ladder variational autoencoders. In Daniel D. Lee, Masashi Sugiyama, Ulrike von Luxburg, Isabelle Guyon, and Roman Garnett, editors, *Advances in Neural Information Processing Systems 29: Annual Conference on Neural Information Processing Systems 2016, December 5-10, 2016, Barcelona, Spain*, pages 3738–3746, 2016. URL: <https://proceedings.neurips.cc/paper/2016/hash/6ae07dcb33ec3b7c814df797cbda0f87-Abstract.html>.
- [39] Yang Song and Stefano Ermon. Generative modeling by estimating gradients of the data distribution. In Hanna M. Wallach, Hugo Larochelle, Alina Beygelzimer, Florence d’Alché-Buc, Emily B. Fox, and Roman Garnett, editors, *Advances in Neural Information Processing Systems 32: Annual Conference on Neural Information Processing Systems 2019, NeurIPS 2019, December 8-14, 2019, Vancouver, BC, Canada*, pages 11895–11907, 2019. URL: <https://proceedings.neurips.cc/paper/2019/hash/3001ef257407d5a371a96dcd947c7d93-Abstract.html>.
- [40] Yang Song, Jascha Sohl-Dickstein, Diederik P. Kingma, Abhishek Kumar, Stefano Ermon, and Ben Poole. Score-based generative modeling through stochastic differential equations. In *9th International Conference on Learning Representations, ICLR 2021, Virtual Event, Austria, May 3-7, 2021*. OpenReview.net, 2021. URL: <https://openreview.net/forum?id=PxTIG12RRHS>.
- [41] Hoang Thanh-Tung and Truyen Tran. Catastrophic forgetting and mode collapse in gans. In *2020 International Joint Conference on Neural Networks, IJCNN 2020, Glasgow, United Kingdom, July 19-24, 2020*, pages 1–10. IEEE, 2020. doi:10.1109/IJCNN48605.2020.9207181.

## BIBLIOGRAPHY

---

- [42] Ashish Vaswani, Noam Shazeer, Niki Parmar, Jakob Uszkoreit, Llion Jones, Aidan N. Gomez, Łukasz Kaiser, and Illia Polosukhin. Attention is all you need. In Isabelle Guyon, Ulrike von Luxburg, Samy Bengio, Hanna M. Wallach, Rob Fergus, S. V. N. Vishwanathan, and Roman Garnett, editors, *Advances in Neural Information Processing Systems 30: Annual Conference on Neural Information Processing Systems 2017, December 4-9, 2017, Long Beach, CA, USA*, pages 5998–6008, 2017. URL: <https://proceedings.neurips.cc/paper/2017/hash/3f5ee243547dee91fdb053c1c4a845aa-Abstract.html>.
- [43] Xiaolong Wang, Ross B. Girshick, Abhinav Gupta, and Kaiming He. Non-local neural networks. In *2018 IEEE Conference on Computer Vision and Pattern Recognition, CVPR 2018, Salt Lake City, UT, USA, June 18-22, 2018*, pages 7794–7803. Computer Vision Foundation / IEEE Computer Society, 2018. URL: [http://openaccess.thecvf.com/content\\_cvpr\\_2018/html/Wang\\_Non-Local\\_Neural\\_Networks\\_CVPR\\_2018\\_paper.html](http://openaccess.thecvf.com/content_cvpr_2018/html/Wang_Non-Local_Neural_Networks_CVPR_2018_paper.html), doi:10.1109/CVPR.2018.00813.
- [44] Yong Wang, Estelle Coning, Abdoulaye Harou, Wilfried Jacobs, Paul Joe, Larisa Nikitina, Rita Roberts, Jianjie Wang, Jim Wilson, Aitor Atencia, Benedikt Bica, Barbara Brown, Steven Goodmann, Alexander Kann, Ping wah Li, Isabel Monterio, Franziska Schmid, Alan Seed, and Jenny Sun. *Guidelines for Nowcasting Techniques*. World Meteorological Organization, 11 2017. URL: [https://library.wmo.int/doc\\_num.php?explnum\\_id=3795](https://library.wmo.int/doc_num.php?explnum_id=3795).
- [45] James W. Wilson, Yerong Feng, Min Chen, and Rita D. Roberts. Nowcasting challenges during the beijing olympics: Successes, failures, and implications for future nowcasting systems. *Weather and Forecasting*, 25(6):1691 – 1714, 2010. URL: [https://journals.ametsoc.org/view/journals/wefo/25/6/2010waf2222417\\_1.xml](https://journals.ametsoc.org/view/journals/wefo/25/6/2010waf2222417_1.xml), doi:<https://doi.org/10.1175/2010WAF2222417.1>.